[American Journal of Science, Vol. 320, March, 2020, P. 185–235, DOI 10.2475/03.2020.01]

American Journal of Science

MARCH 2020

THERMODYNAMIC CONSTRAINTS ON THE GEOCHEMISTRY OF LOW-TEMPERATURE, CONTINENTAL, SERPENTINIZATION-GENERATED FLUIDS

JAMES ANDREW M. LEONG*,***,† and EVERETT L. SHOCK*,**,***

ABSTRACT. The hydrous alteration of ultramafic rocks, known as serpentinization, generates fluids that can fuel microbial communities and enable the synthesis of simple organic compounds. Serpentinization reactions can proceed even at the ambient, low-temperature conditions present in continental aquifers raising questions about the limits of life deep in the Earth's subsurface. Through thermodynamic calculations, we investigate various reactions that facilitate the transformation of oxic, slightly acidic rainwater into reduced, hyperalkaline fluids during low-temperature serpentinization. We explore a suite of factors (variabilities in temperature, host-rock compositions, fluid salinity, and the buffering capacity of various serpentinization-relevant minerals) that offer broad insights into the chemical environments formed through low-temperature serpentinization. Results of calculations show that alteration of olivine-rich lithologies will lead to fluids constrained by the chrysotile-brucite-diopside equilibrium assemblage, close in pH to those measured from the most alkaline fluids hosted in ultramafic rocks. Variabilities in the compositions of fluids hosted by continental serpentinizing systems can be attributed to a shift from being in equilibrium with diopside to calcite, among other reactions. Results of calculations also show that it would be difficult to distinguish fluids reacting with either fresh or altered ultramafic rocks based solely on their pH, and total dissolved Ca, Mg and Si content. Our models also account for Fe incorporation into solid solutions of serpentine and brucite and show that the global H_2 flux from continental serpentinization could be considerably lower than estimates based on iron oxidation to magnetite only. Lastly, we present the energetic landscape available to subsurface microorganisms by focusing on two microbial process using H_2: methanogenesis and hydrogen oxidation. Limited but available energy (0.2–1.7 calories/kg fluid) can be exploited by methanogens, permitting the possibility of deep communities in serpentinizing aquifers. More energy is available for methanogenesis (0.2–6 calories/kg fluid) and hydrogen oxidation (0–17 calories/kg fluid) when upwelling, deep-seated, serpentinization-generated fluids mix with shallow groundwater. Ultimately, predictions set forth in this study provide a framework for testing ideas that can explain the compositions of fluids and microbial communities sampled at ultramafic environments here on Earth and perhaps in the near future, on ocean worlds in our solar system.

Keywords: serpentinization, water-rock interaction, thermodynamics, microbial energetics

INTRODUCTION

Environments where water meets ultramafic rocks enable serpentinization, one of the most profound geochemical processes on Earth. During serpentinization, minerals

* Group Exploring Organic Processes In Geochemistry, Arizona State University, Tempe, Arizona, 85287, USA
** School of Earth & Space Exploration, Arizona State University, Tempe, Arizona, 85287, USA
*** School of Molecular Sciences, Arizona State University, Tempe, Arizona, 85287, USA
† Corresponding author: jmleong@asu.edu

that compose ultramafic rocks (olivine and pyroxene), are replaced mainly by serpentine upon interaction with water. Serpentinization drives the transformation of near-neutral and oxic surface fluids like rain or seawater into alkaline, reduced fluids rich in H_2 and CH_4. These reduced fluids provide energy and nutrients for chemosynthetic communities (see review by Schrenk and others, 2013), abiotically synthesize organic compounds (see review by McCollom and Seewald, 2007), and potentially facilitate the emergence of life on Earth (Sleep and others, 2004, 2011; Holm and others, 2006; Martin and Russel, 2007; Martin and others, 2008, 2014; Russel and others, 2010; Lane and Martin, 2012). Serpentinization extends beyond Earth, as ultramafic rocks are present in a number of terrestrial bodies in the Solar System (Schulte and others, 2006; Vance and others, 2007; Ehlmann and others, 2010; Holm and others, 2015, Glein and others, 2015), raising possibilities of life powered by water-rock interactions beyond our own planet.

On Earth, serpentinization occurs wherever ultramafic rocks meet water, which is inevitable at the seafloor. Chimneys venting H_2- and CH_4-rich fluids at temperatures exceeding 100 °C, including those at the Rainbow (Charlou and others, 2002; Douville and others, 2002), Logatchev (Schmidt and others, 2007), Kairei (Gallant and Von Damm, 2006; Kumagai and others, 2008), Von Damm (McDermott and others, 2015), and Lost City (Kelley and others, 2001, 2005; Lang and others, 2010; Seyfried and others, 2015) vent fields, are well known consequences of hydrothermal interactions between ultramafic rocks and seawater. Less dramatic but likely more widespread outcomes of serpentinization are low-temperature (<100 °C) H_2- and CH_4-rich hyperalkaline fluids seeping diffusely from ultramafic rocks exposed near spreading ridges (Früh-Green and others, 2003, 2018), serpentinite mud volcanoes near subduction zones (Mottl and others, 2003, 2004; Wheat and others, 2008; Mottl, 2009), and exposed ultramafic outcrops in continents such as in ophiolites, ultramafic massifs, metamorphic belts and kimberlite deposits (see table 1).

Serpentinizing systems hosted on the continents provide accessible opportunities to sample deep-seated fluids. These low-temperature systems also provide examples to test predictions about the consequences of water and rock interactions without the added complexity of magmatic input like those in seafloor hydrothermal systems. Recent undertakings to drill into and sample deep aquifers, and subsequently establish a borehole observatory on the Samail Ophiolite in Oman (Kelemen and others, 2013; https://www.omandrilling.ac.uk/) will advance knowledge of the subsurface reactions driving fluid transformation during the serpentinization process. In preparation, insights into these subsurface reactions can be provided by thermodynamic predictions.

Several theoretical investigations have focused on seawater-ultramafic interactions at hydrothermal conditions (Janecky and Seyfried, 1986; Wetzel and Shock, 2000; Alt and Shanks, 2003; Allen and Seyfried, 2004; Palandri and Reed, 2004; Frost and Beard, 2007; Seyfried and others, 2007, 2015; Foustoukos and others, 2008; McCollom and Bach, 2009; Klein and others, 2009, 2013; Evans and others, 2013; Bach and others, 2013). The existing theoretical studies for low-temperature continental serpentinizing settings (Pfeifer, 1977; Bruni and others, 2002; Palandri and Reed, 2004; Cipolli and others, 2004; Boschetti and Toscani, 2008; Marques and others, 2008; Okland and others, 2012; Paukert and others, 2012) tend to focus on the consequence of altering a specific composition of ultramafic rock under conditions for a given study site. Here we examine low-temperature continental serpentinization independent of conditions dictated by a specific locality. Our initial focus is on generalized reactions that drive the serpentinization process. We examine the consequences brought about by variabilities in temperatures (0–100 °C), fluid salinity, and host rock compositions. Other factors such as varying dissolved inorganic carbon (DIC) input, and the buffering capacity of

TABLE 1

List of continental locations with documented fluid and gas compositions attributed to serpentinization

Location	Study[1]
U.S.A. (Coast Range ophiolites, the Cedars, Del Puerto ophiolite, California and Oregon)	Barnes and others, 1967; Barnes and O'Neil, 1969; Blank and others, 2009*; Cardace and others, 2013; Crespo-Medina and others, 2014*; Morrill and others, 2013; Suzuki and others, 2013*, 2014*, 2017*; Kohl and others, 2016*; Twing and others, 2017*; Meyer-Dombard and others, 2018
Switzerland (Engadine Valley)	Pfeiffer, 1977
Italy (Voltri, Taro-Cenno, Elba)	Pfeiffer, 1977; Bruni and others, 2002; Cipolli and others, 2004; Boschetti and Toscani, 2008; Chavagnac and others, 2013a, 2013b; Boulart and others, 2013**; Schwarzenbach and others, 2013; Boschetti and others, 2013; Quéméneur and others, 2015*; Segadelli and others, 2016; Brazelton and others, 2017*; Sciarra and others, 2019**; Etiope and Whiticar, 2019**
Greece (Othrys and Argolida ophiolites)	Papastamaki, 1977; Etiope and others, 2013a**; D'Alessandro and others, 2018; Daskalopoulou and others, 2018**
Oman (Samail ophiolite)	Barnes and others, 1978; Neal and Stanger, 1983**, 1984, 1985; Bath and others, 1987*; Taylor and others, 1991; Sano and others, 1993**; Dewandel and others, 2005; Matter and others, 2006; Paukert Vankeuren and others, 2012, 2019; Chavagnac and others, 2013a, 2013b; Boulart and others, 2013**; Olson and others, 2014; Miller and others, 2016*; Rempfert and others, 2017*; Canovas and others, 2017; Vacquand and others, 2018**; Zgonnik and others, 2019**; Fones and others, 2019*; Giampouras and others, 2020
New Caledonia (Prony Bay)	Barnes and others, 1978; Monnin and others, 2014; Quéméneur and others, 2014*; Postec and others, 2015*; Vacquand and others, 2018**
Bosnia and Herzegovina (Dinaride ophiolite)	Barnes and others, 1978; Etiope and others, 2017**
Philippines (Zambales and Palawan ophiolites)	Abrajano and others, 1988**, 1990**; Fujii and others, 2010; Cardace and others, 2015; Woycheese and others, 2015*; Baculi and others, 2015*; Shimbashi and others, 2018; Vacquand and others, 2018**; Meyer-Dombard and others, 2018*, 2019*
New Zealand (Poison Bay, Dun Mountain)	Giggenbach and others, 1993**; Pawson and others, 2014**
Cyprus (Trodos massif)	Neal and Shand, 2002; Rizoulis and others, 2016*
Mexico (Socorro Island)[2]	Taran and others, 2002, 2010**
Canada (Kirkland Lake and Lake Timiskiming kimberlite fields, Canadian Shield, and Tablelands massif)	Sader and others, 2007; Sherwood-Lollar and others, 2007**; Szponar and others, 2013; Brazelton and others, 2012*, 2013*; Morrill and others, 2014*; Cumming and others, 2019
Portugal (Iberian Hercynian Belt)	Tiago and others, 2004*; Marques and others, 2008, 2018; Etiope and others, 2013b**; Tiago and Veríssimo, 2013*
Finland (Outokumpu deep drill hole, Fennoscandian Shield)[3]	Sherwood-Lollar and others, 2007**; Itävaara and others, 2011*; Nyyssönen and others, 2014*
Turkey (Chimaera seep and Tekirova ophiolites)	Hosgormez and others, 2008**; Etiope and others, 2011**; Meyer-Dombard and others, 2015*; Neubeck and others, 2017*
Japan (Hakuba Happo springs, Hida belt)	Homma and Tsukahara, 2008; Suda and others, 2014**, 2017**
Norway (Leka ophiolite)	Okland and others, 2012; Daee and others, 2013*
Costa Rica (Santa Elena ophiolite)	Sanchez-Murillo and others, 2013*; Crespo-Medina and others, 2017*
U.A.E. (Samail ophiolite)	Etiope and others, 2015**
Spain (Ronda massif)	Etiope and others, 2016**; Giampouras and others, 2019

[1]Those indicated by * are microbiological studies or geochemical studies that include microbiological data. Those indicated with ** are studies focused on gas compositions. All the rest are focused on the aqueous compositions and/or hydrogeology of serpentinizing systems.

[2]Acidic hotsprings that likely have input from volcanic gas.

[3]Borehole lithology is dominated by metasedimentary rocks with some ultramafic sequence.

various Ca-bearing minerals are considered. Exploration of this suite of factors offers broad insights into the chemical environments formed through low-temperature serpentinization. In the latter part of this paper, we describe model outcomes for the amounts of H_2 generated, and offer a reevaluation of existing estimates for the global H_2 flux from continental serpentinization. Lastly, we present the energetic landscape

available to subsurface microorganisms by focusing on two microbial processes: methanogenesis and hydrogen oxidation.

OVERVIEW OF LOW-TEMPERATURE CONTINENTAL SERPENTINIZATION

Since the reports in the 1960's by Barnes and others (1967, 1972, 1978) and Barnes and O'Neil (1969), studies on the chemistry of continental hyperalkaline fluids have grown to encompass a number of settings in ~ 20 countries shown in table 1. A number of these studies (Neal and Stanger, 1985; Bruni and others, 2002; Cipolli and others, 2004; Dewandel and others, 2005; Marques and others, 2008; Paukert and others, 2012; Okland and others, 2012) proposed models for the overall evolution of fluids that infiltrate into aquifers composed of ultramafic rocks. These models, together with observations from natural systems permit the following generalizations. Initially, rainwater infiltrates into the shallow aquifer and reacts with the rocks in a system open to atmospheric exchange. These reactions generate slightly basic (pH 7–9) fluids rich in Mg^{+2} and HCO_3^- that are often referred to as Type 1 fluids. It has been documented that Type 1 fluids occur in highly fractured zones of shallow ophiolite aquifers (<50 m, Dewandel and others, 2005), as well as in surface streams. Some fluids infiltrate into the deep subsurface and interact progressively with more and more ultramafic rocks in a system that is ultimately closed from atmospheric influence. The greater degrees of interactions between water and rock facilitate the transformation of meteoric and Type 1 fluids into reduced, hyperalkaline fluids that are enriched in Ca^{+2} and OH^-, often referred to as Type 2. It is estimated that these fluids originate at depths of at least 500 m (Dewandel and others, 2005). Through deep-seated structures such as faults and lithological contacts, these fluids can eventually discharge back onto the surface as hyperalkaline seeps, and precipitate travertine deposits upon interaction with atmospheric $CO_{2(g)}$ or mixing with HCO_3^--rich Type 1 fluids.

COMPUTATIONAL MODEL

Reaction path calculations simulate processes occurring during rock alteration by quantifying changes in the aqueous and mineral compositions arising from irreversible mass transfer reactions as specified quantities of water and rock progressively react. An increase in reaction progress is akin to an increase in the rock-to-water ratio, as the reacting water encounters more rock while infiltrating into the subsurface. These equilibrium calculations, although idealized, allow us to adequately track changes in fluid chemistry during rock alteration as demonstrated by the above-mentioned studies on various sites of active serpentinization. The reaction path code EQ6 (Wolery and Jarek, 2003) was used for calculations in this study, together with a customized thermodynamic database (see below). A global average modern rainwater composition compiled by Hao and others (2017) from Berner and Berner (2012) was used as the starting reacting fluid. We modified the pH and DIC from this compilation slightly to be in equilibrium with modern atmospheric $CO_{2(g)}$ levels. Details about the composition of this starting rainwater can be found in table A1. As illustrated in figure 1, our calculations include both *open* and *closed* systems, related to those simulated by Cipolli and others (2004) and Paukert and others (2012). Water-rock interactions first proceed in a system *open* to atmospheric exchange, simulating conditions when fluids are in the shallow subsurface or close to the surface. At some point in the reaction progress, fluids infiltrate deeper into the subsurface where conditions are *closed* to atmospheric influence and input from atmosphere-derived volatiles such as $CO_{2(g)}$ and $O_{2(g)}$ ceases. Temperature and pressure conditions remain near ambient (25 °C, 1 bar) in our initial models of low-temperature continental serpentinizing systems.

As in the case of kinetically enabled models by Paukert and others (2012), simulations were run using a fluid-centered, flow-through system where compositions

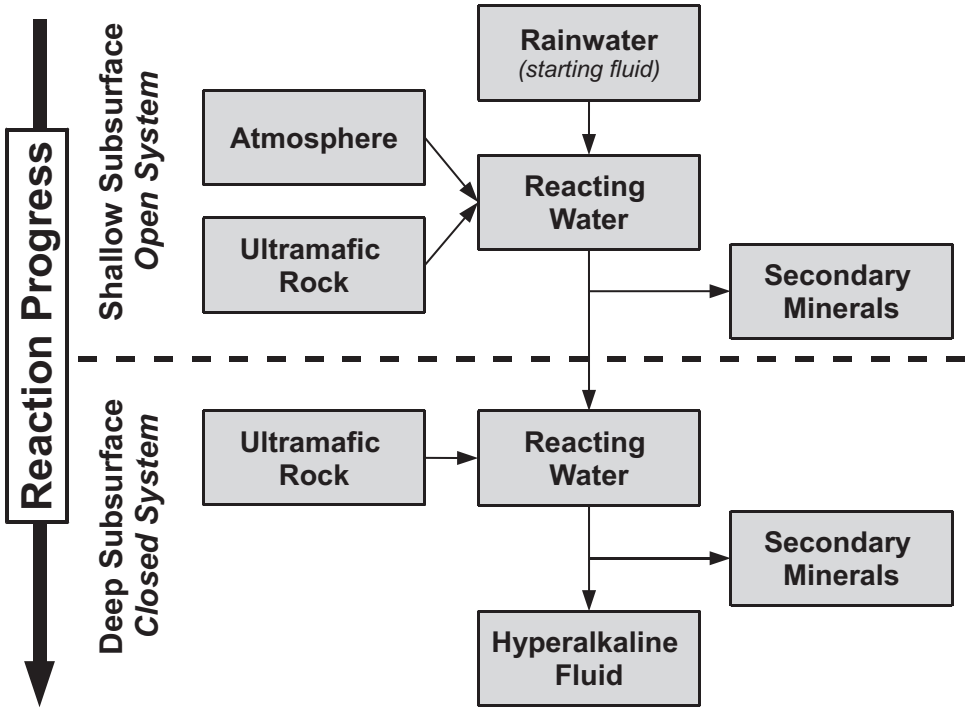

Fig. 1. Schematic of a fluid-centered flow-through model, as modified from Paukert and others (2012), showing transition from a system *open* to the atmosphere to one *closed* to atmosphere-derived volatiles as the overall serpentinization reaction progresses.

are tracked as reactive fluid moves through an aquifer. However, instead of using experimentally-derived dissolution rates, in this study inputs from primary minerals are controlled by relative dissolution rates to explore effects of variable contributions of primary minerals to changes in fluid composition. Compositions of reacting rocks used in our simulations are listed in table 2. We first simulate rainwater interactions with an idealized ultramafic rock (Model A) with a composition typical of an ophiolitic harzburgite (Hanghoj and others, 2010) with 85 mol% olivine (X_{Mg} = Mg/(Mg+Fe) = 0.9, Forsterite$_{90}$ or Fo$_{90}$), 14 mol% orthopyroxene (X_{Mg} = 0.9, Enstatite$_{90}$ or En$_{90}$), and 1 mol% clinopyroxene (X_{Mg} = 0.95, Diopside$_{95}$ or Di$_{95}$). The resulting reaction paths are divided into various stages to explore, step by step, the reactions that drive the transformation of rainwater to hyperalkaline fluids. We then explore further the consequences of reactions with rocks composed of variable amounts of primary minerals (Models B1-B5 and C1-C5) as well as with previously altered ultramafic rocks (serpentinites, Models D1-D4). To facilitate discussions in terms of idealized reactions using end-member phases, we first report results of simulations without considering the precipitation of secondary minerals as solid solutions. Later in the discussion, we report the consequences of incorporating solid solutions into our models. Effects of variable temperature and salinity were also explored, as well as the precipitation of various Ca-bearing phases, as discussed below.

Thermodynamic data used in the calculations were calculated with the SUPCRT code (Johnson and others, 1992) using standard state thermodynamic data for aqueous species taken from Shock and Helgeson (1988), Shock and others (1989,

TABLE 2

Compositions of reacting rocks used in this study and figures where results of each model appear

Model	Rock Name	Composition[1]
	Model A: Generalized Model (figures 2-3, 7F, 8-11)	
A	Harzburgite	85% Olivine-14% Orthopyroxene-1% Clinopyroxene
	Model B: Alteration of olivine- and orthopyroxene-bearing rocks (figures 7A-7E)	
B1	Dunite	100% Olivine
B2	Harzburgite	75% Olivine-25% Orthopyroxene
B3	Harzburgite	50% Olivine-50% Orthopyroxene
B4	Orthopyroxenite	25% Olivine-75% Orthopyroxene
B5	Orthopyroxenite	100% Orthopyroxene
	Model C: Alteration in the presence of clinopyroxene (figures 8-9, 12)	
C1	Harzburgite	85% Olivine-10% Orthopyroxene-5% Clinopyroxene
C2	Harzburgite	75% Olivine-20% Orthopyroxene-5% Clinopyroxene
C3	Harzburgite	65% Olivine-30% Orthopyroxene-5% Clinopyroxene
C4	Harzburgite	45% Olivine-50% Orthopyroxene-5% Clinopyroxene
C5	Orthopyroxenite	35% Olivine-60% Orthopyroxene-5% Clinopyroxene
	Model D: Alteration of serpentinites (figure 9B)	
D1	Serpentinite	95% Serpentine-5% Clinopyroxene
D2	Serpentinite	75% Serpentine-20% Brucite-5% Clinopyroxene
D3	Serpentinite	65% Serpentine-30% Brucite-5% Clinopyroxene
D4	Serpentinite	55% Serpentine-40% Brucite-5% Clinopyroxene

[1]Compositions of reacting minerals are in solid solutions. X_{Mg}: olivine - 0.90; orthopyroxene - 0.90; clinopyroxene - 0.95, serpentine - 0.95; brucite - 0.90.

1992, 1997), Sverjensky and others (1997), together with the revised Helgeson-Kirkham-Flowers equations of state (Shock and others, 1992) and data for minerals taken from Helgeson and others (1978) and Wolery and Jove-Colon (2004). In addition, data for several minerals were added, while maintaining internal thermodynamic consistency, to explore solid solution behavior during serpentinization. New data are summarized in table A2, which also includes a discussion of data sources. In models where the precipitation of secondary phases in solid solutions are allowed, the calculations account for ideal solid solution substitution of the iron endmembers with their Mg endmember counterparts. Serpentine usually occurs as lizardite or chrysotile at low-temperature environments. Because differences in the thermodynamic properties between these two serpentine polymorphs are minor (Evans, 2004; Frost and Beard, 2007) we used chrysotile to represent the Mg-end member of serpentine. In some of our calculations, we suppressed the precipitation of certain minerals. These suppressed minerals and the reasons for suppression are explained in the discussions of model results. Primary and secondary minerals, including solid solutions modeled in this study, are listed in table 3.

THERMODYNAMIC CONSTRAINTS ON THE EVOLUTION OF FLUIDS DURING LOW-TEMPERATURE SERPENTINIZATION

Results of calculations simulating the serpentinization of the model ultramafic rock introduced above (Model A, 85% olivine, 14% orthopyroxene, 1% clinopyrox-

TABLE 3

List of minerals included in this study

Mineral[1]	Abbreviation[2]	Formula
	Primary Minerals	
Forsterite (*Olivine*)	Fo	Mg_2SiO_4
Fayalite (*Olivine*)	Fa	Fe_2SiO_4
Enstatite (*Orthopyroxene*)	En	$MgSiO_3$
Ferrosilite (*Orthopyroxene*)	Fs	$FeSiO_3$
Diopside (*Clinopyroxene*)	Di	$CaMgSi_2O_6$
Hedenbergite (*Clinopyroxene*)	Hd	$CaFeSi_2O_6$
	Secondary Minerals	
Chrysotile (*Serpentine*)	Ctl	$Mg_3Si_2O_5(OH)_4$
Greenalite (*Serpentine*)	Gre	$Fe_3Si_2O_5(OH)_4$
Mg-Cronstedtite (*Serpentine*)	Mg-Cro	$Mg_2Fe(FeSiO_5)(OH)_4$
Hisingerite (*Serpentine*)[3]	His	$Fe_2Si_2O_5(OH)_4$
Talc (*Talc*)	Tlc	$Mg_3Si_4O_{10}(OH)_2$
Minnesotaite (*Talc*)	Mns	$Fe_3Si_4O_{10}(OH)_2$
Brucite (*Brucite*)	Brc	$Mg(OH)_2$
Ferroan Brucite (*Brucite*)	Fe-Brc	$Fe(OH)_2$
Tremolite (*Amphibole*)	Tr	$Ca_2Mg_5Si_8O_{22}(OH)_2$
Ferrotremolite (*Amphibole*)	Fe-Tr	$Ca_2Fe_5Si_8O_{22}(OH)_2$
Goethite	Gth	$FeO(OH)$
Magnetite	Mag	Fe_3O_4
Dolomite	Dol	$CaMg(CO3)_2$
Magnesite	Mgs	$MgCO_3$
Calcite	Cal	$CaCO_3$
Andradite	Adr	$Ca_3Fe_2Si_3O_{12}$
Portlandite	Por	$Ca(OH)_2$

[1]If shown, minerals in italics indicate name of solid solution. All reacting primary minerals used in our models are in solid solutions. For compositions of primary phases, see Table 2.

[2]Mineral abbreviations follow recommendations by Whitney and Evans (2010). Minerals not included in Whitney and Evans (2010) are abbreviated using the first three letters of the minerals.

[3]The dehydrated version of hisingerite ($Fe_2Si_2O_5(OH)_4 \cdot nH_2O$, n=0) was used in this study.

ene) are shown in figures 2 and 3, and provide a framework for depicting the predicted consequences. The resulting reaction paths are divided into six stages to explore, step by step, the reactions that drive the transformation of acidic rainwater to hyperalkaline fluids. The numbers in circles in figures 2 and 3 indicate the starting points of various stages of the overall reaction progress. Figure 2A depicts these six stages in a generalized schematic diagram for a subsurface flowpath in an ultramafic aquifer. Note that the transition from shallow to deep subsurface settings described in figure 1 occurs in stage 3. Calculated changes in pH with reaction progress are shown in figure 2B. Precipitating minerals and compositions of fluids at each stage of the overall reaction progress are summarized in figure 2C and are described in detail in the following discussion. Changes in the total concentrations of Ca, Mg, Si, Fe and dissolved inorganic carbon (DIC), as well as the number of moles of secondary minerals produced or consumed are shown in figure 3. Also shown in figure 3 are activity diagrams that depict the stabilities of minerals relative to the activities of aqueous solutes, together with the reaction paths. Unless otherwise stated, compositions of fluids (including pH) and solid precipitates are results of calculations simulating ambient conditions (25 °C, 1 bar).

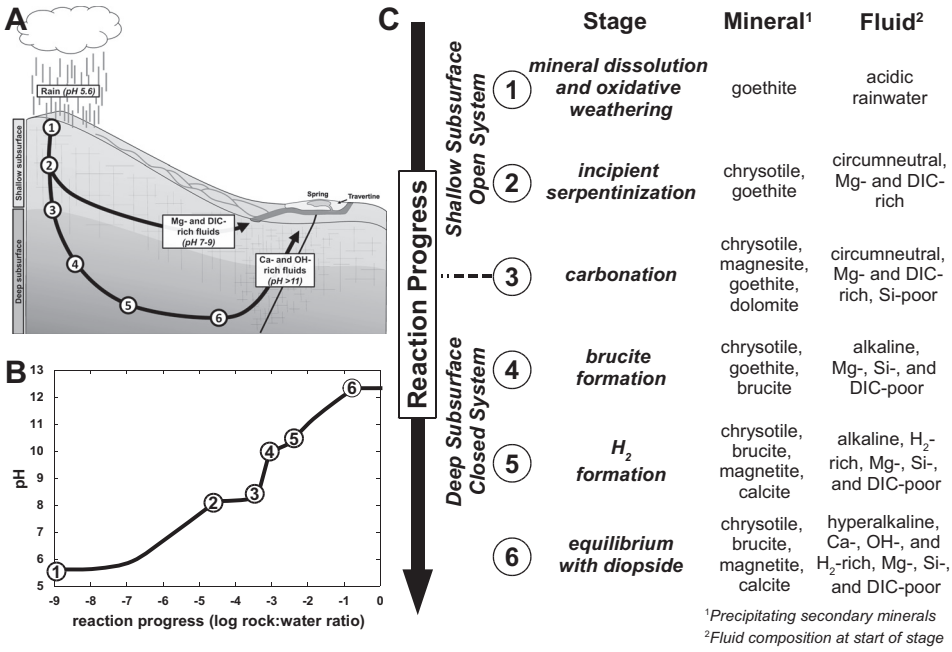

Fig. 2. The progress of the overall serpentinization reaction is divided into six stages that depict conversion of meteoric water into evolved fluids (Types 1 and 2). The numbers in circles indicate the starting points of these stages. (A) depicts these stages in the generalized subsurface reaction scheme shown in figure 1. (B) shows the evolution of pH during the overall reaction progress at 25 °C and 1 bar. (C) summarizes precipitating minerals and fluid compositions at each stage of the overall serpentinization reaction progress. Note that stage 3 marks the transition from shallow to deep subsurface environments.

Stages in Reaction Progress

Stage 1, dissolution of primary minerals into rainwater.—The first stage of reaction progress begins when rainwater interacts with the rocks. At initial stages of reaction progress, the model system is *open* to the atmosphere, simulating rainwater interacting with rocks in the surface or shallow subsurface. The primary minerals that compose ultramafic rocks, formed at mantle temperatures and pressures, are unstable at the surface in the presence of rain and the atmosphere and consequently alter into secondary phases. Rainwater is slightly acidic (pH ~ 5.6) and contains H^+ derived from atmospheric $CO_{2(g)}$ via

$$CO_{2(g)} + H_2O \rightarrow HCO_3^- + H^+ \quad (1)$$

which drives the dissolution of primary minerals present in ultramafic rocks as described by the reactions

$$Mg_2SiO_{4(\text{forsterite})} + 4H^+ \rightarrow 2Mg^{+2} + SiO_{2(aq)} + 2H_2O, \quad (2)$$

$$MgSiO_{3(\text{enstatite})} + 2H^+ \rightarrow Mg^{+2} + SiO_{2(aq)} + H_2O, \text{ and} \quad (3)$$

$$CaMgSi_2O_{6(\text{diopside})} + 4H^+ \rightarrow Ca^{+2} + Mg^{+2} + 2SiO_{2(aq)} + 2H_2O. \quad (4)$$

As shown in figure 2B, progress of these reactions drives pH to higher values owing to the continuous consumption of H^+ during mineral hydrolysis. The dissolution of the primary minerals also releases solutes into the fluid, which increases their total

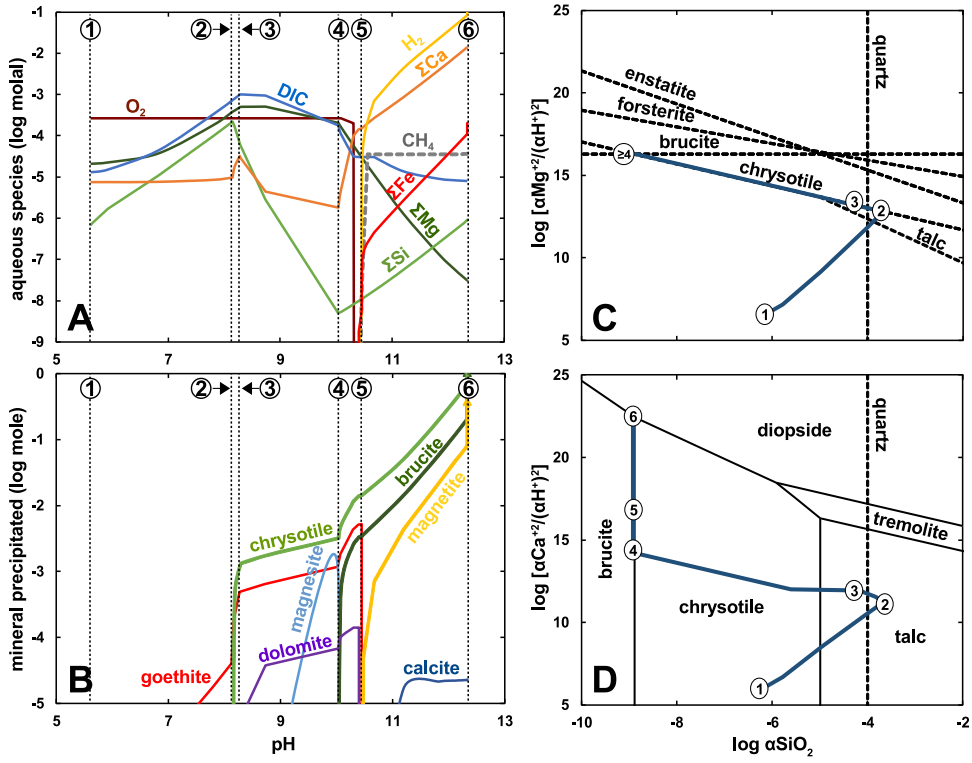

Fig. 3. Evolution of (A) aqueous compositions and (B) secondary precipitation as pH increases with overall reaction progress at 25 °C and 1 bar. Fluid evolution is also depicted on activity diagrams for the (C) MgO-SiO_2-H_2O and (D) CaO-MgO-SiO_2-H_2O systems. The numbers in circles indicate the starting points of various stages of overall reaction progress as in fig. 2C. Note that mineral saturation is indicated by dashed lines in (C) and (D), while solid lines in (D) represent boundaries for the stability fields of minerals.

concentrations relative to rainwater as illustrated in figure 3A. At conditions open to the atmosphere, the concentration of dissolved inorganic carbon (DIC) is controlled by atmospheric $CO_{2(g)}$ levels. At a constant atmospheric fugacity, $fCO_{2(g)}$, HCO_3^- and DIC must increase with pH (decrease in H^+) for reaction (1) to proceed. This increase in DIC early in the reaction progress is shown in figure 3A. Ultimately, reactions (1 – 4) facilitate the transformation of dilute, acidic rainwater into a circumneutral fluid mostly enriched in Mg and DIC.

Reactions (2 – 4) refer to the Mg endmembers of natural mineral compositions that are solid solutions. The Mg endmembers provide a framework for illustrating the reactions discussed throughout this section. It should be kept in mind that dissolution of natural ultramafic minerals will also release Fe^{+2}, which often substitutes for Mg^{+2} in minerals. As shown in figure 3B, Fe^{+2} released to the fluid can be oxidized by O_2 to form an oxyhydroxide such as goethite (FeOOH), through

$$4Fe^{+2} + O_{2(g)} + 6H_2O \rightarrow 4FeO(OH)_{(goethite)} + 8H^+. \quad (5)$$

As goethite precipitates, total Fe concentrations stay at low values that plot below the concentration range of most of figure 3A. Throughout the overall reaction progress, O_2 consumption and oxidative weathering proceed through reaction (5) only. Ferric iron-bearing phases like hematite and other ferric oxyhydroxides are also known to

occur in serpentinizing systems (Alt and Shanks, 2003; Mayhew and others, 2018). Precipitation of these phases would result in similarly low values of dissolved Fe as those shown in figure 3A owing to their low solubilities. The fluid accumulates other major solutes (Mg, Ca, Si) from mineral dissolution, until they are concentrated enough for minerals to saturate. Increases in total dissolved concentrations of the above solutes are accompanied by increases in the activity ratios of Mg^{+2} and Ca^{+2} to H^+ [$\alpha Mg^{+2}/(\alpha H^+)^2$ and $\alpha Ca^{+2}/(\alpha H^+)^2$, respectively], as well as the activity of $SiO_{2(aq)}$ [$\alpha SiO_{2(aq)}$] as illustrated by reaction paths on activity diagrams shown in figure 3C, for the MgO-SiO_2-H_2O system, and 3D for the CaO-MgO-SiO_2-H_2O system. Note that mineral saturation is indicated by dashed lines in figures 3C and 3D, while solid lines in figure 3D represent boundaries for the stability fields of minerals. At a point during Stage 1 of reaction progress, as shown by the reactions paths in figures 3C and 3D, $\alpha SiO_{2(aq)}$ is high enough to saturate quartz and talc. These minerals, however, are rarely encountered in low-temperature serpentinites and were suppressed in the model to evaluate the maximum concentrations that Mg and Si can attain before the fluid reaches chrysotile saturation.

Stage 2, the onset of serpentinization.—The maximum values of $\alpha SiO_{2(aq)}$ and total dissolved Si are reached at Stage 2 where the reaction path encounters the chrysotile saturation line, at which point chrysotile begins to precipitate in the model via

$$3Mg^{+2} + 2SiO_{2(aq)} + 5H_2O \rightarrow Mg_3Si_2O_5(OH)_{4(chrysotile)} + 6H^+. \quad (6)$$

In response to the precipitation of chrysotile, the total dissolved Si decreases as shown in figure 3A. Correspondingly, as illustrated in figure 3C, when chrysotile saturation is attained, the reaction path turns and $\alpha SiO_{2(aq)}$ decreases along the chrysotile saturation line. Despite the consumption of Mg in reaction (6), continued dissolution of ultramafic phases means that the total dissolved Mg continues to increase in concentration. As an example, dissolution of olivine-dominated lithologies results in a surplus of Mg with respect to Si taken up during serpentinization as depicted by

$$2Mg_2SiO_{4(forsterite)} + 2H^+ + H_2O \rightarrow Mg_3Si_2O_5(OH)_{4(chrysotile)} + Mg^{+2}. \quad (7)$$

Trends in pH result from reactions consuming and releasing H^+ into the fluid. In Stage 1 of reaction progress, dissolution of primary minerals consumes H^+ (rxns 2 – 4), and reactions that release H^+ include precipitation of secondary goethite (rxn 5), as well as the continuing dissolution of atmospheric $CO_{2(g)}$ (rxn 1) into the fluid. Released H^+, in turn, drives the dissolution of primary minerals (rxns 2 – 4) allowing reaction progress to proceed. As shown in figures 2 and 3, the increasing trends in pH means that dissolution reactions prevail over reactions that release H^+. The precipitation of chrysotile (rxn 6) at the start of Stage 2 provides another source for H^+, which dampens the increasing pH trend observed since the start of Stage 1 (see fig. 2B). However, pH continues to increase, as production of H^+ through reaction (6) is not enough to balance its consumption through reactions (2 – 4). The overall process is exemplified by reaction (7), which depicts the overall process of forsterite dissolution and chrysotile precipitation (sum of rxns 2 and 6) and results in a net consumption of protons.

Stage 3, atmosphere out, carbonates in.—As the fluid infiltrates deeper into the aquifer, it loses contact with the atmosphere as it continues to react with the rock. At the start of Stage 3, our calculations simulate a transition from an open shallow subsurface setting to a deep subsurface environment closed to atmospheric input. As shown in figure 3A, DIC stops increasing without the atmosphere supplying $CO_{2(g)}$. Consequently, as illustrated in figure 2B, pH increases dramatically without additional H^+ provided by reaction (1). Increasing pH and concentrations of divalent cations

(Mg^{+2} and Ca^{+2}) will saturate carbonate minerals. As shown in figures 3A and 3B, the first carbonate predicted to precipitate is dolomite via the reaction

$$Mg^{+2} + Ca^{+2} + 2HCO_3^- \rightarrow (CaMg)(CO_3)_{2(dolomite)} + 2H^+ \quad (8)$$

which causes DIC and total dissolved Ca to decrease in response to dolomite precipitation. The next carbonate predicted to saturate, and in greater quantity than dolomite, is magnesite via the reaction

$$Mg^{+2} + HCO_3^- \rightarrow MgCO_{3(magnesite)} + H^+ \quad (9)$$

which causes a slight decrease in the total dissolved Mg concentration.

During Stage 3, as shown in the reaction paths depicted in the activity diagrams shown in figures 3C and 3D, the decrease in $\alpha SiO_{2(aq)}$ that started when chrysotile first precipitated at the beginning of Stage 2 continues. Despite the overall decrease in total Mg owing to dolomite, magnesite and chrysotile precipitation, the increase in pH is abrupt enough to cause the $\alpha Mg^{+2}/(\alpha H^+)^2$ to increase gently along the chrysotile saturation line (fig. 3C). The abrupt increase in pH also causes the $\alpha Ca^{+2}/(\alpha H^+)^2$ to increase slightly as the $\alpha SiO_{2(aq)}$ decreases (fig. 3D).

Stage 4, brucite in, magnesite and dolomite out.—At Stage 4 of the overall reaction progress, pH is high enough to saturate brucite via

$$Mg^{+2} + 2H_2O \rightarrow Mg(OH)_{2(brucite)} + 2H^+. \quad (10)$$

Reaction (10) provides a new source for protons ending the dramatic increase in pH observed since the start of Stage 3 (fig. 2B). However, the dissolution reactions (rxns 2 – 4) that consume H^+ continue, allowing pH to increase more gradually than during Stage 3. As shown in figures 3A and 3B, total dissolved Mg decreases abruptly in response to brucite precipitation. The continuous decreases in total Mg and DIC cause magnesite and eventually dolomite to become unstable and neither precipitates henceforth. Additionally, as depicted in figure 3C, the trend of decreasing $\alpha SiO_{2(aq)}$ observed since the onset of serpentinization at Stage 2 stops when the reaction path attains brucite saturation at the point where the brucite and chrysotile saturation lines intersect. A major implication is that a fluid in equilibrium with both chrysotile and brucite will always remain undersaturated with respect to forsterite and enstatite, ultimately driving the total dissolution of these primary minerals. Totally serpentinized ultramafic rocks, where no relict olivine and orthopyroxene survive, are not uncommon in ultramafic settings (for example, see Oufi and others, 2002; Klein and others, 2014). Forsterite only becomes stable relative to chrysotile and brucite at temperatures > 350 °C (see Klein and others, 2013).

As depicted in figure 3C, the $\alpha Mg^{+2}/(\alpha H^+)^2$ becomes constant when the reaction path reaches the horizontal brucite saturation line corresponding to reaction (10). Moreover, the equilibrium assemblage of brucite and chrysotile will also set the $\alpha SiO_{2(aq)}$ as defined by the reaction

$$3Mg(OH)_{2(brucite)} + 2SiO_{2(aq)} \rightarrow Mg_3Si_2O_5(OH)_{4(chrysotile)} + H_2O, \quad (11)$$

which is the sum of reactions (6) and (10). At 25 °C and 1 bar, reaction (11) will yield a low $\alpha SiO_{2(aq)}$ of $10^{-8.9}$. Despite the $\alpha SiO_{2(aq)}$ being fixed by reaction (11), the speciation of Si allows an increase in total dissolved Si, as depicted in figure 3A, because the abundance of $HSiO_3^-$ increases with increasing pH via the reaction

$$SiO_{2(aq)} + H_2O \rightarrow HSiO_3^- + H^+. \quad (12)$$

Reaction (12) allows total dissolved Si to increase with increasing pH while maintaining the fixed $\alpha SiO_{2(aq)}$ imposed by reaction (11).

Along the reaction path depicted in the activity diagram shown in figure 3D, Stage 4 starts at the boundary between the brucite and chrysotile stability fields. The reaction path follows this boundary as the $\alpha Ca^{+2}/(\alpha H^{+})^{2}$ continues to increase with reaction progress owing to increases in both pH, shown in figure 2B, and total dissolved Ca concentration shown in figure 3A. This point marks the transition from a *Type 1* fluid dominated by Mg and HCO_3^- to a *Type* 2 fluid dominated by Ca^{+2} and OH^-, which are the characteristic fluids found in serpentinizing systems.

Stage 5, rise of a reduced fluid.—As fluid moves deeper into the subsurface, atmosphere-derived volatiles such as $O_{2(g)}$ and $CO_{2(g)}$ are exhausted, demarcating the start of Stage 5 of the overall reaction progress. At this point, H_2O becomes the main oxidant, generating H_2 through the oxidation of ferrous iron in primary minerals to ferric iron in secondary minerals via

$$2Fe^{+2}O_{(\text{primary minerals})} + H_2O \rightarrow Fe_2{}^{+3}O_{3(\text{secondary minerals})} + H_{2(aq)}. \quad (13)$$

Progress of reaction (13) causes the fluid to become more reduced with the continuous addition of H_2. This destabilizes goethite which is replaced by magnetite as the only Fe-bearing precipitate in this initial round of modeling because solid solution models of serpentine and brucite were not included. The consequences of allowing solid solutions to form is explored below. Moreover, as shown in figure 3A, continuous addition of H_2 will generate a concentration of dissolved H_2 close to 100 millimolal by the end of Stage 5. This is 100 times as much dissolved H_2 as would be in equilibrium with 1 atmosphere of $H_{2(g)}$ at ambient conditions (~1 millimolal dissolved H_2), suggesting an overpressurized system capable of generating a free $H_{2(g)}$ phase. Further calculations incorporating constraints on confining pressures in deep subsurface aquifers can quantify the proportion of H_2 present as a free gas. This evaluation can provide insights into the habitability of serpentinizing subsurface as free H_2 is believed to promote formation of CH_4 (McCollom, 2016; Etiope and Whiticar, 2019).

As conditions become increasingly reduced, CH_4 formation is thermodynamically favorable and the concentration of DIC (represented by the species $CO_3{}^{-2}$ at this pH condition) will decrease if the reaction

$$CO_3{}^{-2} + 4H_{2(aq)} + 2H^+ \rightarrow CH_{4(aq)} + 3H_2O \quad (14)$$

is not kinetically inhibited. Such a scenario is depicted as a downward dashed arrow from the DIC curve in figure 3A. This downward trend for DIC does not occur if kinetic barriers for reaction (14) exist and DIC will remain in solution, albeit at low concentrations. DIC can then precipitate to yield calcite via

$$Ca^{+2} + CO_3{}^{-2} \rightarrow CaCO_{3(\text{calcite})} \quad (15)$$

when pH and the total dissolved Ca are high enough, as shown in figures 3A and 3B. A kinetic inhibition to abiotic methane generation opens the possibility for microbial methanogenesis, as discussed below.

Stage 6, chrysotile-brucite-diopside equilibria.—Since the beginning of Stage 1 through the end of Stage 5, pH continues to increase transforming slightly acidic rainwater into an increasingly alkaline fluid. The increase in pH is driven by the consumption of H^+ through the dissolution of primary minerals (rxns 2 – 4). Precipitation of secondary minerals releases H^+, and, in turn, increases the extent of the dissolution reactions. So far, the release of H^+ from precipitation reactions is not enough to counter its consumption during dissolution reactions resulting in an overall net consumption of H^+ that drives the increasing pH trend shown in figure 2B. Note that as the fluid becomes more alkaline, reactions depicted in this paper could be written using the species OH^- instead of H^+. Nonetheless, rewriting the above reactions into those that

release and consume OH^- for dissolution and precipitation reactions, respectively, would still result in the same trends in the pH and concentrations of aqueous species shown in figures 2 and 3.

In a system involving only forsterite as the dissolving primary mineral, the increase in pH stops when the overall reaction progress precipitates both chrysotile and brucite as depicted by the reaction

$$2Mg_2SiO_{4(\text{forsterite})} + 3H_2O \rightarrow Mg_3Si_2O_5(OH)_{4(\text{chrysotile})} + Mg(OH)_{2(\text{brucite})}. \quad (16)$$

Reaction (16) describes the overall reaction for the dissolution of forsterite (rxn 2), and the precipitation of chrysotile (rxn 6) and brucite (rxn 10). As Reaction (16) does not result in a net consumption or production of H^+, pH will remain constant once chrysotile and brucite are both precipitating. The maximum pH this system can attain is that reached at the start of stage 4 (pH ~ 10) where brucite joins chrysotile in the secondary assemblage. Addition of enstatite will favor the formation of chrysotile over that of brucite, as exemplified by the reaction

$$3Mg_2SiO_{4(\text{forsterite})} + MgSiO_{3(\text{enstatite})} + 5H_2O \rightarrow 2Mg_3Si_2O_5(OH)_{4(\text{chrysotile})} + Mg(OH)_{2(\text{brucite})}. \quad (17)$$

However, as both chrysotile and brucite are still precipitating, the pH would still be constrained by the chrysotile-brucite equilibria and would still end up like that predicted for reaction (16).

It is the dissolution of diopside (rxn 4) that further drives the pH into hyperalkaline conditions (pH > 11). Mg^{+2} and $SiO_{2(aq)}$ released through the dissolution of diopside can be consumed through the precipitation of Mg- and Si-bearing minerals such as chrysotile, dolomite, magnesite, and brucite. Ca^{+2} released by the dissolution of diopside (rxn 4) can be potentially balanced by the precipitation of Ca-bearing phases such as dolomite (rxn 8) or calcite (rxn 15), but the minimal and continuously decreasing amount of DIC is not enough for reactions (8) and (15) to consume all of the Ca^{+2} released through reaction (4). Unbalanced Ca^{+2} will be accommodated by the consumption of H^+ (or, conversely, release of OH^-), and thus pH continues to increase.

At some point in the overall reaction progress, the increase in pH will stop. This occurs when the fluid approaches equilibrium with diopside, which means that reaction (4) stops going forward. As depicted in figure 3D, this occurs when the reaction path reaches the invariant point defined by the equilibrium assemblage of chrysotile, brucite, and diopside (Ctl-Brc-Di), as described by the reaction

$$CaMgSi_2O_{6(\text{diopside})} + 2Mg(OH)_{2(\text{brucite})} + 2H^+ \leftrightarrow Ca^{+2} + Mg_3Si_2O_5(OH)_{4(\text{chrysotile})} + H_2O. \quad (18)$$

As this is an invariant point in the CaO-MgO-SiO_2-H_2O system, not only the pH (fig. 2B) but also the total dissolved Ca, Mg, and Si (fig. 3A) will remain unchanged despite continuous reaction progress, until diopside is completely reacted. As fluids attain compositions dictated by this triple point, they are as close as possible to being in equilibrium with the host aquifer rocks, and defining the final stage, Stage 6, of overall reaction progress.

Fluid composition attained at Stage 6 of overall reaction progress is shown in figure 3A and corresponds to reduced, Ca-OH fluid with hyperalkaline pH (pH ~12), elevated levels of total dissolved Ca (~10 millimolal), and dilute concentrations of total dissolved Si (~1 μmolal) and Mg (<1 μmolal). As an example, the pH can be

derived using reaction (18), which, at 25 °C and 1 bar, has an equilibrium constant of $10^{22.4}$. An equilibrium constant expression for reaction (18), assuming activities of pure solids and water at unity, is given by

$$K_{18} = \frac{\alpha Ca^{+2}}{(\alpha H^{+})^{2}} = 10^{22.4}, \tag{19}$$

and, incorporating an ionic balancing constraint

$$\alpha Ca^{+2} = 0.5\alpha OH^{-} = 0.5\frac{10^{-14}}{\alpha H^{+}}, \tag{20}$$

will yield a pH of ~12 at 25 °C and 1 bar. Equation (20) is a simplified illustration compared with our calculations that account for full aqueous speciation and ionic balance. Further constraints via reaction (15, calcite precipitation) will allow the prediction of DIC concentrations. As shown in figure 3A, an equilibrium assemblage of Ctl-Brc-Di and calcite results in a predicted fluid with very low concentrations of DIC (<10 μmolal).

In summary, Stage 6 of the overall reaction progress corresponds to the final step in which the infiltrating fluid attains its maximum pH. Fluid composition imposed by the above assemblage of minerals results in a hyperalkaline fluid with elevated total concentrations of Ca, and dilute levels of total Mg, Si and DIC (see fig. 3A). Such equilibria also impose limits on the maximum pH that can be attained by a serpentinizing system. At ambient conditions (25 °C, 1 bar) this yields a pH close to 12. This and other results discussed in this section have strong or subtle temperature dependencies as discussed next.

Variations in Temperature

The models described above simulate water-rock interactions at ambient conditions (25 °C, 1 bar). Continental serpentinizing fluids reported in the literature range in temperature up to ~50 °C. Although yet to be sampled, serpentinizing fluids at higher temperatures up to ~100 °C could exist deep in an ophiolite aquifer, assuming ophiolite thickness of 3 to 4 km and a geotherm of 30 °C km^{-1}. To explore the chemistry of serpentinization-generated fluids that can form at various low temperatures, fluid compositions constrained by Ctl-Brc-Di plus calcite were calculated at temperatures ranging from 0 °C to 100 °C. Results are shown in figure 4, including trends in pH, total dissolved Ca, Si, Mg, and DIC, and their speciated components over this temperature range. In the following discussion, note that the temperatures for calculated or measured pH values are indicated in subscripts.

The pH of a fluid in equilibrium with chrysotile, brucite, diopside, and calcite will decrease as temperature increases, as shown in figure 4A. The calculated pH at 100 °C ($pH_{100°C}$ = 10.1) is more than 3 pH units lower than that calculated at 0 °C ($pH_{0°C}$ = 13.4). The latter is close to the $pH_{2.4°C}$ (13.1) calculated at *in situ* temperatures at South Chamorro Seamount (Mottl, 2009). Mottl (2009) argued that this extremely high pH is attained through the release of OH^{-} (or conversely, consumption of H^{+}) during the reduction of DIC to generate CH_4 (see rxn 14). Alternatively, this high pH could result from fluid-mineral equilibria as it is close to that predicted for equilibrium with Ctl-Brc-Di (fig. 4A). On the continents, high pH values were measured in fluids hosted in Canadian kimberlite deposits (12.46, Sader and others, 2007), the Tablelands Ophiolite in Canada (12.2, Szponar and others, 2013), Coast Range Ophiolites Microbial Observatory (CROMO) in California, USA (12.4, Crespo-Medina and others, 2014), Voltri Massif in Italy (12.3, Schwarzenbach and others, 2013), Samail Ophiolite in Oman (12, Chavagnac and others, 2013b), and the Dinaride Ophiolite in

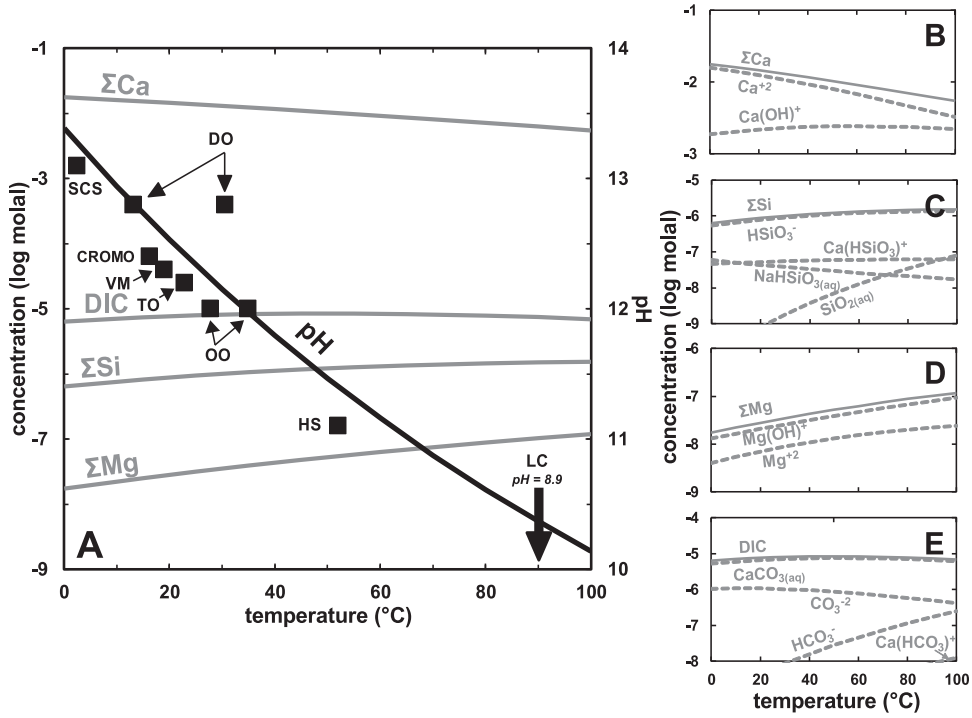

Fig. 4. (A) Trends of pH and total dissolved solute concentrations, as constrained by equilibrium with Ctl-Brc-Di (rxn 18) and Cal (rxn 15) at temperatures ranging from 0 °C to 100 °C (see table 3 for abbreviations of minerals). Also shown are the calculated speciations of (B) ΣCa, (C) ΣSi, (D) ΣMg, and (E) DIC. Plotted in (A) are some of the highest pH measured in serpentinizing systems (black squares): South Chamorro Seamount (SCS, Mottl, 2009); Coast Range Ophiolites, California (CROMO, Crespo-Medina and others, 2014); Voltri Massif, Italy (VM, Schwarzenbach and others, 2013); Oman Ophiolite (OO, Chavagnac and others, 2013b); Dinaride Ophiolite, Bosnia and Herzegovina (DO, Etiope and others, 2017); Tablelands Ophiolite, Canada (TO, Szponar and others, 2013); Hakuba Happo Springs, Japan (HS, Homma and Tsukahara, 2008); and Lost City Hydrothermal Field, Mid-Atlantic Ridge (LC, Seyfried and others, 2015). pH values for SCS and LC were measured at 25 °C and were recalculated to *in situ* temperatures by Mottl (2009) for SCS and by this work using data from Seyfried and others (2015) for LC.

Bosnia and Herzogovina (12.8, Etiope and others, 2017). Measured pH of 12 (Oman), 12.2 (Tablelands), 12.3 (Voltri), 12.4 (CROMO) and 12.8 (Dinaride) at temperatures of 34.9 °C, 21.3–24.3 °C, 19 °C, 16.2 °C, and 13.1 °C, respectively, are close to those predicted for the Ctl-Brc-Di equilibria (fig. 4A). A $pH_{30.5°C}$ measurement of 12.8 at Dinaride, which is 0.7 pH units above that imposed by Ctl-Brc-Di equilibria could have been produced through reduction reactions that generate CH_4, as Mottl (2009) postulated for the South Chamorro Seamount fluid. The CH_4 concentration (2706 μM) associated with this sample is the highest recorded so far in ultramafic-hosted hyperalkaline fluids (Etiope and others, 2017). Alternatively, this high pH could be a result of mineral buffering reactions other than the Ctl-Brc-Di equilibria. High pH values (~12.5) were measured from slag-filled aquifer fluids in Lake Calumet, Chicago, Illinois (Roadcap and others, 2005, 2006; Ohlsson and others, 2019) and even more basic pH values were observed in Maqarin, Jordan (Barnes and others, 1982; Khourey and others, 1985, 1992; Alexander and others, 1992; Pederson and others, 2004). These sites are not hosted in ultramafic rocks and the high pH is likely a result of mineral equilibria akin to that resulting from concrete-water interactions rather than by the Ctl-Brc-Di equilibria attained during the serpentinization of ultramafic

rocks. As an example, the $\alpha Ca^{+2}/(\alpha H^{+})^{2}$ of a fluid constrained by portlandite and high Ca/Si hydrate (CSH) phases is higher than typically seen in serpentinizing fluids, owing to both higher pH and total dissolved Ca (Blanc and others, 2010). In addition to portlandite and CSH phases, fluid in equilibrium with calcite at extremely DIC-limited environments would require very high pH, as expounded upon below. These examples underscore the fact that hyperalkaline fluids are not unique to serpentinization-related environments and other fluid-rock processes that buffer pH to high values also exist.

Temperatures slightly exceeding 50 °C, perhaps the highest measured in continental serpentinizing systems, were recorded by Homma and Tsukahara (2008) and Suda and others (2014) in Hakuba Happo Hot Springs, Japan. The highest reported $pH_{52°C}$ for this area is 11.1 (Homma and Tsukahara, 2008) which is also close to that constrained by the Ctl-Brc-Di equilibrium. Taran and othes (2002, 2010) documented acidic ($pH_{25°C}$ = 2.58–2.93) hot springs (42–99 °C) in Socorro Island, Mexico enriched in H_2 and CH_4 attributed to serpentinization. As it is located in an active magma-driven hydrothermal system, further work can decouple how much the compositions of these fluids were influenced by volcanic input or by serpentinization. Otherwise, temperatures higher than those recorded in Hakuba Happo for continental serpentinizing fluids have yet to be measured, but higher temperatures are observed in submarine hydrothermal fields. Calculated pH values at *in situ* temperatures (ranging from 75–116 °C) for end-member fluids venting at the Lost City hydrothermal field are lower than those predicted for Ctl-Brc-Di equilibria (Seyfried and others, 2015). For instance, at an *in situ* temperature of 90 °C (Beehive Structure, Lost City hydrothermal field; Seyfried and others, 2015), the calculated $pH_{90°C}$ of 8.9 is 1.5 pH units below that predicted for a fluid in equilibrium with Ctl-Brc-Di ($pH_{90°C}$ = 10.4). Seyfried and others (2015) attributed this lower pH to the chrysotile-tremolite-diopside (Ctl-Tr-Di) equilibria, which compared to the Ctl-Brc-Di equilibria, will yield lower $\alpha Ca^{+2}/(\alpha H^{+})^{2}$ (and hence lower pH) and higher $\alpha SiO_{2(aq)}$. The shift from the Ctl-Brc-Di to the Ctl-Tr-Di equilibria results from subsurface transport in which fluids react with the intermingling peridotite and the relatively more silica-rich gabbroic bodies beneath the Lost City hydrothermal field (Seyfried and others, 2015).

Compared to pH, total dissolved Ca, Si, Mg and DIC do not vary as much with temperature (fig. 4A). At most, the total Mg concentration is greater by an order of magnitude at 100°C compared with 0 °C, while changes in total Ca, Si, and DIC are less conspicuous. As shown in figure 4B, the most abundant species contributing to the total Ca in the fluid is Ca^{+2}, although with an increasing contribution from $Ca(OH)^{+}$ as temperature increases. Total Si is dominantly made up of the anion $HSiO_3^{-}$, which can form aqueous complexes with cations like Na^{+}, Ca^{+2} and Mg^{+2} (fig. 4C). The low concentration of Mg^{+2} means that the abundance of the Mg-silicate complex is predicted to be lower than the concentration range shown in figures 4C and 4D. Total dissolved Mg is mostly made up of $Mg(OH)^{+}$ at these alkaline conditions (fig. 4D). Most of the dissolved inorganic carbon exists as the neutral complex, $CaCO_{3(aq)}$, in these Ca-enriched fluids followed by CO_3^{-2} (fig. 4E).

Variations in Fluid Salinity

Results described above are for calculations with 1 millimolal NaCl solutions. In additional models we examined the effects of varying salinity from dilute (0.1 millimolal NaCl) to that equivalent to seawater (0.5 molal NaCl). Results of calculations for conditions at 25 °C and 1 bar depicted in figure 5, show that pH and the concentrations of most dissolved species (DIC, total dissolved Mg and Ca) in equilibrium with the Ctl-Brc-Di plus calcite assemblage change only slightly, increasing with fluid salinity. In contrast, total dissolved Si increases by more than an order of magnitude (fig. 5A). This change is attributed to a shift in the dominant aqueous species that comprises the total

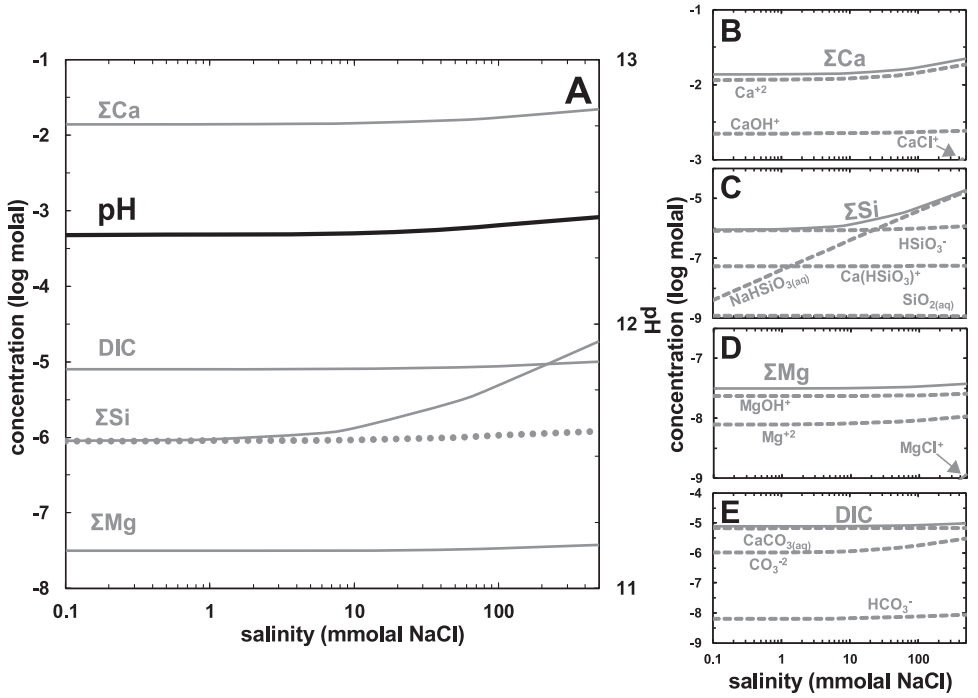

Fig. 5. (A) Trends of pH and total dissolved solute concentrations constrained by Ctl-Brc-Di equilibrium (rxn 18) at 25 °C and 1 bar, as functions of increasing fluid salinity. Also plotted are the calculated speciations of (B) ΣCa, (C) ΣSi, (D) ΣMg, and (E) DIC. Dotted line for ΣSi in (A) depicts results of simulations where the $NaHSiO_{3(aq)}$ complex is suppressed.

dissolved Si pool (fig. 5C). In dilute highly basic solutions, most of the dissolved Si exists as the anion $HSiO_3^-$, but shifts to the sodium silicate complex, $NaHSiO_{3(aq)}$ as salinity rises. Because the activity of $SiO_{2(aq)}$ remains constant as dictated by the Ctl-Brc equilibrium (rxn 11), and pH increases only slightly, the concentration of $HSiO_3^-$ also remains relatively constant (see rxn 12) with salinity. Simultaneously, the concentration of $NaHSiO_{3(aq)}$ increases even at constant $HSiO_3^-$ as the reaction

$$Na^+ + HSiO_3^- \rightarrow NaHSiO_{3(aq)} \quad (21)$$

proceeds with increasing salinity. The overall consequence is an increase in the total dissolved Si. This increase in dissolved Si aligns with observations of the enhanced solubility of a number of silicates with increasing salinity (see Newton and Manning, 2010) that may be attributed to changes in the speciation of dissolved silica species. However, existing stability constants for the $NaHSiO_{3(aq)}$ complex (Seward, 1974; Sverjensky and others, 1997) used in this work are questioned by some studies (Busey and Mesmer, 1977; Tutolo and Tosca, 2018; Huang and Sverjensky, 2019). For example, the solubilities of certain silicates (amorphous silica; Marshall and Warakomski, 1980; Zarubin and Nemkina, 1990) decrease with increasing salinity indicating a much weaker drive to form this complex than depicted in our models. Suppressing this complex results in a dissolved Si trend, shown by the dotted line in figure 5A, that is independent of fluid salinity. Future studies that can constrain solubilities of serpentinization-relevant minerals at highly saline environments will permit predictions of fluid compositions in other rocky bodies in our solar system where saline fluids are

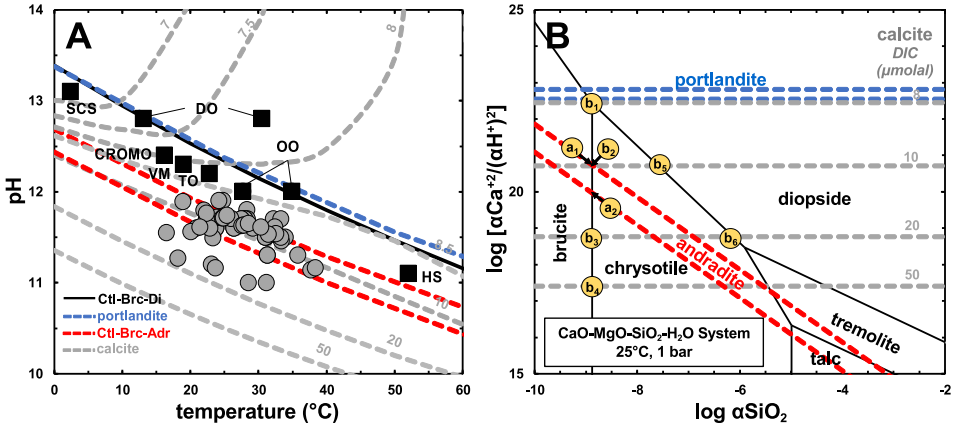

Fig. 6. (A) pH and temperature of hyperalkaline fluids (pH >11) sampled from Oman (filled gray circles, data from Paukert and others, 2012, Chavagnac and others, 2013b, and Canovas and others, 2017) and other <60 °C sites listed in fig. 4A (filled black squares). Most samples from Oman plot below the pH dictated by Ctl-Brc-Di equilibrium (solid black curve). (B) Activity diagram for the CaO-MgO-SiO_2-H_2O system. Stability fields and saturation lines of minerals are similar to fig. 3D, with the addition of saturation lines for calcite (dashed gray) at variable DIC concentrations indicated above or below the line, portlandite (dashed blue), and andradite (dashed red). Upper and lower lines for portlandite represent ranges in solubility data from the literature (see text). Upper line for andradite depicts redox conditions constrained by the iron-magnetite equilibrium, lower line is constrained by the goethite-magnetite equilibrium. Points a_1 and a_2 depict equilibrium with andradite with both chrysotile and brucite (Ctl-Brc-Adr) at redox conditions mentioned above. Point b_1 depicts the Ctl-Brc-Di equilibrium triple point. Points b_2, b_3, and b_4 depict equilibrium with Ctl-Brc-Cal at DIC concentrations of 10, 20, and 50 μmolal, respectively. The lines in (A) represent pH values calculated by the equilibria noted by these points in (B) – dashed red lines (a_1 and a_2) and dashed gray lines (b_1, b_2, b_3, and b_4) – as well as pH values derived from the lower portlandite line (dashed blue line) and additional Ctl-Brc-Cal equilibrium points at limited DIC (<8.5 μmolal) concentrations (dashed gray lines). Equilibria without brucite are represented by points b_5 and b_6, which depict equilibrium with Ctl-Di-Cal at DIC concentrations of 10 and 20 μmolal, respectively. See table 3 for abbreviations of minerals.

known to predominate (Glein and others, 2015). Nonetheless, the lowest Si concentrations measured from non-saline, continental serpentinizing fluids (1 μmolal Si, Chavagnac and others, 2013b) are consistent with our predictions. The speciation of other solutes are depicted in figures 5B, 5D, and 5E for total dissolved Ca, Mg and inorganic carbon, respectively, and change minimally with variable salinity. Chloride complexes of Ca^{+2} and Mg^{+2} occur only in minor amounts that remain below most of the concentration range in figure 5 (note how $MgCl^+$ appears only at the highest salinity) and would not affect the speciation of these cations as much as Na affects the total dissolved Si.

Precipitation of Ca-bearing Phases

The dissolution of diopside and the lack of a precipitating Ca-bearing phase to counter reaction (4) requires the consumption of H^+ (or production of OH^-) to accommodate the otherwise unbalanced Ca^{+2}. During the overall serpentinization progress, this increase in pH is accommodated until the fluid attains equilibrium with diopside. As shown in figure 4A, equilibria involving diopside can account for some of the highest pH values observed in serpentinizing environments. Most studies on continental serpentinizing sites report the pH of hyperalkaline fluids to be between 11 to 12, somewhat lower than the theoretical maxima. As an example, as shown in figure 6A, most hyperalkaline fluids sampled in Oman (filled gray circles, Paukert and others, 2012; Chavagnac and others, 2013b; Canovas and others, 2017) have measured pH values lower than those set by equilibrium with diopside (solid black line in fig. 6A)

given the measured fluid temperature. The precipitation of Ca-bearing phases can cause fluids to shift from being in equilibrium with diopside and can likely draw pH to lower values. In this section, we explore the effects of various Ca-bearing phases (portlandite, andradite, and calcite) on fluid compositions. Results of calculations are shown in the temperature *vs.* pH plot and the CaO-MgO-SiO_2-H_2O activity diagram depicted in figures 6A and 6B, respectively.

Portlandite.—Albeit rarely, portlandite can occur in serpentinizing environments (Neal and Stanger, 1984; Chavagnac and others, 2013a). The $\alpha Ca^{+2}/(\alpha H^{+})^2$ needed to saturate portlandite can be derived using the equilibrium constant expression for the reaction

$$Ca^{+2} + 2H_2O \rightarrow Ca(OH)_{2(portlandite)} + 2H^{+}. \quad (22)$$

At ambient conditions (25°C, 1 bar), $\alpha Ca^{+2}/(\alpha H^{+})^2 = 10^{22.5}$ to $10^{22.8}$ (Reardon, 1990; Wolery and Jove-Colon, 2004; Blanc and others, 2010, dashed blue lines in fig. 6B) where the lower value is close to that derived for Ctl-Brc-Di equilibrium ($10^{22.4}$, see point b_1 in fig. 6B). Temperature-dependent thermodynamic data for portlandite exist (Wolery and Jove-Colon, 2004) and allow us to calculate pH constrained by portlandite solubility from 0 °C to 60 °C. The dashed blue line plotted in figure 6A depicts calculated pH values that closely align with pH values dictated by the Ctl-Brc-Di equilibrium. It follows that fluids produced through serpentinization, at the maximum pH and Ca concentration attainable through Ctl-Brc-Di- equilibrium, can potentially precipitate portlandite. However, it is only at this specific stage of the overall serpentinization progress that portlandite saturation can be attained, which is consistent with its rare occurrence in hyperalkaline pools and serpentinite outcrops.

Andradite.—Anhydrous and hydrous andraditic garnets are known to occur in a number of serpentinites (Beard and Hopkinson, 2000; Menez and others, 2012, 2018; Plümper and others, 2014), where they are found to be intimately associated with organic matter (Menez and others, 2012, 2018). The uptake of Ca^{+2} into garnet as shown by the reaction

$$3Ca^{+2} + 2Fe^{+3} + 3SiO_{2(aq)} + 6H_2O \rightarrow Ca_3Fe_2Si_3O_{12(andradite)} + 12H^{+} \quad (23)$$

can draw pH away from equilibrium with diopside. The $\alpha Ca^{+2}/(\alpha H^{+})^2$ of fluids in equilibrium with andradite was calculated using reaction (23) over ranges of $\alpha SiO_{2(aq)}$ from 10^{-10} to 10^{-2}, and $\alpha Fe^{+3}/(\alpha H^{+})^3$ constrained by redox states buffered by either goethite-magnetite or magnetite-iron equilibria. Results of calculations are plotted as dashed red lines in figure 6B and show that equilibrium with andradite requires that the fluid has lower values of $\alpha Ca^{+2}/(\alpha H^{+})^2$ than set by equilibrium with diopside. A more reduced environment constrained by the magnetite-iron equilibrium (top dashed red line in fig. 6B) results in slightly higher $\alpha Ca^{+2}/(\alpha H^{+})^2$ values than those set by the goethite-magnetite (lower dashed red line in fig. 6B). We calculated pH constrained by an equilibrium assemblage of chrysotile, brucite, and andradite (Ctl-Brc-Adr, points a_1 and a_2 in figure 6B) at temperatures ranging from 0 °C to 60 °C and results of calculations are overlain in figure 6A as dashed red lines. pH constrained by the above equilibrium at the range of temperature depicted in figure 6A can account for many but not all environmental observations offset from Ctl-Brc-Di equilibria. In the calculation above, we substituted thermodynamic data for andradite in place of missing data for hydrous andraditic garnets. Further calculations incorporating thermodynamic data on hydrous andraditic garnets, and field studies documenting their occurrence in ophiolitic aquifers, would allow assessments on the role of garnets during low-temperature serpentinization. Like magnetite, andraditic garnets can potentially host ferric iron among secondary precipitates during serpentinization, which can further the potential to generate H_2 via reaction (13). For example,

Plümper and others (2014) estimated massive amounts of H_2 generated through andradite formation that would be enough to stabilize Fe-Ni alloys based on observations of garnet-bearing serpentinites in the Feragen ultramafic body in Norway.

Calcite.—As discussed above, results shown in figure 3A demonstrate that limits on the amount of DIC late in the overall serpentinization progress mean that calcite precipitation (rxn 15) will not be able to balance Ca^{+2} released through diopside dissolution (rxn 4). However, if there is a supply of DIC from another source it may be possible for fluids to be in equilibrium with calcite instead of diopside. This may occur where deep-seated fluids devoid of atmospheric input discharge back to the surface where infiltration of $CO_{2(g)}$, interaction with near-surface carbonate veins, or mixing with DIC-rich shallow groundwater can supply DIC. The consequences are illustrated by the dashed gray lines in figure 6B, which show calculated values of $\alpha Ca^{+2}/(\alpha H^{+})^2$ in equilibrium with calcite at the indicated concentrations of DIC. At DIC concentration of ~8 μmolal, a 25 °C, 1 bar fluid can be in equilibrium with both diopside and calcite (point b_1 in fig. 6B). At higher DIC concentrations, the presence of calcite can draw $\alpha Ca^{+2}/(\alpha H^{+})^2$ to values lower than those constrained by diopside. If calcite precipitation is faster than diopside dissolution, fluid composition can shift from that dictated by Ctl-Brc-Di equilibrium to that constrained by chrysotile-brucite-calcite (Ctl-Brc-Cal) equilibrium such as those depicted by points b_2, b_3, and b_4 in figure 6B for DIC concentrations of 10, 20, and 50 μmolal, respectively. The consequences for pH of this shift in controlling mineral assemblages at temperatures ranging from 0 °C to 60 °C are shown as dashed gray lines in figure 6A, and show that equilibrium with calcite in extremely DIC limited environments (< 8 μmolal) may require pH higher that can be attained through equilibrium with diopside. This could account for the extremely high pH recorded by Etiope and others (2017) at one site in the Dinaride Ophiolite discussed above. Otherwise, at DIC concentrations > 8 μmolal, calcite will draw pH to lower values than equilibrium with diopside. With increasing DIC concentration the equilibrium pH constrained by Ctl-Brc-Cal will be lower. As shown in figure 6A, a shift from equilibrium with diopside to calcite can account for most environmental pH observations. As an example, most hyperalkaline fluids sampled in Oman have pH values that lie between ranges possible for calcite at low DIC concentrations (8–20 μmolal) and andradite at variable redox conditions (goethite-magnetite to magnetite-iron equilibria). So far, no study has surveyed the abundance of andradite or hydrogarnets in ophiolitic aquifers. Calcite, on the other hand, is common as near-surface veins and surface travertine deposits (Kelemen and Matter, 2008; Mervine and others, 2014). It is likely that this shift to calcite equilibria occurs in the near subsurface or at the surface where deep-seated fluids encounter DIC-rich shallow groundwater or the atmosphere. It can also be seen in figure 6A that a few Oman samples plot at pH values higher than that set by calcite equilibrium at 10 μmolal DIC and are close to equilibrium with diopside or with calcite at extremely DIC-limited conditions (<10 μmolal). This suggests that these fluids were less influenced by surficial or shallow subsurficial processes and remain close to equilibrium with the altered host rocks (Ctl-Brc-Di equilibrium).

Higher concentration of DIC will draw the fluid to lower pH as shown in figure 6A. Pfeiffer (1977) and Bruni and others (2002) argued that the high pH of serpentinizing springs is mainly attributed to extremely low DIC characteristic of systems closed to atmospheric influence. Our calculations agree with this statement, as very low DIC concentrations are needed for pH to remain > 11 as shown by the calcite trends in figure 6A. However, reaction path calculations underscore that the path to hyperalkaline pH is facilitated by primary mineral dissolution reactions, especially diopside, and a low DIC concentration is only needed to preserve hyperalkaline conditions generated by water-rock reactions. Nevertheless, the calculations shown above underline

that variabilities in pH recorded in serpentinizing systems may be attributed to variations in DIC input in addition to variations in temperature and buffering reactions involving other minerals.

In the discussions above, brucite is assumed to be present in the equilibrium mineral assemblage. Fluid pathways may encounter environments where brucite is unstable such as in the shallow subsurface where the aquifer can be composed of brucite-free serpentinites (Miller and others, 2016). Interaction with these rocks will draw fluids away from the brucite stability field depicted in figure 6B and toward assemblages stable at higher $\alpha SiO_{2(aq)}$. As an example, fluids in equilibrium with chrysotile, diopside, and calcite at DIC concentrations of 10 μmolal and 20 μmolal, respectively depicted by points b_5 and b_6 in figure 6B, will result in fluids with lower $\alpha Ca^{+2}/(\alpha H^{+})^2$ and higher $\alpha SiO_{2(aq)}$ and will ultimately generate fluids with lower pH and higher Si concentrations than values constrained by the Ctl-Brc-Di equilibrium. Note that points b_5 and b_6 (Ctl-Di-Cal), respectively, share similar $\alpha Ca^{+2}/(\alpha H^{+})^2$ with points b_2 and b_3 (Ctl-Brc-Cal equilibrium) and would result in fluids with similar pH with the former distinguished from the latter only by their higher dissolved Si concentrations. As such, most of the environmental pH values shown in figure 6A can also be accommodated by this shift to the Ctl-Di-Cal equilibrium. In addition to the consequences of a brucite-free serpentinite aquifer, mixing with Si-rich shallow groundwater can also draw fluids to higher $\alpha SiO_{2(aq)}$. Assessment of the silica concentrations of serpentinization-generated hyperalkaline fluids is one of the most powerful ways to discriminate among various fluid pathways possible in ultramafic aquifers, as well as the consequence of fluid mixing at and below the surface.

Variations in Contributions from Primary Minerals

The preceding discussion refers to a model of rainwater reacting with a single generalized composition of ultramafic rock (85% Fo_{90}-olivine, 14% En_{90}-orthopyroxene, and 1% Di_{95}-clinopyroxene). This composition is characteristic of harzburgites that are common in ophiolites. However, modal compositions of primary minerals that compose harzburgites vary in ophiolites and in exhumed ultramafic rocks in the seafloor [see: Warren (2016) for a compilation of seafloor ultramafic rock mineralogy and geochemistry]. Consequently, fluids will likely encounter rocks with variable composition during subsurface transport. Moreover, primary minerals can dissolve at differing rates resulting in variable contributions of aqueous solutes from primary minerals that may differ from the modal composition of the host rock. Therefore, in this section we discuss the consequence of variable contributions of primary minerals on the compositions of aqueous fluids. Details on the composition of the reacting rocks used in our simulations can be found in table 2. This work focuses on alteration at ambient conditions and is complementary to results by Klein and others (2013) on the variabilities in secondary mineralization and fluid and gas chemistry resulting from the alteration of ultramafic rocks of variable modal compositions at temperatures up to 400 °C. In addition, this work expands the compositional variabilities explored by seminal calculations on low-temperature serpentinization by Pfeifer (1977) and Palandri and Reed (2004).

Results for 25 °C and 1 bar are shown in figures 7 to 9. We start with rainwater interactions with rocks composed only of olivine ($Forsterite_{90}$) and orthopyroxene ($Enstatite_{90}$) (Models B1-B5, $MgO\text{-}FeO\text{-}SiO_2\text{-}H_2O$ system), and then discuss the effects of involving clinopyroxene ($Diopside_{95}$) (Models C1-C5, $CaO\text{-}MgO\text{-}FeO\text{-}SiO_2\text{-}H_2O$ system) on the resulting fluid compositions. Lastly, instead of a fresh ultramafic rock, we model fluids reacting with a serpentinite (Models D1-D4). This model shares features with those conducted by Cipolli and others (2004) and Bruni and others (2002) who simulated rainwater-serpentinite interactions to account for the origins of hyperalkaline fluids seeping out from metaophiolitic lithologies in the Voltri Group of

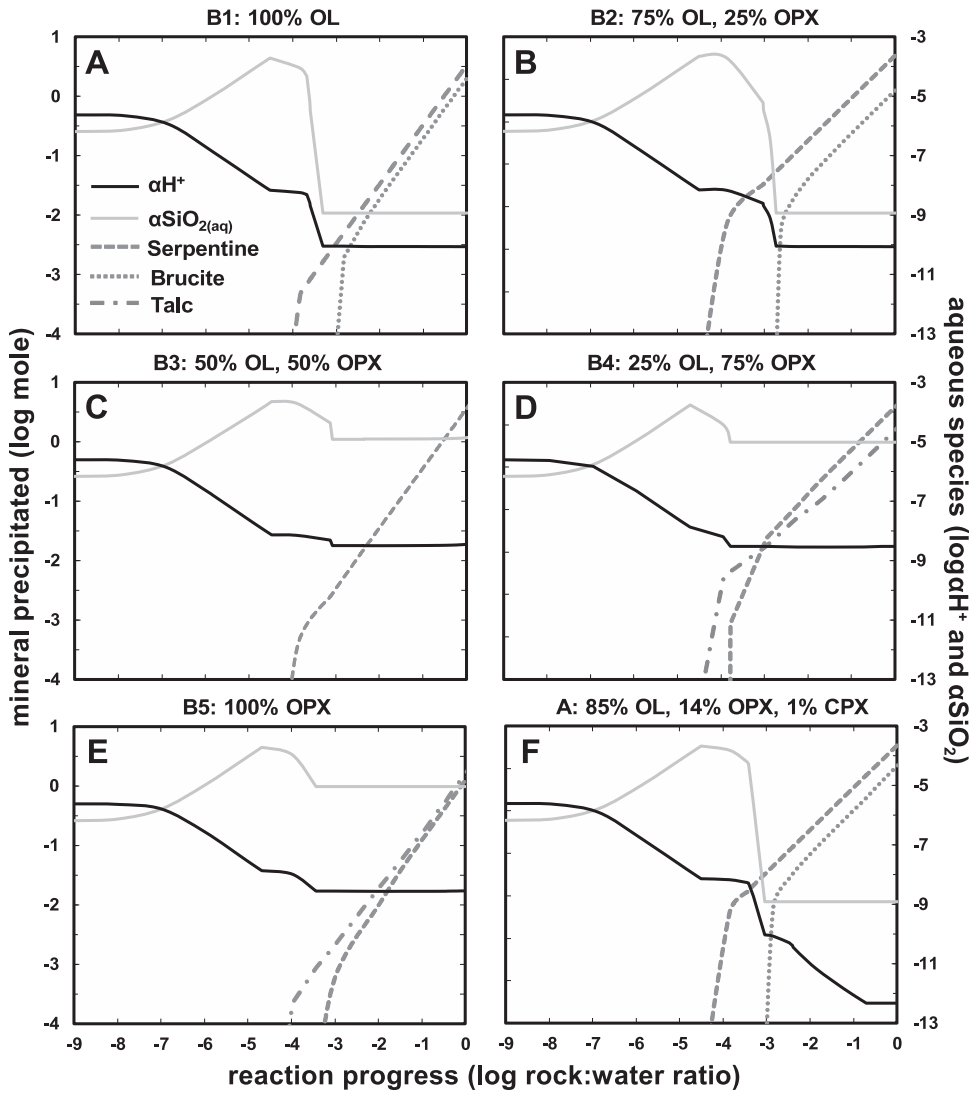

Fig. 7. (A-E) Results of simulations at 25 °C and 1 bar for host rocks of the MgO-FeO-SiO_2-H_2O system (Models B1-B5) where reacting rocks contain olivine (OL) or orthopyroxene (OPX) or combinations of both. (F) Results of simulation illustrated in fig. 3 (Model A) for comparison. Contributions from the primary phases are indicated above each plot.

the Ligurian Ophiolite in Italy. However, instead of bulk serpentinite chemistry, here we use variable molal contributions of serpentine and brucite to investigate the effects of variable serpentinite compositions on the evolution of fluids. In these serpentinite models, the source of Ca is minor relict clinopyroxene.

Olivine and orthopyroxene alteration (MgO-FeO-SiO_2-H_2O system).—As shown in figure 7A, at late stages of reaction progress almost equal amounts of chrysotile and brucite (in moles) will precipitate if the only dissolving mineral is olivine (Model B1). This is exemplified by reaction (16), which depicts the sum of the reactions involving the dissolution of forsterite (rxn 2), and the precipitation of chrysotile (rxn 6) and brucite

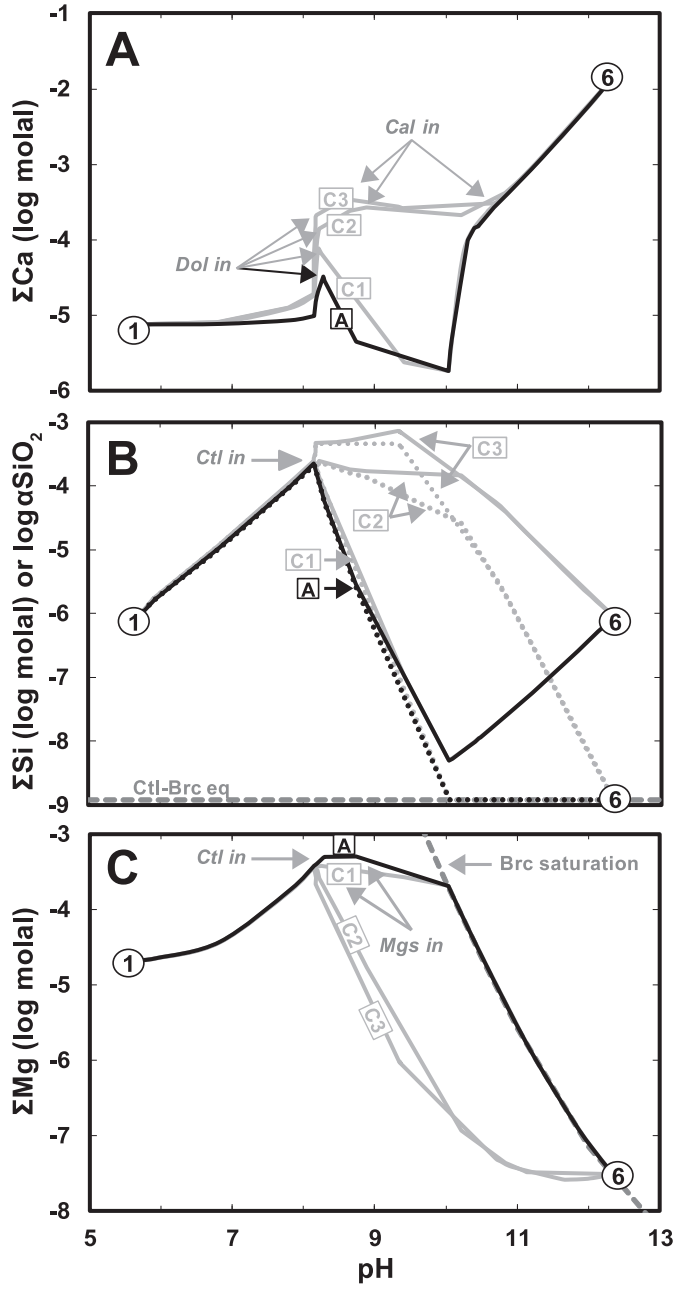

Fig. 8. Trends in (A) ΣCa, (B) ΣSi and $\alpha SiO_{2(aq)}$, and (C) ΣMg during reactions with variable harzburgitic compositions in the CaO-MgO-FeO-SiO_2-H_2O system at 25 °C and 1 bar. Black and gray lines refer to results of simulations using Model A and C rock compositions, respectively. Note that 1 and 6 refer to the beginning and end of the reaction path depicted in figs. 2 and 3. Letters indicate reaction paths summarized in table 2. Abbreviations of minerals are listed in table 3. The word "in" (for example, Mgs in) refers to the point in the reaction progress where a given mineral starts to precipitate. Note that $SiO_{2(aq)}$ in (B) is one of the various species that compose ΣSi shown in fig. 4C.

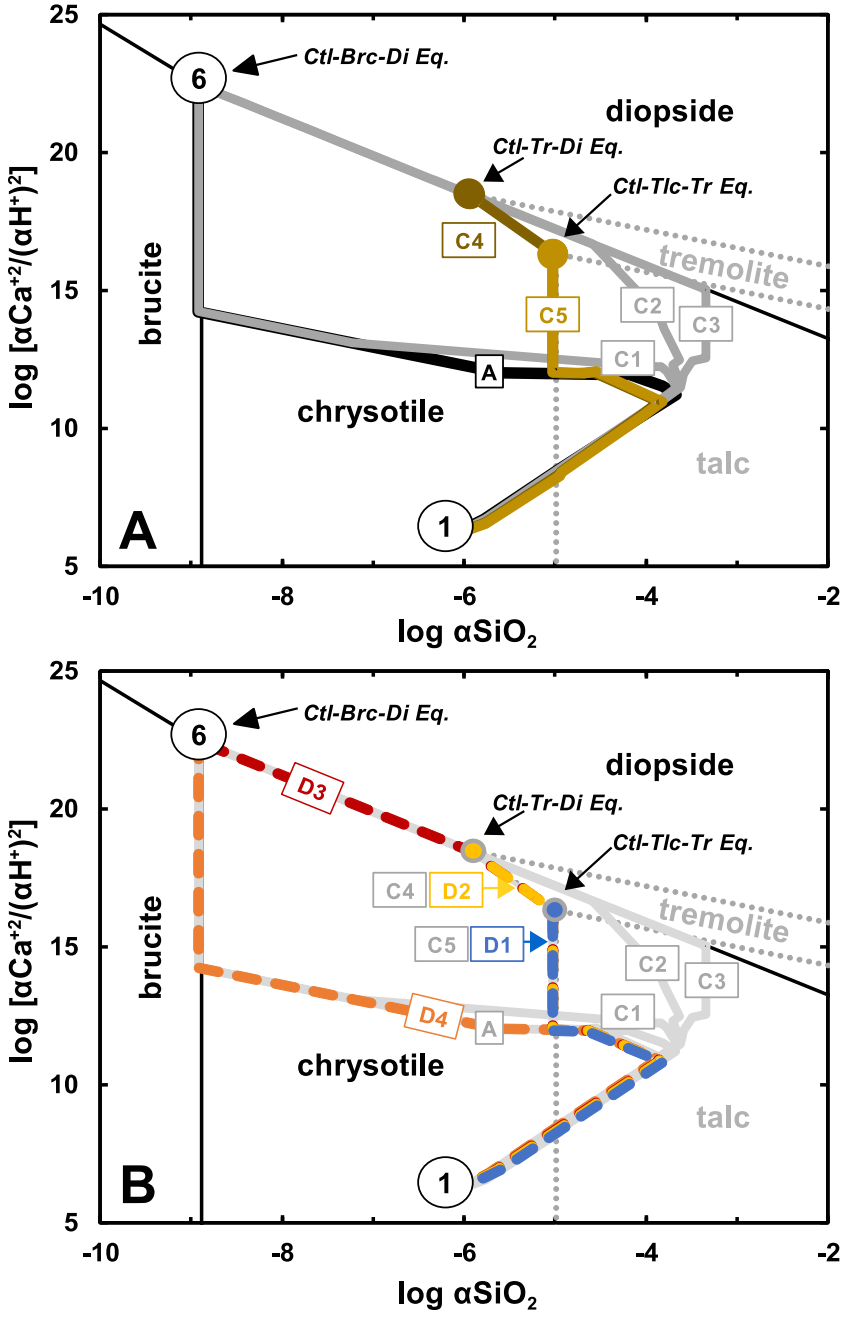

Fig. 9. CaO-MgO-SiO_2-H_2O activity diagram for 25 °C and 1 bar depicting various reaction pathways summarized in table 2: (A) models A and C1-C5, (B) models D1-D4. Reaction paths A and C1-C5 depict interaction of water with fresh ultramafic rocks with variable primary mineral compositions, while reaction paths D1-D4 depict water interacting with serpentinites of variable compositions (see table 2). Stability fields bounded by dotted lines in gray are for minerals (talc and tremolite) suppressed in some calculations. Note that reaction paths D1-D4 overlap with most of reaction paths A and C1-C5, and that 1 and 6 refer to the beginning and end of the reaction path depicted in figs. 2 and 3.

(rxn 10). The reason that there is slightly less brucite forming relative to chrysotile in figure 7A is that iron released from olivine precipitates as goethite and magnetite during alteration. If the reacting mineral is pure forsterite, equal amounts of chrysotile and brucite (in moles) will precipitate as depicted by reaction (16). Note that reaction (16) results in neither a net consumption or production of H^+ and pH will remain constant once chrysotile and brucite are both precipitating. The activity of $SiO_{2(aq)}$ will be set by Ctl-Brc equilibrium defined by reaction (11). The consequences of reactions (11) and (16) are shown in figure 7A, including the constant pH (-log αH^+) and $\alpha SiO_{2(aq)}$ trends once brucite joins chrysotile in the secondary assemblage. The predicted pH arising from these equilibria is near 10 which is close to the maximum pH of 9.5 measured by Okland and others (2012) in groundwaters seeping from olivine-rich (dunite) outcrops of the Leka Ophiolite.

In contrast to dunites which are mostly composed of olivine, harzburgites have considerable abundances of orthopyroxene in addition to olivine. The involvement of orthopyroxene during alteration will decrease the amount of brucite precipitated in favor of chrysotile as shown in figure 7B, which illustrates a model where rainwater interacts with a hypothetical rock composed of 75 mole percent olivine and 25 mole percent orthopyroxene (see rxn 17, Model B2). As in figure 7A, both chrysotile and brucite are present, which means that fluid compositions will be controlled by the same Ctl-Brc equilibrium (rxn 11). As a consequence, this scenario will yield similar pH and total dissolved Si values to the results shown in figure 7A for olivine-only dissolution. This pattern continues until we consider equal mole percent contributions of olivine and orthopyroxene (Model B3), as depicted in figure 7C, which will only produce serpentine via

$$Mg_2SiO_{4(forsterite)} + MgSiO_{3(enstatite)} + 2H_2O \rightarrow Mg_3Si_2O_5(OH)_{4(chrysotile)}. \quad (24)$$

In cases where the abundance of orthopyroxene exceeds that of olivine, talc is favored instead of brucite, as shown in figure 7D (Model B4). In these models for orthopyroxene-rich systems, the precipitation of talc is allowed. As the abundance of primary orthopyroxene increases, talc will precipitate at the expense of chrysotile. This pattern continues for alteration of rocks composed of increasing abundances of orthopyroxene, and culminates in the results shown in figure 7E for orthopyroxene-only dissolution (Model B5), which results in equal moles of precipitating chrysotile and talc, corresponding to the reaction

$$6MgSiO_{3(enstatite)} + 3H_2O \rightarrow Mg_3Si_2O_5(OH)_{4(chrysotile)} + Mg_3Si_4O_{10}(OH)_{2(talc)}. \quad (25)$$

Note that most of the plots in figure 7 reveal that extensive reaction progress results in constant pH values as H^+ is neither consumed and produced, consistent with reactions (16), (17), (24) and (25) depending on the rock composition. In the model depicted in figure 7C, pH approaches 8.5 once chrysotile starts to precipitate. In the orthopyroxene-dominated models shown in figures 7D and 7E, constant pH is maintained once talc and chrysotile are both precipitating. At these conditions, the $\alpha SiO_{2(aq)}$ will be set by the chrysotile-talc (Ctl-Tlc) equilibria as defined by

$$Mg_3Si_2O_5(OH)_{4(chrysotile)} + 2SiO_{2(aq)} \rightarrow Mg_3Si_4O_{10}(OH)_{2(talc)} + H_2O, \quad (26)$$

and is higher than values set by Clt-Brc equilibrium (rxn 11), which is revealed by comparing figures 7D and 7E with figures 7A and 7B.

Alteration in the presence of clinopyroxene (CaO-MgO-FeO-SiO_2-H_2O system).—As shown in figures 7A to 7E, hyperalkaline pH (>11) can not be attained from the dissolution of any combination of olivine and orthopyroxene alone. It is the presence of diopside that drives pH to increase further with reaction progress. The precipitation of

dolomite (rxn 8) calcite (rxn 15) will not be enough to counterbalance the pH increase driven by the overall reaction among diopside, chrysotile and brucite (rxn 18) owing to DIC limitation at late stages of reaction progress. Thus, pH will continue to increase and the fluid will accumulate Ca until it maximizes as the fluid attains equilibrium with diopside. Results from the initial model described above (85% olivine, 14% orthopyroxene, 1% clinopyroxene) are shown again in figure 7F for comparison with the other scenarios that do not involve the dissolution of diopside. It can be seen that including diopside in the model will yield pH values >12, which are higher than those attained in scenarios without it (pH ≤ 10).

The dramatic effect on pH of the single example of a diopside-bearing alteration model in figure 7 raises questions about the consequences for other ultramafic assemblages. Results of simulations depicting effects of modal variations in the CaO-MgO-FeO-SiO_2-H_2O system, summarized in table 2, are shown in figures 8 and 9. In both figures, reaction path A (Model A) reflects results discussed above as depicted in figures 3 and 7F for 85% Ol-14% Opx-1% Cpx. Simulations that generally encompass variabilities in harzburgite compositions, having five times as much clinopyroxene and variable contributions from olivine and orthopyroxene, are depicted by reaction paths C1, C2, and C3, which refer to 85% Ol-10% Opx-5% Cpx, 75% Ol-20% Opx-5% Cpx, and 65% Ol-30% Opx-5% Cpx scenarios, respectively. As shown in figure 8A trends in total dissolved Ca are similar among the four models tested. Note however that models with 5 percent clinopyroxene can attain higher Ca concentrations in fluids at pH~9 and can precipitate calcite at lower extents of reaction progress than the model with 1 percent clinopyroxene (reaction path A).

Trends in total dissolved Si concentration (solid lines), as well as trends in the $SiO_{2(aq)}$ activity (dotted lines) are shown in figure 8B. Reaction paths A and C1 follow similar patterns, characterized by dramatic decreases in the total Si concentration and $SiO_{2(aq)}$ activity once chrysotile joins the secondary assemblage (see Stage 2 of the overall reaction progress). Likewise, these reaction paths also attain $\alpha SiO_{2(aq)}$ values constrained by Ctl-Brc equilibria starting at pH~10, yet have increasing total Si concentrations until the maximum pH values are attained. In contrast, the models with greater contribution from orthopyroxene (Reaction paths C2 and C3) yield different pathways with no abrupt drop in total Si concentration once chrysotile starts precipitating. The reaction of enstatite into chrysotile involves a release in $SiO_{2(aq)}$ as depicted by the reaction

$$3MgSiO_{3(enstatite)} + 2H_2O \rightarrow Mg_3Si_2O_5(OH)_{4(chrysotile)} + SiO_{2(aq)}, \qquad (27)$$

which is in contrast to alteration of relatively more forsterite-rich systems (reaction paths A and C1) that involve release of Mg^{+2} during chrysotile precipitation (see rxn 7). $SiO_{2(aq)}$ released through reaction (27) can react with forsterite to form additional chrysotile via

$$3Mg_2SiO_{4(forsterite)} + SiO_{2(aq)} + 4H_2O \rightarrow 2Mg_3Si_2O_5(OH)_{4(chrysotile)}. \qquad (28)$$

Consequently, as forsterite is reacting with excess silica from orthopyroxene to form chrysotile, the precipitation of brucite occurs much further in reaction progress in the orthopyroxene-rich model. These differences are depicted in figure 8C, which illustrates trends in the total dissolved Mg concentration of the four reaction paths. Also depicted in figure 8C is the saturation curve for brucite (dashed gray line), showing that brucite precipitates when the reaction paths intersect the saturation line. Reaction paths C2 and C3 attain brucite saturation much further along the alteration process than do the other reaction paths. Moreover, and in contrast to reaction paths A and C1, magnesite precipitation does not occur along Reaction paths C2 and C3, due to interactions with rocks that are relatively less Mg-rich and more Si-rich.

These various pathways are depicted on an activity diagram for the CaO-MgO-SiO_2-H_2O system in figure 9A. Note that reaction paths C2 and C3 first attain equilibrium with both chrysotile and diopside and only attain brucite saturation at the end of the reaction path at the Ctl-Brc-Di equilibrium point. This is in contrast with models depicting interactions with more Mg-rich or forsterite-rich rocks where chrysotile and brucite equilibrium is attained first before reaching the Ctl-Brc-Di equilibrium point, as shown by reaction paths A and C1. In addition to the four reaction paths shown in figure 8, results of additional calculations modelling orthopyroxene-dominated systems, 45% Ol-50% Opx-5% Cpx (reaction path C4) and 35% Ol-60% Opx-5% Cpx (reaction path C5), are also shown in figure 9A. When contributions from orthopyroxene exceed those of olivine, reaction paths will not attain silica activities lower than that constrained by equilibrium with tremolite. Reaction path C4, which models system with still significant contribution from olivine but not greater than pyroxene minerals, will ultimately end at the chrysotile-tremolite-diopside (Ctl-Tr-Di) invariant point shown in figure 9A. Reaction path C5 exemplifies systems with even greater orthopyroxene contributions and will end at the chrysotile-talc-tremolite (Ctl-Tlc-Tr) equilibrium triple point without proceeding to compositions with lower $\alpha SiO_{2(aq)}$. Equilibria with Ctl-Tr-Di or Ctl-Tlc-Tr results in lower $\alpha Ca^{+2}/(\alpha H^{+})^2$ and higher $\alpha SiO_{2(aq)}$ than those in equilibrium with Ctl-Brc-Di. As a consequence, water-rock interactions hosted in orthopyroxene-dominated lithologies will result in fluids with lower pH and dissolved Ca values but higher Si concentration. Further discussion of the consequences for fluid compositions arising from variabilities in primary minerals follows discussion of model results below that allow iron incorporation into solid solutions of precipitating phases.

Alteration of serpentinites.—In addition to alteration of fresh ultramafic rocks, groundwater can interact with partially or completely serpentinized rocks. Results of four reaction paths that model alteration of serpentinites (composed mostly of serpentine and brucite) are shown in figure 9B where they can be compared to the alteration of fresh ultramafic rocks discussed above (see table 2). In these calculations, the source for Ca is relict clinopyroxene (5 mole % Di_{95}). Reaction path D1 (dashed blue line) shows the changing calculated composition of a fluid interacting with a rock whose secondary assemblage is completely composed of serpentine and relict clinopyroxene, and reaction paths D2 (dashed yellow), D3 (dashed red) and D4 (dashed orange) follow fluid compositions where the aquifer rock is composed of different proportions of serpentine and brucite with 5 percent clinopyroxene (see table 2). Overall, these reaction paths are similar to others shown in figures 8 to 9A, but contributions from the dissolving rock are described by the reverse of reactions (6) and (10) for chrysotile and brucite dissolution, respectively. Alteration of a serpentinite without relict clinopyroxene leads to results similar to those shown in figure 7C for reaction of 50 mole percent olivine and orthopyroxene. After all, a mole of serpentine (chrysotile) is the hydrated equivalent of one mole each of olivine (forsterite) and orthopyroxene (enstatite) as indicated by reaction (24).

Reaction path D1 generates a fluid with $\alpha SiO_{2(aq)}$ controlled by Ctl-Tlc equilibrium as a fully serpentinized ultramafic rock is too silica-rich to attain the Ctl-Brc equilibria. Additionally, as depicted by the CaO-MgO-SiO_2-H_2O activity diagram shown in figure 9B, path D1 ends up at the Ctl-Tlc-Tr equilibrium triple point similar to that of reaction path C5 described above. Compared with the Ctl-Brc-Di and the Ctl-Tr-Di equilibrium triple points, fluids constrained by Ctl-Tlc-Tr equilibrium have lower $\alpha Ca^{+2}/(\alpha H^{+})^2$ and higher $\alpha SiO_{2(aq)}$. The pH of the fluid controlled by these equilibria can be derived and results of calculations yield pH (~10 at 25 °C, 1 bar) lower than that attained by a fluid controlled by the Ctl-Brc-Di (pH ~ 12) or the Ctl-Tr-Di (pH ~ 11) equilibria. If the host serpentinite contains some amount of brucite, fluids can attain equilibrium with the Ctl-Tr-Di or the Ctl-Brc-Di assemblage.

Models depicting serpentinites composed of 75 mol% serpentine, 20 mol% brucite, and 5 mol% clinopyroxene, represented by reaction path D2 in figure 9B, ultimately result in fluids in equilibrium with Ctl-Tr-Di similar to systems modelled by reaction path C4. A greater contribution from brucite will result in reaction paths that end up at the Ctl-Brc-Di equilibrium triple point. This is shown by reaction path D3 in figure 9B, which depicts results for a model fluid reacting with host rocks composed of 65 mol% serpentine, 30 mol% brucite, and 5 mol% clinopyroxene. This model follows a path that is similar to that of reaction paths C2 and C3 described above, and would even follow a similar path at earlier stages of the reaction progress if talc precipitation was suppressed. The trace of reaction path D4 in figure 9B depicts interactions with rocks containing even more brucite (40 mol%) and follows a path similar to those from alteration of olivine-rich rocks (reaction paths A and C1). Specifically, if talc is suppressed in a model related to that depicted by reaction path D4, the results will follow a path close to that shown by reaction path C1.

Further discussion on the consequences of lithological variations.—Many reaction paths for low-temperature alteration of olivine-rich rocks are similar to the overall serpentinization of a rock with the generalized composition shown in figures 2 and 3 and summarized as reaction path A in figures 7, 8, and 9. Examination of these figures shows that this pathway closely resembles those resulting from simulations of other olivine-rich rocks (reaction path C1) and consequently, despite these lithological variations, a useful starting assumption is that low-temperature alteration of olivine-rich rocks would follow similar stages in the overall reaction progress as that of reaction path A. It is only in models that include greater contributions from orthopyroxene (for example, reaction paths C2 and C3 starting with 25 mol% orthopyroxene) that the overall reaction progress takes a different pathway. Nevertheless, these models still attain equilibrium with chrysotile, brucite, and diopside (Stage 6) but along a different path than that followed by more olivine-rich systems. Specifically, this pathway attains equilibrium with brucite only at the last stage of the overall reaction progress. Results of further simulations involving greater orthopyroxene contributions (>50 mol%) yield pathways resulting in fluids in equilibrium with Ctl-Tr-Di or Ctl-Tlc-Tr.

The system CaO-MgO-SiO_2-H_2O, as represented by the activity diagrams shown in figures 6B and 9, has three equilibrium triple points: (1) Ctl-Brc-Di, (2) Ctl-Tr-Di, and (3) Ctl-Tlc-Tr. It follows that fluid-rock interactions involving ultramafic rocks will ultimately lead to fluids with three distinct composition as dictated by these assemblages, despite variabilities in the compositions of the reacting rocks. Variabilities in the dissolved inorganic carbon levels, however, draw fluids away from these equilibrium triple points to equilibrate with calcite and greatly diversify the compositions of fluids approaching equilibrium with the host aquifer rocks. As shown in figure 6B, greater amounts of DIC, however, would be needed to draw fluids away from being in equilibrium with Ctl-Tr-Di or Ctl-Tlc-Tr than that if the fluid composition is dictated by the Ctl-Brc-Di equilibrium.

Results of calculations involving secondary minerals (serpentine and brucite, with relict clinopyroxene) as the dissolving phases, will yield a range of fluid compositions similar to those generated when primary minerals are dissolving, as depicted in the CaO-MgO-SiO_2-H_2O activity diagram shown in figure 9B. *It follows that it would be difficult to distinguish fluids reacting with either fresh or altered ultramafic rocks based solely on their pH, and total Ca, Mg and Si content.* Perhaps this explains why when Chavagnac and others (2013b) sampled fluids from both the Voltri group of the Ligurian Ophiolite in Italy and the Samail Ophiolite in Oman, where aquifer rocks are variably serpentinized, they found that fluids from both localities have overlapping pH and total Ca, Mg, and Si content. Rather than major solutes, other species should be considered to further evaluate how the degree of alteration of the aquifer host rock affects the

resulting fluid chemistry. Serpentine and carbonate minerals can sequester certain trace elements (for example, B, U, Sr, Cl; Kodolanyi and others, 2012) during serpentinization and it follows that remobilization of these elements during further alteration of serpentinites could result in fluids with trace element compositions different from those where the host aquifer rocks are less altered. In addition to trace elements, data on timescales of reactions could be diagnostic as serpentinites would be less reactive than fresh harzburgites. Experiments show that olivine usually dissolves at a much faster rate than various polymorphs of serpentine (for example, see Pokrovsky and Schott (2000) and Oelkers (2001) for olivine, and Bales and Morgan (1985), Thom and others (2013), and Daval and others, (2013) for serpentine). Attaining hyperalkaline conditions would likely take a greater length of time when serpentinizing serpentinites rather than fresh ultramafic rocks.

Effects of Incorporating Mineral Solid Solutions

In the reaction paths discussed above we allow the dissolving primary minerals to be in solid solutions, but so far have discussed results of models where the precipitation of secondary minerals only as endmember compositions were considered. Studies of natural serpentines, however, show that both serpentine and brucite can incorporate Fe into their structures (O'Hanley and Dyar, 1993, 1998; Evans, 2008; Evans and others, 2012). In brucite the iron is present as Fe^{+2}, but in serpentine minerals iron can be both Fe^{+2} and Fe^{+3}. Therefore, additional calculations were conducted to compare results incorporating solid solutions in product phases, as shown in figure 10, with results shown in figure 3 where alteration product solid-solutions were not considered. These calculations share features with those of McCollom and Shock (1998), McCollom and Bach (2009) and Klein and others (2009, 2013) where ideal site mixing was assumed for most solid solutions. The serpentine structure incorporates Fe^{+3} either through ferri-Tschermack's substitution in octahedral and tetrahedral sites [towards the Mg-cronstedtite ($(Mg_2Fe^{+3})(Fe^{+3}Si)O_5(OH)_4$) endmember] or through an octahedral vacancy model [towards the hisingerite ($([]Fe^{+3}_2)Si_2O_5(OH)_4$) endmember] as shown by O'Hanley and Dyar (1993, 1998), Evans (2008), Andreani and others (2013), and Tutolo and others (2019). To accommodate Fe^{+3} incorporation in both octahedral and tetrahedral sites in serpentine, a four member (chrysotile, greenalite, Mg-cronstedtite, hisingerite) ideal mixing model was used in our calculations.

Trends are plotted against overall reaction progress showing the number of moles of precipitated Mg-, Fe-, and Si-bearing minerals in figure 10A, and concentrations of aqueous H_2, and total dissolved Si, Mg, and Fe in figure 10B. Total dissolved Ca, DIC, and other minerals that do not differ meaningfully from results in figure 3 are not included. Earlier stages (1 – 3) of reaction progress are also not shown as the models give nearly identical results.

Overall mineralogical trends.—If solid solutions are not considered, the only secondary minerals that can host Fe throughout the overall serpentinization progress are goethite and magnetite, as depicted as the solid black curves in figure 10A. If solid solutions are allowed, at later stages of the reaction progress most of the Fe will be incorporated into brucite and serpentine instead of magnetite, as shown by the dashed gray lines in figure 10A. This is consistent with observations showing brucite and serpentine as the major iron-hosting precipitates in low-temperature serpentinites rather than magnetite, which forms more readily during high-temperature (>250 °C) serpentinization (Klein and others, 2014). In all other cases iron released during alteration goes into either serpentine or brucite. As they first form, serpentine and brucite are Mg-rich, and increasingly incorporate Fe as reactions progress toward higher rock:water ratios. Despite incorporating some Fe, serpentine remains Mg-rich (X_{Mg} = Mg/(Mg+Fe) = 0.94) at latter stages of reaction progress, and a significant amount of the iron is incorporated into brucite (X_{Mg} = 0.83). These predictions are

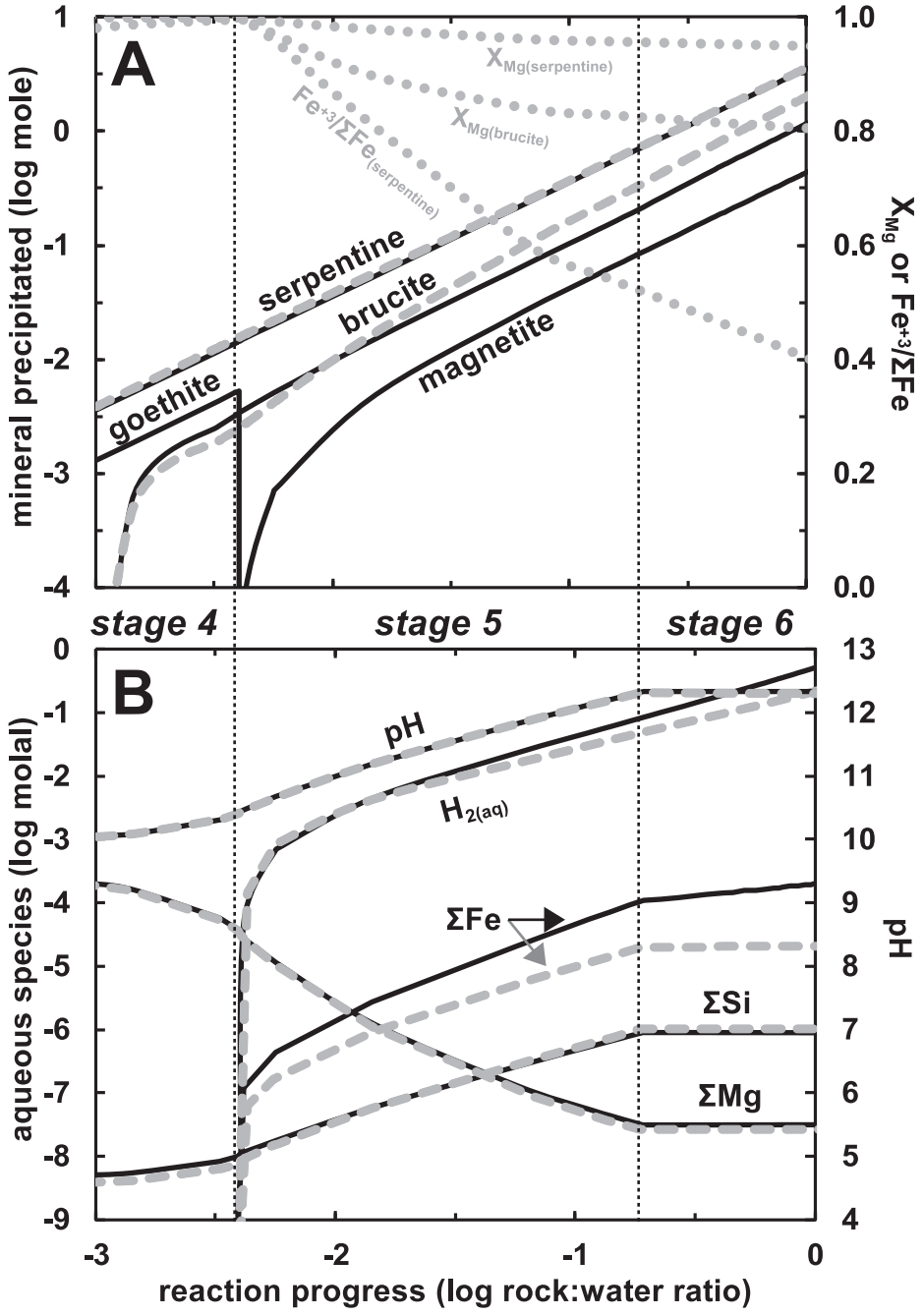

Fig. 10. Reaction path differences at 25 °C and 1 bar in models where precipitation of secondary phases in solid solutions were (dashed gray) and were *not* (solid black) considered. Trends in secondary precipitation (moles precipitated) and aqueous concentration (pH and molal concentration) are depicted in (A) and (B), respectively. Also plotted in (A) as dotted gray lines (values on right y-axis) are the mole fraction of Mg (X_{Mg} = Mg/(Mg + Fe)) in precipitating serpentine and brucite, and the $Fe^{+3}/\Sigma Fe$ of precipitating serpentine in models allowing solid solutions. The vertical black dashed lines indicate the start and end of stages 4–6 of the serpentinization process summarized in figure 2C.

consistent with observations from serpentine (X_{Mg} = 0.92–0.94) and brucite (X_{Mg} = 0.82–0.84) veins cutting olivine in partially serpentinized dunites from New Caledonia (Frost and others, 2013). At low rock:water ratios $Fe^{+3}/\Sigma Fe$ in precipitating serpentine is elevated, and decreases as the system becomes more rock dominated and reduced. This is consistent with low $Fe^{+3}/\Sigma Fe$ (<0.50) of serpentine determined by Mayhew and others (2018) and Andreani and others (2013) in the least serpentinized samples, and high values (>0.70) in highly altered samples that formed in fluid-dominated environments. As shown in figure 10A, serpentine with $Fe^{+3}/\Sigma Fe > 0.70$ would only occur in fluid-dominated systems characterized by relatively low rock:water ratios $< 10^{-1.5}$ and relatively oxidized fluids.

The $\alpha SiO_{2(aq)}$ of a fluid in equilibrium with the Fe^{+2} endmembers of serpentine and brucite, as depicted by the reaction

$$3Fe(OH)_{2(Fe\text{–}brucite)} + 2SiO_{2(aq)} \rightarrow Fe_3Si_2O_5(OH)_{4(greenalite)} + H_2O, \quad (29)$$

is slightly higher at 25 °C and 1 bar ($10^{-7.9}$) than that constrained by the Mg^{+2}-end members ($10^{-8.9}$, see rxn 11). The incorporation of Fe into both serpentine and brucite shifts the $\alpha SiO_{2(aq)}$ to slightly higher values and the $\alpha Mg^{+2}/(H^+)^2$ to lower values, consistent with the minor differences in pH, and total Mg and Si concentrations between the two models (fig. 10B). In contrast, a major difference between the two models is the resulting total dissolved Fe concentration depicted in figure 10B. In the model where Fe incorporation into serpentine and brucite is prohibited, the total dissolved Fe will be controlled by magnetite solubility. If solid solutions are allowed, the resulting total dissolved Fe will be a response to the precipitation of both Fe-bearing serpentine and brucite, yielding lower concentrations of total dissolved Fe.

Implications for H_2 generation.—In addition to differences in dissolved Fe, models that do or do not include serpentine and brucite solid solutions result in differing amounts of H_2 generated, which is tied to the amount of ferrous iron from the primary minerals that was oxidized and hosted as ferric iron in the secondary phases (see rxn 13). Bach (2016) demonstrated differing trends of H_2 generation applied to low-temperature serpentinization of the seafloor depending on the model used. In this work, we discuss implications of using models with and without solid solutions for continental serpentinization. As shown in figure 10B, the model allowing only magnetite formation will generate more than ~2 times as much H_2 as the model that allows Fe incorporation into serpentine and brucite. These differences, weighted per kg of reacting rock, are depicted in figure 11 as functions of rock:water ratio. Before Stage 5 of overall reaction progress, neither model produces H_2 as O_2 from the atmosphere is still present and available to oxidize iron. Once O_2 is consumed, H_2O will start to oxidize Fe and will, in turn, be reduced to H_2. Allowing the formation of ferric iron-hosting serpentine ($Fe^{+3}/\Sigma Fe$ <0.67 for most of Stages 5 and 6, fig. 10A) will generate H_2, but not as much as models in which magnetite ($Fe^{+3}/\Sigma Fe$ = 0.67) is the only Fe-bearing phase allowed to precipitate. Both models predict similar potentials to generate H_2 only over a small interval of reaction progress right after the beginning of stage 5, as shown in figures 10 and 11, when the $Fe^{+3}/\Sigma Fe$ of serpentine remained > 0.67. As shown in figure 11, at rock:water ratio = 1, the amount of H_2 generated through serpentine formation [0.18 mole H_2 (kg harzburgite)$^{-1}$] is less than half as much as can be generated when magnetite is assumed to be the only Fe-bearing alteration product [0.43 mole H_2 (kg harzburgite)$^{-1}$].

It can be anticipated that variations in the composition of the reacting rock will affect the amount of H_2 generated. Results as functions of the ratio of primary olivine to orthopyroxene, all with minor clinopyroxene, are depicted in figure 12. The pH, secondary assemblages (dashed gray lines), and X_{Mg} of the secondary phases (dotted gray lines) are shown in figure 12A for a rock:water ratio of 1. As discussed above,

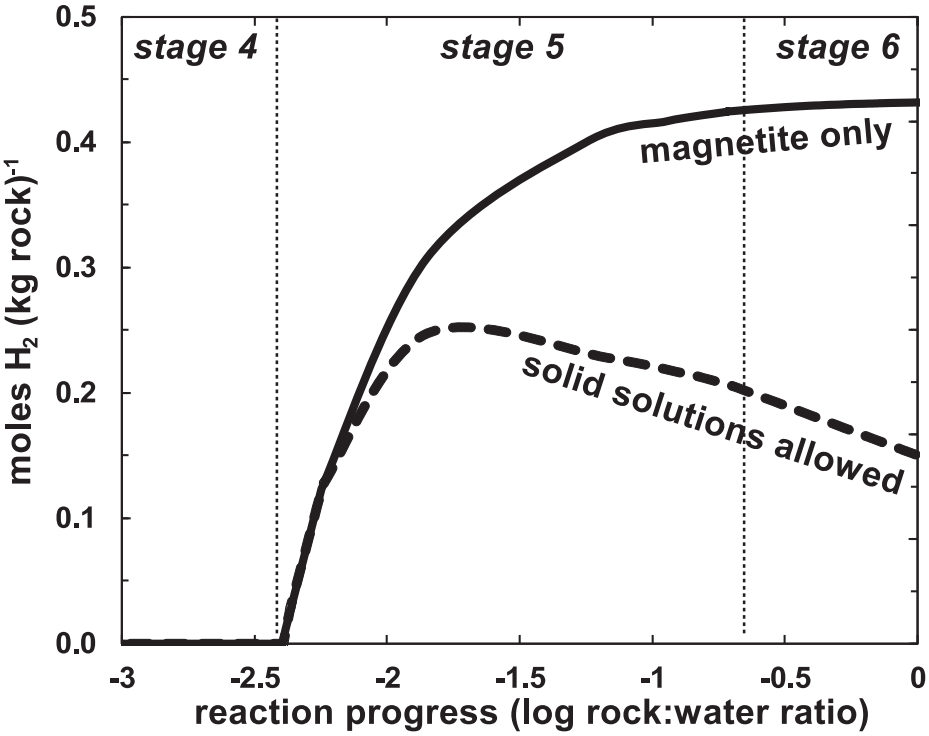

Fig. 11. Predicted amount of H_2 generated per kg of rock at rock:water ratios ranging from 10^{-3} to 10^{0} in models assuming only magnetite as the Fe-hosting phase (solid black) and those where Fe is allowed to be incorporated into serpentine and brucite (dashed black).

alteration of olivine-rich lithologies (left side of fig. 12A) results in assemblages comprised of serpentine + brucite and the high pH (>12) of the fluid will be dictated by Ctl-Brc-Di equilibrium. Compositions of fluids shift from that constrained by the Ctl-Brc-Di equilibrium to that of Ctl-Tr-Di (pH ~11) as the primary mineral assemblage being altered shifts to one dominated by orthopyroxene. Alteration of systems containing even more orthopyroxene (right side of fig. 12A) yields serpentine + talc assemblages and lower pH (~10) set by the Ctl-Tlc-Tr equilibrium.

How iron is hosted in the secondary assemblage is shown in figure 12B. Most of the iron is incorporated into serpentine despite variabilities in rock compositions. Some amount of iron is hosted in brucite in olivine-dominated systems but shifts to talc as orthopyroxene becomes more dominant. Changes in the $Fe^{+3}/\Sigma Fe$ ratio of the precipitating serpentine are also shown in figure 12B. The ratio remains relatively constant in either olivine- and orthopyroxene-dominated lithologies, but at starkly contrasting values. As shown in figure 12B, a shift to orthopyroxene-dominated lithologies will cause an abrupt drop (~6×) in the $Fe^{+3}/\Sigma Fe$ ratio of the precipitating serpentine. This shift can be represented by the reaction

$$3Fe^{+2}{}_2Fe^{+3}{}_2SiO_5(OH)_{4(\text{cronstedtite})} + 5SiO_{2(aq)} + 3H_2 \rightarrow 4Fe^{+2}{}_3Si_2O_5(OH)_{4(\text{greenalite})} + H_2O, \quad (30)$$

which favors the more Si-rich ferrous-iron bearing serpentine component (greenalite) relative to the dominant ferric-iron bearing serpentine component (cronstedtite) as

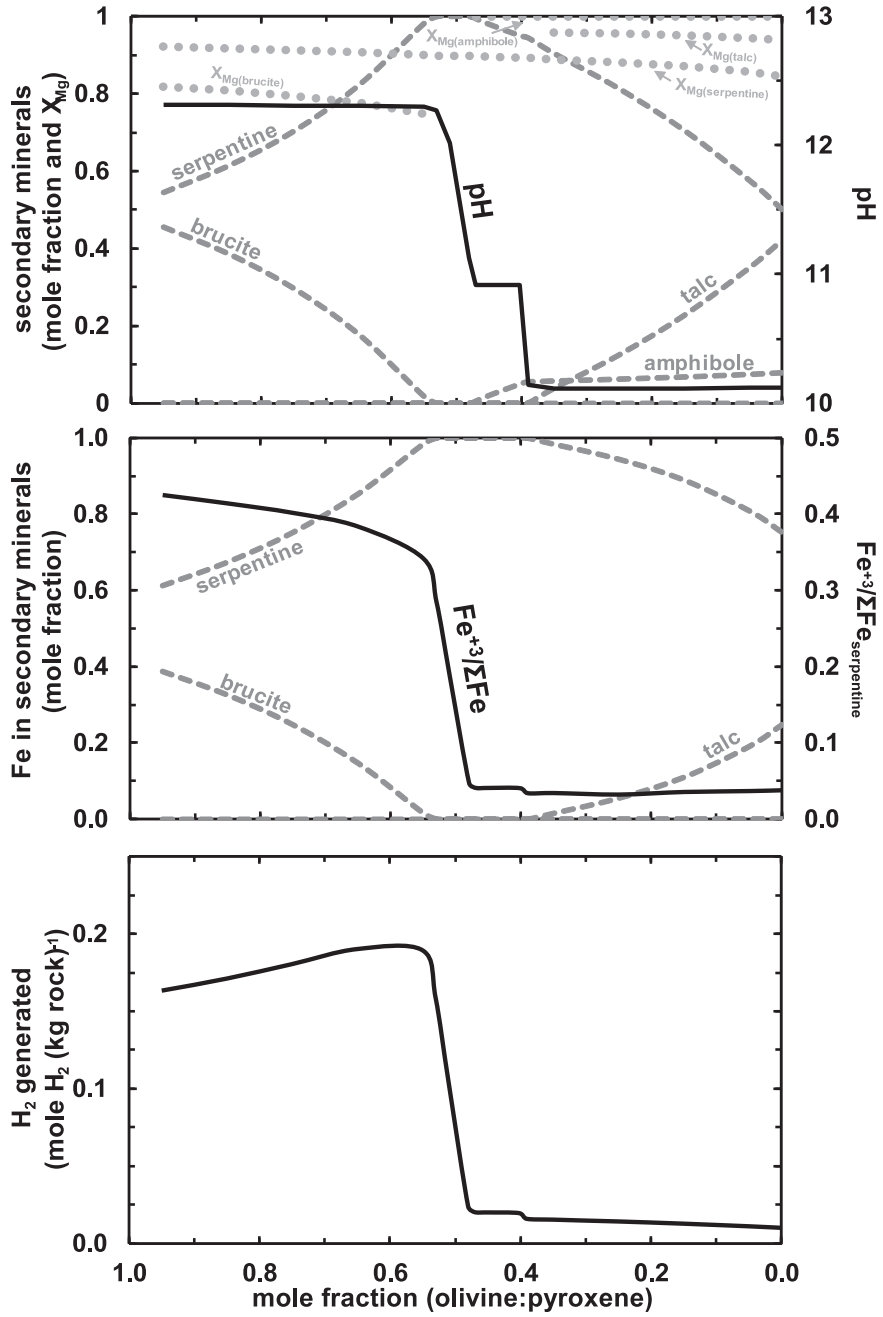

Fig. 12. (A) Trends in secondary assemblages and pH values of fluids resulting from the alteration of ultramafic rocks with variable contributions from olivine and orthopyroxene (clinopyroxene constant at 5 mol% contribution). Dashed gray curves depict the mole fraction of the mineral indicated in the total secondary assemblage. Dotted gray curves show the X_{Mg} of each mineral. (B) shows how iron is hosted in the secondary assemblages. Solid black curve in (B) indicates the $Fe^{+3}/\Sigma Fe$ of the precipitating serpentine. (C) indicates the predicted amount of H_2 generated per kg of rock. Values shown in this figure are from results of simulations of alteration of rock with composition depicted by Model A at rock:water = 1, 25 °C, and 1 bar.

the bulk composition shifts toward the more Si-rich orthopyroxene-dominated lithologies. Reaction (30) is a simplified illustration compared with our calculations that account for ideal solid solution mixing among end-member components (chrysotile, greenalite, Mg-cronstedtite, and hisingerite) of serpentine.

The distribution of iron into alteration phases causes variations in the amount of H_2 generated per kg of reacting rock as shown in figure 12C. As the reacting rocks become less olivine-rich the calculated abundance of H_2 increases owing to the increased proportion of iron being incorporated into serpentine, which hosts both ferrous and ferric iron, relative to that going to form brucite, which only hosts ferrous iron. The shift from cronstedtite to greenalite in the alteration assemblage means that the amount of H_2 generated during the alteration of orthopyroxene-dominated lithologies is less than that from alteration of olivine-dominated systems. The results summarized in figure 12 have similarities to those of Klein and others (2013), who showed that the amount of H_2 generated through seawater-ultramafic interaction depends on the composition of the reacting rocks. The maximum H_2 generated (0.2 moles H_2 kg^{-1} rock) shown in figure 12C is two times less than that attained by only allowing iron incorporation into magnetite. Sherwood-Lollar and others (2014) estimated the global flux of H_2 ($0.2–1.8 \times 10^{11}$ mole H_2 $year^{-1}$) from continental serpentinization using reactions to magnetite. If considering Fe incorporation into serpentine and brucite during low-temperature serpentinization, reevaluation of this flux would amount to $0.1–0.9 \times 10^{11}$ mole H_2 $year^{-1}$.

BIOENERGETIC LANDSCAPES

Results of numerical models by McCollom (2007), Amend and others (2011), and Nakamura and Takai (2014) show that deep-sea ultramafic-hosted hydrothermal systems can supply more energy to chemolithotrophs than analogous hydrothermal systems generated through basalt-seawater interactions. Moreover, these calculations show that the predominant sources of energy are from reactions that involve H_2 and CH_4. Similar findings were observed for analogous serpentinization-generated fluids in continental settings (Cardace and others, 2015; Canovas and others, 2017; Crespo-Medina and others, 2017). Though Canovas and others (2017) inferred the likelihood of several metabolic reactions in the subsurface, available energy supplies for subsurface microorganisms in serpentinizing environments have yet to be quantified. The framework presented above allows us to calculate energy supplies available in the deep subsurface using predicted compositions of fluids close to equilibrium with the host rock, as well as the energy available as these reduced rock-equilibrated fluids mix with oxic groundwater. Details on calculations of instantaneous energetic returns for a metabolic reaction can be found in McCollom and Shock (1997), McCollom (2007), Shock and others (2010), Amend and others (2011) and Canovas and others (2017).

Here, we focus on two microbial metabolisms: hydrogen oxidation, and methanogenesis as described, respectively, by

$$2H_{2(aq)} + O_{2(aq)} \rightarrow 2H_2O, \tag{31}$$

and

$$CO_{2(aq)} + 4H_{2(g)} \rightarrow CH_{4(aq)} + 2H_2O. \tag{32}$$

Methanogens may also use CO_3^{-2} and HCO_3^- as inorganic carbon sources especially at hyperalkaline conditions typical of serpentinizing environments. Methanogenesis from CO_3^{-2} is depicted in reaction (14) while that for HCO_3^- can be described by

$$HCO_3^- + 4H_{2(aq)} + H^+ \rightarrow CH_{4(aq)} + 3H_2O. \tag{33}$$

As shown in figure 4E, most of the dissolved inorganic carbon in Ca-rich, hyperalkaline fluids generated through serpentinization exist as the neutral complex $CaCO_{3(aq)}$ and would comprise the major dissolved source of inorganic carbon available for methanogens via

$$CaCO_{3(aq)} + 4H_{2(aq)} + 2H^{+} \rightarrow Ca^{+2} + CH_{4(aq)} + 3H_2O. \quad (34)$$

We chose hydrogen oxidation and methanogenesis because they are known metabolisms from serpentinizing environments, and because the subsurface concentration of the various aqueous species involved in the reactions can be constrained through mineral-fluid equilibria. Hydrogen oxidizers growing with calcite as their carbon source and belonging to the proposed genera *Serpentinomonas* were isolated by Suzuki and others (2014) from hyperalkaline springs in the Cedars, Coast Range, California. Experiments using isotopically labeled carbon (^{13}C) by Brazelton and others (2011) and Kohl and others (2016) at Lost City and the Cedars, respectively, show evidence for microbial methane generation from various inorganic and organic substrates. Lipid biomarker analysis also provides evidence for microbial methanogenesis at Lost City on the mid-Atlantic ridge (Bradley and others, 2009). Further evidence for microbial H_2 oxidation and methanogenesis in both submarine and continental serpentinizing sites is provided by metagenomic, 16S rRNA, and 16S rDNA analyses by Schrenk and others (2004), Brazelton and others (2006, 2012, 2013, 2017), Blank and others (2009), Tiago and Veríssimo (2013), Suzuki and others (2013), Sánchez-Murillo and others (2014), Quéméneur and others (2014, 2015), Crespo-Medina and others (2014; 2017); Postec and others (2015), Woycheese and others (2015), Baculi and others (2015), Miller and others (2016), Twing and others (2017), Rempfert and others (2017), and Fones and others (2019).

We calculated the energetic returns for microbial H_2 oxidation (rxn 31) and microbial methanogenesis (rxns 14, 32, 33 and 34) in fluids close to equilibrium with ultramafic rocks as constrained through fluid-mineral equilibria calculations discussed above. Dissolved H_2 concentrations of deep-seated reduced fluids were assumed to be in equilibrium with one bar of $H_{2(g)}$, which can be considered as a minimum for a deeply serpentinizing aquifer. Discussion of figure 3A above shows that an H_2 overpressurized system can occur at advanced stages of reaction progress. Higher dissolved H_2 would potentially increase energetic returns for both microbial methanogenesis and H_2 oxidation. There will be no energy available from reactions (14), (32), (33) and (34) if abiotic CH_4 generation is allowed to proceed and equilibrate. However, if abiotic CH_4 generation is kinetically inhibited during low-temperature serpentinization, conditions favorable for microbial methanogenesis will develop. As discussed above (see Stage 5), sluggish abiotic methane generation can result in DIC remaining in solution late in the overall serpentinization reaction progress and that DIC will be out of equilibrium with high concentrations of dissolved H_2. At the pH dictated by the Ctl-Brc-Di equilibria (pH = 12.3; at 25 °C and 1 bar), the calculated DIC concentration is ~8 μmolal if it is in equilibrium with calcite. Assuming minimal background methane ($<10^{-12}$ molal) and H_2 concentrations implied above (in equilibrium with 1 bar of $H_{2(g)}$), calculations of energetic returns for microbial methanogenesis with inorganic carbon (rxns 14, 32, 33, and 34) will yield ~ 0.2 calories kg^{-1} (0.9 joules kg^{-1}) of fluid. An increase in DIC concentration would draw fluids away from being in equilibrium with diopside (Ctl-Brc-Di) to calcite (Ctl-Brc-Cal) and shift the fluid composition to lower pH. The resulting change in the energy available for methanogens as DIC concentrations increase is shown in figure 13. An increase in DIC and a decrease in pH will drive reactions (14), (32), (33), and (34) forward, ultimately increasing the energy that can be available for methanogens to exploit. As an example, a fluid in equilibrium with calcite at higher DIC (50 μmole kg^{-1}) and lower pH

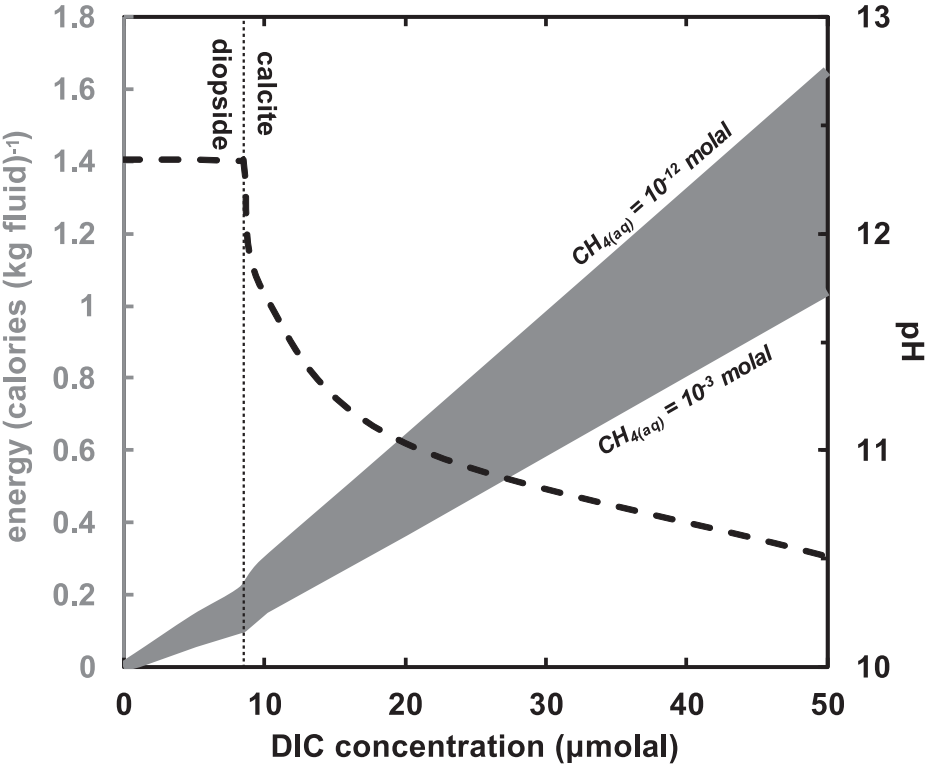

Fig. 13. Predicted energy (calories/kg fluid) available for hydrogenotrophic methanogenesis in deep-seated fluids close to equilibrium with the rocks at 25 °C and 1 bar. Fluid compositions were derived from fig. 6B, which shows that deep-seated fluids are likely close to Ctl-Brc-Di (pH ~12 at 25 °C). At higher DIC concentrations, fluid can saturate with calcite and pH will be dictated by the Ctl-Brc-Cal equilibrium with higher DIC concentrations resulting in lower pH (dashed line). The solid gray area indicates ranges in the energy yield assuming variable background methane concentrations ranging from 10^{-12} to 10^{-3} molal.

(~10.5) will yield energy amounting to 1.7 calories kg^{-1} (7 joules kg^{-1}) of fluid, which is close to 10 times higher than that calculated above for a fluid in equilibrium with diopside. Calculations at higher background methane (10^{-3} mole kg^{-1}) yield less energy as there is a lower drive for reactions (14), (32), (33), and (34) to proceed. However, despite the 9 orders of magnitude change in abundance of dissolved CH_4 this will reduce the energy yield at most by half. We allow up to 50 μmolal of DIC despite predicted DIC concentrations of deep-seated hyperalkaline of < 20 μmolal (fig. 6A) to accommodate minor input from infiltrating atmosphere-derived volatiles during fluid discharge. Another process that can bring additional inorganic carbon sources to deep-seated fluids is mixing with DIC-rich shallow groundwater. Consequences of mixing are discussed below.

There is no energy available for H_2 oxidation at deep subsurface environments owing to the predicted absence of $O_{2(aq)}$ at advanced stages of serpentinization. However, hydrogen oxidizing bacteria in the genus *Hydrogenophaga* were detected from high pH subsurface fluids in Oman (Miller and others, 2016; Rempfert and others, 2017) implying that O_2 could have been available in the subsurface through atmospheric infiltration or mixing with oxic groundwater. Subsurface methanogens were also detected in the same studies. We demonstrate above that energy can be available for microbial methanogenesis, but not for H_2 oxidation, for a deep-seated fluid

without atmospheric and shallow groundwater input. Delivery of additional DIC through atmospheric and shallow groundwater mixing, however, can potentially increase energetic returns. These processes may occur in discharge zones where surfacing deep-seated hyperalkaline fluids can encounter shallow groundwater.

In our mixing calculations we used predicted compositions of deep-seated rock-equilibrated fluids and oxic shallow groundwaters in equilibrium with the atmosphere and altered rocks (serpentinites, carbonates) common in the shallow subsurface, and chose 25 °C and 1 bar for both types of fluid. For the shallow groundwater, we set the pH = 8 based on measurements from well samples ($7 < pH < 9$, Paukert and others, 2012, 2019; Rempfert and others, 2017). This choice of pH is also supported by mineral saturation calculations by Paukert and others (2012) on groundwater fluids from the Oman Ophiolite showing that equilibrium with serpentine, magnesite, and calcite at pH = 8 will yield a Mg-HCO_3 type fluid close in composition to that observed in the field. For the deep-seated, rock-equilibrated fluid we used four different compositions to represent end-member possibilities, all at 25 °C and 1 bar including a fluid in equilibrium with Ctl-Brc-Di plus calcite, and fluids in equilibrium with Ctl-Brc-Cal at DIC concentrations of 10, 20, and 50 μmolal. We assumed minimal background methane (10^{-12} molal) to quantify maximum energy yields for methanogenesis. Further compositional details of end-member fluids used in our mixing calculations can be found in table A1.

The calculated energies available for hydrogen oxidation and methanogenesis during the subsurface mixing process are shown in figure 14. Trends in pH during the mixing process are shown in figure 14A. Note that the deep-seated fluid in equilibrium with diopside (pH = 12.3) and that in equilibrium with calcite at 10 μmolal DIC (pH = 11.7) are strong bases. As a consequence, it would take more than 80 percent or 50 percent mixing with shallow groundwater, respectively, for the pH of the mixed fluid to be <11. Energetic returns for hydrogen oxidation and methanogenesis are shown in figure 14B. The curve for methanogenesis (thick gray curve in fig. 14B) represents mixing trends for the four deep-seated endmember fluids. These fluids have different starting pH and DIC concentrations contributing to differences in energetic yields (see fig. 13). The thickness of the curve represents this variation. In contrast, the energy yield for H_2 oxidation does not vary among these four endmember fluids resulting in the thin curve shown. As discussed above, energy is available for methanogens even without mixing with shallow groundwater. Fluids that started with more DIC, such as those in equilibrium with calcite, yield more energy throughout the mixing process than those starting with less DIC in equilibrium with diopside. The difference, however, becomes less apparent (thinner gray curve) as the mixed fluid is increasingly dominated by shallow groundwater. Maximum energy availabilities for methanogenesis (6 calories kg^{-1} or 25 joules kg^{-1} of fluid) are attained at mixing extents of < 30% and the amounts of energy available decrease with increasing progress of mixing. In contrast, no energy is available for H_2 oxidation before mixing occurs, but becomes available at the first instance of mixing. Compared to methanogenesis, energetic returns for H_2 oxidation maximize at greater extents of mixing (~60%) yielding energy of 17 calories kg^{-1} (72 joules kg^{-1}) of fluid. Changes in the direction of the energetic trends for both methanogenesis and hydrogen oxidation indicate a transition depending on which of the reactants is limiting (DIC or H_2 for methanogenesis, O_2 or H_2 for hydrogen oxidation). Trends shown in figure 14B hint that methanogens could be favored in fluids characterized by no to low extents of mixing, while H_2 oxidizers would prefer systems characterized by higher extents of mixing.

Energetic returns inferred for the continental serpentinizing subsurface are far less than what has been calculated for analogous mixing process accompanying fluid venting in deep sea hydrothermal environments. As an example, McCollom (2007)

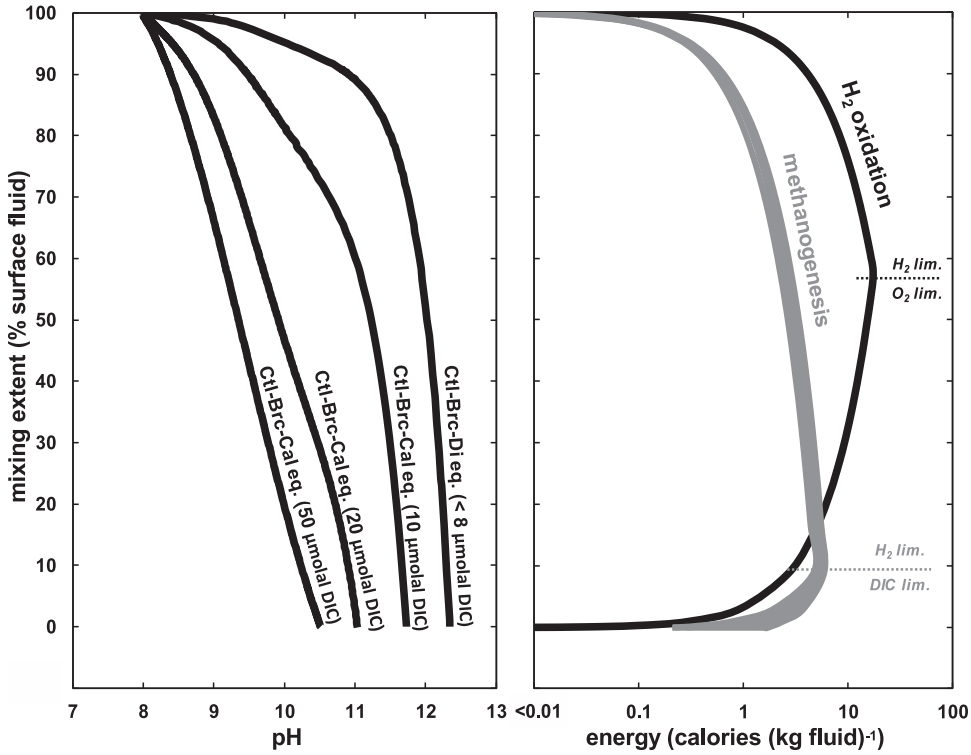

Fig. 14. (A) pH and (B) energy yields for H_2 oxidation and methanogenesis during mixing between fluids that equilibrated with deep-seated rocks (Ctl-Brc-Di and Ctl-Brc-Cal, bottom of (B)) and those that equilibrated with the highly altered shallow aquifer host rocks (top of (B)) at 25 °C and 1 bar. The four curves in (A) depict trends for pH during mixing for four deep-seated end-member fluids with variable starting DIC following fig. 6B: fluid in equilibrium with Ctl-Brc-Di and fluids in equilibrium with Ctl-Brc-Cal at DIC concentrations of 10, 20, and 50 µmolal. These four starting end-member fluids result in little differences in energy yield for methanogenesis as the mixing process progresses and are therefore depicted as one thick gray curve in (B). The thickness of the curve represents variations in energy bounded by that yielded by a fluid in equilibrium with Ctl-Brc-Di as the minimum and a fluid in equilibrium with Ctl-Brc-Cal at DIC concentrations of 50 µmolal as the maximum. Trends for H_2 oxidation are similar for these different starting fluids and are shown as one black curve in (B). Thin dashed lines in (B) indicate transition points for the limiting reactant.

calculated maximums of ~100 and ~900 calories kg^{-1} for methanogenesis and hydrogen oxidation, respectively, during vent fluid-seawater mixing. Nevertheless, despite being limited, available subsurface energy that can be exploited by microorganisms permits the possibility of deep communities in serpentinizing aquifers. Moreover, the above calculations also highlight discharge zones of fluid pathways as hotspots where subsurface life may bloom as reduced deep-seated fluids encounter oxidized shallow-aquifer fluids.

Communities observed in serpentinizing systems are not limited to H_2 oxidation and methanogenesis (Schrenk and others, 2013; Canovas and others, 2017). A more comprehensive theoretical evaluation of subsurface energy available for various metabolic process is possible once concentrations of relevant aqueous and gaseous species are constrained. In addition, constraints on organic compounds, such as formate and acetate, can provide insights into the likelihood of deep subsurface methanogens using substrates other than inorganic carbon. As shown in figure 13, simulations starting with various background concentrations of dissolved CH_4 do not dramatically change the

calculated energy yields for methanogenesis. These yields would, however, influence the energy available for aerobic and anaerobic methanotrophs. Constraints on deep subsurface CH_4 concentrations will help assess the likelihood of subsurface methanotrophy, as well as refine the energetic returns for methanogens calculated above. Calculations of fluid-mineral equilibria constraining the dissolved sulfide and sulfate concentrations of deep-seated fluids will help quantify energy available for various sulfur-based metabolic processes. Similarly, constraints on dissolved nitrogen species such as ammonia, nitrite and nitrate will allow predictions of energy available for nitrogen-based metabolic reactions. We have inferred the dissolved ferrous iron concentrations of the deep subsurface through fluid-mineral equilibria with magnetite and iron-bearing brucite and serpentine, which can be used to assess energy available for iron oxidizers once more is known about iron oxidizing metabolisms in hyperalkaline systems. Constraints on the available ferric-iron hosting phases (magnetite, Fe^{+3}-bearing serpentine) can also help in quantifying energy available for iron reducing microbes.

CONCLUDING REMARKS

Our goals in conducting this evaluation of environments generated by low-temperature serpentinization of ultramafic rocks in continental settings are to explore various reactions that drive the serpentinization process and their consequences for the concentrations of various aqueous species. By accounting for variable temperatures, salinities, host-rock compositions, and degree of alteration (fresh ultramafic rock *vs* serpentinites) we demonstrate that equilibrium thermodynamic calculations account for the highly alkaline fluids recorded in serpentinizing environments. In light of the sluggish approach to equilibrium at low temperatures, these calculations provide robust tools for exploring the consequence of mass-transfer processes at ambient conditions. An example is the apparent mismatch between measured pH values of serpentinized fluids and calculations that assume equilibrium with idealized mineral assemblages. As described above, pH and composition will shift as a fluid moves from being in equilibrium with diopside to being in equilibrium with calcite as it encounters more DIC through transport processes like fluid mixing and atmospheric input. We have shown that these processes can account for most pH values measured in hyperalkaline fluids in Oman. Nevertheless, variabilities in the chemistry of serpentinization-generated fluids can also be consequences of reactive-transport processes where reactions are kinetically controlled (Tutolo and others, 2018). Calling upon kinetic constraints is warranted after exhausting equilibrium arguments.

Our calculations also extend the findings of previous work by Klein and others (2009, 2013, 2014) who showed that Fe is favorably incorporated into serpentine and brucite, instead of magnetite, during low-temperature serpentinization. When Fe transport occurs without oxidation there is a diminished potential for H_2 generation. Results of our work show that the modern H_2 flux could be two times lower ($0.1–0.9 \times 10^{11}$ mole H_2 $year^{-1}$) than recent estimates (Sherwood-Lollar and others, 2014) that assume iron oxidation to magnetite. Thermodynamic properties of Mg-cronstedtite and hisingerite components of serpentine were estimated and incorporated in our model to account for observations in serpentinites (O'Hanley and Dyar, 1993, 1998; Tutolo and others, 2019). Refinement of the thermodynamic properties of Fe end-members and solid solution models of serpentinization-relevant secondary phases such as serpentine and brucite can help improve our models, especially for calculations on the amount of H_2 generated during low-temperature serpentinization. In addition, by evaluating energy supplies we show how potentials for microbial methanogenesis and hydrogen oxidation can be predicted in the deep serpentinizing subsurface. Energy is available for methanogens in the deep subsurface so long as DIC can be provided through calcite dissolution. Mixing of reduced, deep-seated, rock-equilibrated hyperal-

kaline fluids with shallow groundwater permits hydrogen oxidation, and can provide additional sources of energy that can be exploited by microbes. Further constraints on the chemistry of subsurface fluids, which will soon be available through the Oman Drilling Project will allow a comprehensive evaluation on the habitability of the deep serpentinizing subsurface. Finally, the predictions set forth in this study provide a rigorous framework for testing ideas that can explain the compositions and microbial communities of fluids sampled at the surface in hyperalkaline spring and seeps.

ACKNOWLEDGMENTS

Thanks to Alta Howells, Kirt Robinson, Peter Canovas, Tucker Ely, Grayson Boyer, Vincent Milesi, and Alysia Cox for many helpful discussions over the course of this study. We would like to thank Benjamin Tutolo and an anonymous reviewer for helpful and insightful reviews. Our work has also benefitted from ideas and data shared by Peter Kelemen, Isabelle Daniel, Muriel Andreani, Juerg Matter, and the NASA Astrobiology Institute Rock Powered Life team. We recognize support from NSF grant EAR 1515513, and the NASA Astrobiology Institute Rock-Powered Life project.

TABLE A1

Composition of fluids used in reaction path and mixing calculations

	Rainwater[1]	Shallow Groundwater[2]	Deep Subsurface Fluid A[3]	Deep Subsurface Fluid B[4]	Deep Subsurface Fluid C[5]	Deep Subsurface Fluid D[6]
pH	5.6	8	12.3	11.7	11.1	10.6
ΣNa (mmole/kg)[7]	0.15	1	10	10	10	10
ΣCa (mmole/kg)	0.008	0.6	14.4	3.2	0.7	0.3
ΣMg (μmole/kg)	21	1700	0.03	0.2	2.6	20
ΣCl (mmole/kg)[7]	0.17	1	10	10	10	10
ΣSi (μmole/kg)	0.7	100	1.3	0.3	0.07	0.02
DIC (μmole/kg)	13	2070	8	10	20	50
DO (mmole/kg)[8]	0.3	0.3	0	0	0	0
$H_{2(aq)}$ (mmole/kg)[9]	0	0	0.75	0.75	0.75	0.75

[1]modified from Hao and others (2017).
[2]calculated for a fluid in equilibrium with chrysotile, calcite, magnesite, and the atmosphere at 25°C and 1 bar. pH given as 8 (see text).
[3]fluid in equilibrium with the Ctl-Brc-Di and calcite assemblage at 25°C and 1 bar.
[4]fluid in equilibrium with the Ctl-Brc-Cal assemblage, given 10 μmole/kg DIC, at 25°C and 1 bar.
[5]fluid in equilibrium with the Ctl-Brc-Cal assemblage, given 20 μmole/kg DIC, at 25°C and 1 bar.
[6]fluid in equilibrium with the Ctl-Brc-Cal assemblage, given 50 μmole/kg DIC, at 25°C and 1 bar.
[7]shallow and deep fluids were given ionic strengths equivalent to a 1 and 10 millimole/kg NaCl solution, respectively, following environmental observations (Paukert and others, 2012; 2019).
[8]dissolved O_2 (DO) value for rain and shallow groundwater in equilibrium with the atmosphere at 25°C and 1 bar.
[9]value for deep subsurface fluids in equilibrium with one bar of $H_{2(g)}$ at 25°C.

TABLE A2

Summary of experimental and estimated thermodynamic data for end-member Fe-bearing serpentinization-relevant minerals used in this study

Mineral	Formula	$\Delta_f G°^{a,f}$	$\Delta_f H°^{a,g}$	$S°^{b,h}$	$V°^{c,h}$	$C_p°^{b,h}$	Maier-Kelley Coefficients		
							$a^{b,h}$	$b \times 10^{3d,h}$	$c \times 10^{-5e,h}$
Ferrous Hydroxide	$Fe^{+2}(OH)_2$	-117730[i]	-137340	21.0[j]	26[k]	21.3[l]	26.06[l]	4.35[l]	-5.38[l]
Ferrotremolite	$Ca_2Fe^{+2}{}_5Si_8O_{22}(OH)_2$	-2349100[m]	-2511300	163.5	283	169.2	197.93	58.95	-41.17
Greenalite	$Fe^{+2}{}_3Si_2O_5(OH)_4$	-716530	-787810	72.6	115	74.1	81.65	32.60	-15.39
Minnesotaite	$Fe^{+2}{}_3Si_4O_{10}(OH)_2$	-1070060	-1153380	83.5	148	88.5	88.31	42.61	-11.15
Mg-Cronstedtite	$(Mg_2Fe^{+3})(Fe^{+3}Si)O_5(OH)_4$	-789000[n]	-865180	60.8[o]	108[o]	71.8[o]	77.03[o]	40.52[o]	-15.40[o]
Hisingerite	$Fe^{+3}{}_2Si_2O_5(OH)_4$	-703430[n]	-777330	57.3[o]	105[o]	63.4[o]	68.77[o]	44.98[o]	-16.69[o]

a. cal mol^{-1}. b. cal mol^{-1} K^{-1}. c. cm^3 mol^{-1}. d. cal mol^{-1} K^{-2}. e. cal K mol^{-1}. f. unless otherwise noted, data taken from Wolery and Jove-Colon (2004). g. calculated using the $\Delta_f G°$ and S° data in the table along with the entropy of the elements from Wagman and others (1982). h. unless otherwise noted, data taken from Helgeson and others (1978). i. Sverjensky and Molling (1992) using data from Baes and Mesmer (1976). j. Wagman and others (1982). k. Wolery and Jove-Colon (2004) using data from Weast and Lide (1989). l. McCollom and Bach (2009). m. Sverjensky (1985). n. Calculated using methods consistent with Wolery and Jove-Colon (2004). o. Calculated using methods consistent with Helgeson and others (1978) using reactions $(Mg_2Fe^{+3})(Fe^{+3}Si)O_5(OH)_{4(Mg\text{-}Cronstedtite)} + Al_2O_3 \leftrightarrow (Mg_2Al)(AlSi)O_5(OH)_{4(Amesite)} + Fe_2O_3$ and $Fe^{+3}{}_2Si_2O_5(OH)_{4(Hisingerite)} + Al_2O_3 \leftrightarrow Al_2Si_2O_5(OH)_{4(Kaolinite)} + Fe_2O_3$ to calculate properties for Mg-Cronstedtite and Hisingerite, respectively.

REFERENCES

Abrajano, T. A., Sturchio, N. C., Bohlke, J. K., Lyon, G. L., Poreda, R. J., and Stevens, C. M., 1988, Methane-hydrogen gas seeps, Zambales Ophiolite, Philippines: Deep or shallow origin?: Chemical Geology, v. 71, n. 1–3, p. 211–222, https://doi.org/10.1016/0009-2541(88)90116-7

Abrajano, T. A., Sturchio, N. C., Kennedy, B. M., Lyon, G. L., Muehlenbachs, K., and Bohlke, J. K., 1990, Geochemistry of reduced gas related to serpentinization of the Zambales ophiolite, Philippines: Applied Geochemistry, v. 5, n. 5–6, p. 625–630, https://doi.org/10.1016/0883-2927(90)90060-I

Alexander, W. R., Dayal, R., Eagleson, K., Eikenberg, J., Hamilton, E., Linklater, C. M., McKinley, I. G., and Tweed, C. J., 1992, A natural analogue of high pH cement pore waters from the Maqarin area of northern Jordan. II: Results of predictive geochemical calculations: Journal of Geochemical Exploration, v. 46, n. 1, p. 133–146, https://doi.org/10.1016/0375-6742(92)90104-G

Allen, D. E., and Seyfried, W. E., 2004, Serpentinization and heat generation: Constraints from Lost City and Rainbow hydrothermal systems: Geochimica et Cosmochimica Acta, v. 68, n. 6, p. 1347–1354, https://doi.org/10.1016/j.gca.2003.09.003

Alt, J. C., and Shanks, W. C., 2003, Serpentinization of abyssal peridotites from the MARK area, Mid-Atlantic Ridge: Sulfur geochemistry and reaction modeling: Geochimica et Cosmochimica Acta, v. 67, n. 4, p. 641–653, https://doi.org/10.1016/S0016-7037(02)01142-0

Amend, J. P., McCollom, T. M., Hentscher, M., and Bach, W., 2011, Catabolic and anabolic energy for chemolithoautotrophs in deep-sea hydrothermal systems hosted in different rock types: Geochimica et Cosmochimica Acta, v. 75, n. 19, p. 5736–5748, https://doi.org/10.1016/j.gca.2011.07.041

Andreani, M., Muñoz, M., Marcaillou, C., and Delacour, A., 2013, μXANES study of iron redox state in serpentine during oceanic serpentinization: Lithos, v. 178, p. 70–83, https://doi.org/10.1016/j.lithos.2013.04.008

Bach, W., 2016, Some compositional and kinetic controls on the bioenergetic landscapes in oceanic basement: Frontiers in Microbiology, v. 7, n. 107, https://doi.org/10.3389/fmicb.2016.00107

Bach, W., Jöns, N., and Klein, F., 2013, Metasomatism within the ocean crust, *in* Harlov, D. E., and Austrheim, H., editors, Metasomatism and the Chemical Transformation of Rock: The Role of Fluids in Terrestrial and Extraterrestrial Processes: Berlin, Heidelberg, Springer, Lecture Notes in Earth System Sciences, p. 253–288, https://doi.org/10.1007/978-3-642-28394-9_8

Baculi, R. Q., Lantican, N. B., de los Reyes, F. L., and Raymundo, A. K., 2015, Prokaryotic community analysis of a hyperalkaline spring in the Philippines using 16S rRNA gene clone library construction: Philippine Journal of Science, v. 144, p. 1–15.

Baes, C. F., and Mesmer, R. E., 1976, The hydrolysis of cations: New York, Wiley, 489 p.

Bales, R. C., and Morgan, J. J., 1985, Dissolution kinetics of chrysotile at pH 7 to 10: Geochimica et Cosmochimica Acta, v. 49, n. 11, p. 2281–2288, https://doi.org/10.1016/0016-7037(85)90228-5

Barnes, I., and O'Neil, J. R., 1969, The relationship between fluids in some fresh alpine-type ultramafics and possible modern serpentinization, western United States: GSA Bulletin, v. 80, n. 10, p. 1947–1960, https://doi.org/10.1130/0016-7606(1969)80[1947:TRBFIS]2.0.CO;2

Barnes, I., LaMarche Jr., V. C., and Himmelberg, G., 1967, Geochemical evidence of present-day serpentinization: Science, v. 156, n. 3776, p. 830–832, https://doi.org/10.1126/science.156.3776.830

Barnes, I., Rapp, J. B., O'Neil, J. R., Sheppard, R. A., and Gude III, A. J., 1972, Metamorphic assemblages and the direction of flow of metamorphic fluids in four instances of serpentinization: Contributions to Mineralogy and Petrology, v. 35, p. 263–276, https://doi.org/10.1007/BF00371220

Barnes, I., O'Neil, J. R., and Trescases, J. J., 1978, Present day serpentinization in New Caledonia, Oman and Yugoslavia: Geochimica et Cosmochimica Acta, v. 42, n. 1, p. 144–145, https://doi.org/10.1016/0016-7037(78)90225-9

Barnes, I., Presser, T. S., Saines, M., Dickson, P., and Van Groos, A. F. K., 1982, Geochemistry of highly basic calcium hydroxide groundwater in Jordan: Chemical Geology, v. 35, n. 1–2, p. 147–154, https://doi.org/10.1016/0009-2541(82)90024-9

Bath, A., Christofi, N., Neal, C., Philp, J., Cave, M., McKinley, I., and Berner, U., 1987, Trace element and microbiological studies of alkaline groundwaters in Oman, Arabian Gulf: a natural analogue for cement pore-waters: British Geological Survey, Fluid Processes Research Group, 81 p.

Beard, J. S., and Hopkinson, L., 2000, A fossil, serpentinization-related hydrothermal vent, Ocean Drilling Program Leg 173, Site 1068 (Iberia Abyssal Plain): Some aspects of mineral and fluid chemistry: Journal of Geophysical Research: Solid Earth, v. 105, n. B7, p. 16527–16539, https://doi.org/10.1029/2000JB900073

Berner, E. K., and Berner, R. A., 2012, Global Environment: Water, Air, and Geochemical Cycles: Princeton, New Jersey, Princeton University Press, 464 p.

Blanc, Ph., Bourbon, X., Lassin, A., and Gaucher, E. C., 2010, Chemical model for cement-based materials: Thermodynamic data assessment for phases other than C–S–H: Cement and Concrete Research, v. 40, n. 9, p. 1360–1374, https://doi.org/10.1016/j.cemconres.2010.04.003

Blank, J. G., Green, S. J., Blake, D., Valley, J. W., Kita, N. T., Treiman, A., and Dobson, P. F., 2009, An alkaline spring system within the Del Puerto Ophiolite (California, USA): A Mars analog site: Planetary and Space Science, v. 57, n. 5–6, p. 533–540, https://doi.org/10.1016/j.pss.2008.11.018

Boschetti, T., and Toscani, L., 2008, Springs and streams of the Taro–Ceno Valleys (Northern Apennine, Italy): Reaction path modeling of waters interacting with serpentinized ultramafic rocks: Chemical Geology, v. 257, n. 1–2, p. 76–91, https://doi.org/10.1016/j.chemgeo.2008.08.017

Boschetti, T., Etiope, G., Pennisi, M., Romain, M., and Toscani, L., 2013, Boron, lithium and methane isotope composition of hyperalkaline waters (Northern Apennines, Italy): Terrestrial serpentinization or mixing with brine?: Applied Geochemistry, v. 32, p. 17–25, https://doi.org/10.1016/j.apgeochem.2012.08.018

Boulart, C., Chavagnac, V., Monnin, C., Delacour, A., Ceuleneer, G., and Hoareau, G., 2013, Differences in gas venting from ultramafic-hosted warm springs: The example of Oman and Voltri Ophiolites: Ofioliti, v. 38, n. 2, p. 142–156, https://doi.org/10.4454/ofioliti.v38i2.423

Bradley, A. S., Fredricks, H., Hinrichs, K.-U., and Summons, R. E., 2009, Structural diversity of diether lipids in carbonate chimneys at the Lost City Hydrothermal Field: Organic Geochemistry, v. 40, n. 12, p. 1169–1178, https://doi.org/10.1016/j.orggeochem.2009.09.004

Brazelton, W. J., Schrenk, M. O., Kelley, D. S., and Baross, J. A., 2006, Methane- and sulfur-metabolizing microbial communities dominate the Lost City Hydrothermal Field ecosystem: Applied and Environmental Microbiology, v. 72, n. 9, p. 6257–6270, https://doi.org/10.1128/AEM.00574-06

Brazelton, W. J., Mehta, M. P., Kelley, D. S., and Baross, J. A., 2011, Physiological differentiation within a single-species biofilm fueled by serpentinization: mBio, v. 2, n. 4, p. e00127-11, https://doi.org/10.1128/mBio.00127-11

Brazelton, W. J., Nelson, B., and Schrenk, M. O., 2012, Metagenomic evidence for H_2 oxidation and H_2 production by serpentinite-hosted subsurface microbial communities: Frontiers in Microbiology, v. 2, n. 268, https://doi.org/10.3389/fmicb.2011.00268

Brazelton, W. J., Morrill, P. L., Szponar, N., and Schrenk, M. O., 2013, Bacterial communities associated with subsurface geochemical processes in continental serpentinite springs: Applied and Environmental Microbiology, v. 79, n. 13, p. 3906–3916, https://doi.org/10.1128/AEM.00330-13

Brazelton, W. J., Thornton, C. N., Hyer, A., Twing, K. I., Longino, A. A., Lang, S. Q., Lilley, M. D., Früh-Green, G. L., and Schrenk, M. O., 2017, Metagenomic identification of active methanogens and methanotrophs in serpentinite springs of the Voltri Massif, Italy: PeerJ, v. 5, p. e2945, https://doi.org/10.7717/peerj.2945

Bruni, J., Canepa, M., Chiodini, G., Cioni, R., Cipolli, F., Longinelli, A., Marini, L., Ottonello, G., and Vetuschi Zuccolini, M., 2002, Irreversible water–rock mass transfer accompanying the generation of the neutral, Mg–HCO_3 and high-pH, Ca–OH spring waters of the Genova province, Italy: Applied Geochemistry, v. 17, n. 4, p. 455–474, https://doi.org/10.1016/S0883-2927(01)00113-5

Busey, R. H., and Mesmer, R. E., 1977, Ionization equilibriums of silicic acid and polysilicate formation in aqueous sodium chloride solutions to 300 °C: Inorganic Chemistry, v. 16, n. 10, p. 2444–2450, https://doi.org/10.1021/ic50176a004

Canovas, P. A., Hoehler, T., and Shock, E. L., 2017, Geochemical bioenergetics during low-temperature serpentinization: An example from the Samail ophiolite, Sultanate of Oman: Serpentinization Bioenergetics: Journal of Geophysical Research: Biogeosciences, v. 122, n. 7, p. 1821–1847, https://doi.org/10.1002/2017JG003825

Cardace, D., Hoehler, T., McCollom, T., Schrenk, M., Carnevale, D., Kubo, M., and Twing, K., 2013, Establishment of the Coast Range ophiolite microbial observatory (CROMO): Drilling objectives and preliminary outcomes: Scientific Drilling, v. 16, p. 45–55, https://doi.org/10.5194/sd-16-45-2013

Cardace, D., Meyer-Dombard, D. R., Woycheese, K. M., and Arcilla, C. A., 2015, Feasible metabolisms in high pH springs of the Philippines: Frontiers in Microbiology, v. 6, n. 10, https://doi.org/10.3389/fmicb.2015.00010

Charlou, J. L., Donval, J. P., Fouquet, Y., Jean-Baptiste, P., and Holm, N., 2002, Geochemistry of high H_2 and CH_4 vent fluids issuing from ultramafic rocks at the Rainbow hydrothermal field (36°14′N, MAR): Chemical Geology, v. 191, n. 4, p. 345–359, https://doi.org/10.1016/S0009-2541(02)00134-1

Chavagnac, V., Ceuleneer, G., Monnin, C., Lansac, B., Hoareau, G., and Boulart, C., 2013a, Mineralogical assemblages forming at hyperalkaline warm springs hosted on ultramafic rocks: A case study of Oman and Ligurian ophiolites: Geochemistry, Geophysics, Geosystems, v. 14, n. 7, p. 2474–2495, https://doi.org/10.1002/ggge.20146

Chavagnac, V., Monnin, C., Ceuleneer, G., Boulart, C., and Hoareau, G., 2013b, Characterization of hyperalkaline fluids produced by low-temperature serpentinization of mantle peridotites in the Oman and Ligurian ophiolites: Hyperalkaline Waters in Oman and Liguria: Geochemistry, Geophysics, Geosystems, v. 14, n. 7, p. 2496–2522, https://doi.org/10.1002/ggge.20147

Cipolli, F., Gambardella, B., Marini, L., Ottonello, G., and Vetuschi Zuccolini, M., 2004, Geochemistry of high-pH waters from serpentinites of the Gruppo di Voltri (Genova, Italy) and reaction path modeling of CO_2 sequestration in serpentinite aquifers: Applied Geochemistry, v. 19, n. 5, p. 787–802, https://doi.org/10.1016/j.apgeochem.2003.10.007

Crespo-Medina, M., Twing, K. I., Kubo, M. D. Y., Hoehler, T. M., Cardace, D., McCollom, T., and Schrenk, M. O., 2014, Insights into environmental controls on microbial communities in a continental serpentinite aquifer using a microcosm-based approach: Frontiers in Microbiology, v. 5, n. 604, https://doi.org/10.3389/fmicb.2014.00604

Crespo-Medina, M., Twing, K. I., Sánchez-Murillo, R., Brazelton, W. J., McCollom, T. M., and Schrenk, M. O., 2017, Methane dynamics in a tropical serpentinizing environment: The Santa Elena Ophiolite, Costa Rica: Frontiers in Microbiology, v. 8, no. 916, https://doi.org/10.3389/fmicb.2017.00916

Cumming, E. A., Rietze, A., Morrissey, L. S., Cook, M. C., Rhim, J. H., Ono, S., and Morrill, P. L., 2019, Potential sources of dissolved methane at the Tablelands, Gros Morne National Park, NL, CAN: A terrestrial site of serpentinization: Chemical Geology, v. 514, p. 42–53, https://doi.org/10.1016/j.chemgeo.2019.03.019

Daae, F. L., Økland, I., Dahle, H., Jørgensen, S. L., Thorseth, I. H., and Pedersen, R. B., 2013, Microbial life associated with low-temperature alteration of ultramafic rocks in the Leka ophiolite complex: Geobiology, v. 11, n. 4, p. 318–339, https://doi.org/10.1111/gbi.12035

D'Alessandro, W., Daskalopoulou, K., Calabrese, S., and Bellomo, S., 2018, Water chemistry and abiogenic methane content of a hyperalkaline spring related to serpentinization in the Argolida ophiolite (Ermioni, Greece): Marine and Petroleum Geology, v. 89, Part 1, p. 185–193, https://doi.org/10.1016/j.marpetgeo.2017.01.028

Daskalopoulou, K., Calabrese, S., Grassa, F., Kyriakopoulos, K., Parello, F., Tassi, F., and D'Alessandro, W., 2018, Origin of methane and light hydrocarbons in natural fluid emissions: A key study from Greece: Chemical Geology, v. 479, p. 286–301, https://doi.org/10.1016/j.chemgeo.2018.01.027

Daval, D., Hellmann, R., Martinez, I., Gangloff, S., and Guyot, F., 2013, Lizardite serpentine dissolution kinetics as a function of pH and temperature, including effects of elevated pCO_2: Chemical Geology, v. 351, p. 245–256, https://doi.org/10.1016/j.chemgeo.2013.05.020

Dewandel, B., Lachassagne, P., Boudier, F., Al-Hattali, S., Ladouche, B., Pinault, J.-L., and Al-Suleimani, Z., 2005, A conceptual hydrogeological model of ophiolite hard-rock aquifers in Oman based on a multiscale and a multidisciplinary approach: Hydrogeology Journal, v. 13, p. 708–726, https://doi.org/10.1007/s10040-005-0449-2

Douville, E., Charlou, J. L., Oelkers, E. H., Bienvenu, P., Jove Colon, C. F., Donval, J. P., Fouquet, Y., Prieur, D., and Appriou, P., 2002, The rainbow vent fluids (36°14′N, MAR): The influence of ultramafic rocks and phase separation on trace metal content in Mid-Atlantic Ridge hydrothermal fluids: Chemical Geology, v. 184, n. 1–2, p. 37–48, https://doi.org/10.1016/S0009-2541(01)00351-5

Ehlmann, B. L., Mustard, J. F., and Murchie, S. L., 2010, Geologic setting of serpentine deposits on Mars: Geophysical Research Letters, v. 37, n. 6, L0620, https://doi.org/10.1029/2010GL042596

Etiope, G., Schoell, M., and Hosgörmez, H., 2011, Abiotic methane flux from the Chimaera seep and Tekirova ophiolites (Turkey): Understanding gas exhalation from low temperature serpentinization and implications for Mars: Earth and Planetary Science Letters, v. 310, n. 1–2, p. 96–104, https://doi.org/10.1016/j.epsl.2011.08.001

Etiope, G., Tsikouras, B., Kordella, S., Ifandi, E., Christodoulou, D., and Papatheodorou, G., 2013a, Methane flux and origin in the Othrys ophiolite hyperalkaline springs, Greece: Chemical Geology, v. 347, p. 161–174, https://doi.org/10.1016/j.chemgeo.2013.04.003

Etiope, G., Vance, S., Christensen, L. E., Marques, J. M., and Ribeiro da Costa, I., 2013b, Methane in serpentinized ultramafic rocks in mainland Portugal: Marine and Petroleum Geology, v. 45, p. 12–16, https://doi.org/10.1016/j.marpetgeo.2013.04.009

Etiope, G., Judas, J., and Whiticar, M. J., 2015, Occurrence of abiotic methane in the eastern United Arab Emirates ophiolite aquifer: Arabian Journal of Geosciences, v. 8, p. 11345–11348, https://doi.org/10.1007/s12517-015-1975-4

Etiope, G., Vadillo, I., Whiticar, M. J., Marques, J. M., Carreira, P. M., Tiago, I., Benavente, J., Jiménez, P., and Urresti, B., 2016, Abiotic methane seepage in the Ronda peridotite massif, southern Spain: Applied Geochemistry, v. 66, p. 101–113, https://doi.org/10.1016/j.apgeochem.2015.12.001

Etiope, G., Samardžić, N., Grassa, F., Hrvatović, H., Miošić, N., and Skopljak, F., 2017, Methane and hydrogen in hyperalkaline groundwaters of the serpentinized Dinaride ophiolite belt, Bosnia and Herzegovina: Applied Geochemistry, v. 84, p. 286–296, https://doi.org/10.1016/j.apgeochem.2017.07.006

Etiope, G., and Whiticar, M. J., 2019, Abiotic methane in continental ultramafic rock systems: Towards a genetic model: Applied Geochemistry, v. 102, p. 139–152, https://doi.org/10.1016/j.apgeochem.2019.01.012

Evans, B. W., 2004, The serpentinite multisystem revisited: Chrysotile is metastable: International Geology Review, n. 6, v. 46, p. 479–506, https://doi.org/10.2747/0020-6814.46.6.479

——— 2008, Control of the products of serpentinization by the $Fe^{2+}Mg_{-1}$ exchange potential of olivine and orthopyroxene: Journal of Petrology, v. 49, n. 10, p. 1873–1887, https://doi.org/10.1093/petrology/egn050

Evans, B. W., Dyar, M. D., and Kuehner, S. M., 2012, Implications of ferrous and ferric iron in antigorite: American Mineralogist, v. 97, n. 1, p. 184–196, https://doi.org/10.2138/am.2012.3926

Evans, K. A., Powell, R., and Frost, B. R., 2013, Using equilibrium thermodynamics in the study of metasomatic alteration, illustrated by an application to serpentinites: Lithos, v. 168–169, p. 67–84, https://doi.org/10.1016/j.lithos.2013.01.016

Fones, E. M., Colman, D. R., Kraus, E. A., Nothaft, D. B., Poudel, S., Rempfert, K. R., Spear, J. R., Templeton, A. S., and Boyd, E. S., 2019, Physiological adaptations to serpentinization in the Samail Ophiolite, Oman: The ISME Journal, v. 13, p. 1750-1762, https://doi.org/10.1038/s41396-019-0391-2

Foustoukos, D. I., Savov, I. P., and Janecky, D. R., 2008, Chemical and isotopic constraints on water/rock interactions at the Lost City hydrothermal field, 30°N Mid-Atlantic Ridge: Geochimica et Cosmochimica Acta, v. 72, n. 22, p. 5457–5474, https://doi.org/10.1016/j.gca.2008.07.035

Frost, B. R., and Beard, J. S., 2007, On silica activity and serpentinization: Journal of Petrology, v. 48, n. 7, p. 1351–1368, https://doi.org/10.1093/petrology/egm021

Frost, B. R., Evans, K. A., Swapp, S. M., Beard, J. S., and Mothersole, F. E., 2013, The process of serpentinization in dunite from New Caledonia: Lithos, v. 178, p. 24–39, https://doi.org/10.1016/j.lithos.2013.02.002

Früh-Green, G. L., Kelley, D. S., Bernasconi, S. M., Karson, J. A., Ludwig, K. A., Butterfield, D. A., Boschi, C., and Proskurowski, G., 2003, 30,000 years of hydrothermal activity at the Lost City vent field: Science, v. 301, n. 5632, p. 495–498, https://doi.org/10.1126/science.1085582

Früh-Green, G. L., Orcutt, B. N., Rouméjon, S., Lilley, M. D., Morono, Y., Cotterill, C., Green, S., Escartin, J., John, B. E., McCaig, A. M., Cannat, M., Ménez, B., Schwarzenbach, E. M., Williams, M. J., Morgan, S., Lang, S. Q., Schrenk, M. O., Brazelton, W. J., Akizawa, N., Boschi, C., Dunkel, K. G., Quéméneur, M., Whattam, S. A., Mayhew, L., Harris, M., Bayrakci, G., Behrmann, J.-H., Herrero-Bervera, E., Hesse, K., Liu, H.-Q., Ratnayake, A. S., Twing, K., Weis, D., Zhao, R., and Bilenker, L., 2018, Magmatism, serpentinization and life: Insights through drilling the Atlantis Massif (IODP Expedition 357): Lithos, v. 323, p. 137–155, https://doi.org/10.1016/j.lithos.2018.09.012

Fujii, N., Arcilla, C. A., Yamakawa, M., Pascua, C., Namiki, K., Sato, T., Shikazono, N., and Alexander, W. R., 2010, Natural analogue studies of bentonite reaction under hyperalkaline conditions: Overview of

ongoing work at the Zambales Ophiolite, Philippines, *in* ASME 2010 13th International Conference on Environmental Remediation and Radioactive Waste Management – American Society of Mechanical Engineers, p. 41–50, https://doi.org/10.1115/ICEM2010-40022
Gallant, R. M., and Von Damm, K. L. V., 2006, Geochemical controls on hydrothermal fluids from the Kairei and Edmond Vent Fields, 23°–25°S, Central Indian Ridge: Geochemistry, Geophysics, Geosystems, v. 7, n. 6, Q06018, https://doi.org/10.1029/2005GC001067
Giampouras, M., Garrido, C. J., Zwicker, J., Vadillo, I., Smrzka, D., Bach, W., Peckmann, J., Jiménez, P., Benavente, J., and García-Ruiz, J. M., 2019, Geochemistry and mineralogy of serpentinization-driven hyperalkaline springs in the Ronda peridotites: Lithos, v. 350–351, n. 105215, https://doi.org/10.1016/j.lithos.2019.105215
Giampouras, M., Garrido, C. J., Bach, W., Los, C., Fussmann, D., Monien, P., and Garcia-Ruiz, J. M., 2020, On the controls of mineral assemblages and textures in alkaline springs, Samail Ophiolite, Oman: Chemical Geology, v. 533, n. 119435, https://doi.org/10.1016/j.chemgeo.2019.119435
Giggenbach, W. F., Sano, Y., and Wakita, H., 1993, Isotopic composition of helium, and CO_2 and CH_4 contents in gases produced along the New Zealand part of a convergent plate boundary: Geochimica et Cosmochimica Acta, v. 57, n. 14, p. 3427–3455, https://doi.org/10.1016/0016-7037(93)90549-C
Glein, C. R., Baross, J. A., and Waite, J. H., 2015, The pH of Enceladus' ocean: Geochimica et Cosmochimica Acta, v. 162, p. 202–219, https://doi.org/10.1016/j.gca.2015.04.017
Hanghøj, K., Kelemen, P. B., Hassler, D., and Godard, M., 2010, Composition and genesis of depleted mantle peridotites from the Wadi Tayin Massif, Oman Ophiolite; Major and trace element geochemistry, and Os isotope and PGE systematics: Journal of Petrology, v. 51, n. 1–2, p. 201–227, https://doi.org/10.1093/petrology/egp077
Hao, J., Sverjensky, D. A., and Hazen, R. M., 2017, A model for late Archean chemical weathering and world average river water: Earth and Planetary Science Letters, v. 457, p. 191–203, https://doi.org/10.1016/j.epsl.2016.10.021
Helgeson, H. C., Delaney, J. M., Nesbitt, H. W., and Bird, D. K., 1978, Summary and critique of the thermodynamic properties of rock-forming minerals: American Journal of Science, v. 278A, p. 1–229.
Holm, N. G., Dumont, M., Ivarsson, M., and Konn, C., 2006, Alkaline fluid circulation in ultramafic rocks and formation of nucleotide constituents: A hypothesis: Geochemical Transactions, v. 7, n. 7, https://doi.org/10.1186/1467-4866-7-7
Holm, N. G., Oze, C., Mousis, O., Waite, J. H., and Guilbert-Lepoutre, A., 2015, Serpentinization and the formation of H_2 and CH_4 on celestial bodies (planets, moons, comets): Astrobiology, v. 15, n. 7, p. 587–600, https://doi.org/10.1089/ast.2014.1188
Homma, A., and Tsukahara, H., 2008, Chemical characteristics of hot spring water and geological environment in the northernmost area of the Itoigawa Shizuoka tectonic line: Bulletin of the Earthquake Research Institute, University of Tokyo, v. 83, p. 217–225.
Hosgormez, H., Etiope, G., and Yalçin, M. N., 2008, New evidence for a mixed inorganic and organic origin of the Olympic Chimaera fire (Turkey): A large onshore seepage of abiogenic gas: Geofluids, v. 8, n. 4, p. 263–273, https://doi.org/10.1111/j.1468-8123.2008.00226.x
Huang, F., and Sverjensky, D. A., 2019, Extended Deep Earth Water Model for predicting major element mantle metasomatism: Geochimica et Cosmochimica Acta, v. 254, p. 192–230, https://doi.org/10.1016/j.gca.2019.03.027
Itävaara, M., Nyyssönen, M., Kapanen, A., Nousiainen, A., Ahonen, L., and Kukkonen, I., 2011, Characterization of bacterial diversity to a depth of 1500 m in the Outokumpu deep borehole, Fennoscandian Shield: FEMS Microbiology Ecology, v. 77, n. 2, p. 295–309, https://doi.org/10.1111/j.1574-6941.2011.01111.x
Janecky, D. R., and Seyfried Jr., W. E., 1986, Hydrothermal serpentinization of peridotite within the oceanic crust: Experimental investigations of mineralogy and major element chemistry: Geochimica et Cosmochimica Acta, v. 50, n. 7, p. 1357–1378, https://doi.org/10.1016/0016-7037(86)90311-X
Johnson, J. W., Oelkers, E. H., and Helgeson, H. C., 1992, SUPCRT92: A software package for calculating the standard molal thermodynamic properties of minerals, gases, aqueous species, and reactions from 1 to 5000 bar and 0 to 1000 °C: Computers & Geosciences, v. 18, n. 7, p. 899–947, https://doi.org/10.1016/0098-3004(92)90029-Q
Kelemen, P., Al Rajhi, A., Godard, M., Ildefonse, B., Köpke, J., MacLeod, C., Manning, C., Michibayashi, K., Nasir, S., Shock, E., Takazawa, E., and Teagle, D., 2013, Scientific drilling and related research in the Samail Ophiolite, Sultanate of Oman: Scientific Drilling, v. 15, p. 64–71, https://doi.org/10.5194/sd-15-64-2013
Kelemen, P. B., and Matter, J., 2008, *In situ* carbonation of peridotite for CO_2 storage: Proceedings of the National Academy of Sciences of the United States of America, v. 105, n. 45, p. 17295–17300, https://doi.org/10.1073/pnas.0805794105
Kelley, D. S., Karson, J. A., Blackman, D. K., Früh-Green, G. L., Butterfield, D. A., Lilley, M. D., Olson, E. J., Schrenk, M. O., Roe, K. K., Lebon, G. T., Rivizzigno, P., and the AT3-60 Shipboard Party, 2001, An off-axis hydrothermal vent field near the Mid-Atlantic Ridge at 30° N: Nature, v. 412, p. 145–149, https://doi.org/10.1038/35084000
Kelley, D. S., Karson, J. A., Früh-Green, G. L., Yoerger, D. R., Shank, T. M., Butterfield, D. A., Hayes, J. M., Schrenk, M. O., Olson, E. J., Proskurowski, G., Jakuba, M., Bradley, A., Larson, B., Ludwig, K., Glickson, D., Buckman, K., Bradley, A. S., Brazelton, W. J., Roe, K., Elend, M. J., Delacour, A., Bernasconi, S. M., Lilley, M. D., Baross, J. A., Summons, R. E., and Sylva, S. P., 2005, A serpentinite-hosted ecosystem: The Lost City Hydrothermal Field: Science, v. 307, n. 5714, p. 1428–1434, https://doi.org/10.1126/science.1102556
Khoury, H. N., Salameh, E., and Abdul-Jaber, Q., 1985, Characteristics of an unusual highly alkaline water

from the Maqarin area, northern Jordan: Journal of Hydrology, v. 81, n. 1–2, p. 79–91, https://doi.org/10.1016/0022-1694(85)90168-4

Khoury, H. N., Salameh, E., Clark, I. D., Fritz, P., Bajjali, W., Milodowski, A. E., Cave, M. R., and Alexander, W. R., 1992, A natural analogue of high pH cement pore waters from the Maqarin area of northern Jordan. I: Introduction to the site: Journal of Geochemical Exploration, v. 46, n. 1, p. 117–132, https://doi.org/10.1016/0375-6742(92)90103-F

Klein, F., Bach, W., Jöns, N., McCollom, T., Moskowitz, B., and Berquó, T., 2009, Iron partitioning and hydrogen generation during serpentinization of abyssal peridotites from 15°N on the Mid-Atlantic Ridge: Geochimica et Cosmochimica Acta, v. 73, n. 22, p. 6868–6893, https://doi.org/10.1016/j.gca.2009.08.021

Klein, F., Bach, W., and McCollom, T. M., 2013, Compositional controls on hydrogen generation during serpentinization of ultramafic rocks: Lithos, v. 178, p. 55–69, https://doi.org/10.1016/j.lithos.2013.03.008

Klein, F., Bach, W., Humphris, S. E., Kahl, W.-A., Jöns, N., Moskowitz, B., and Berquó, T. S., 2014, Magnetite in seafloor serpentinite - Some like it hot: Geology, v. 42, n. 2, p. 135–138, https://doi.org/10.1130/G35068.1

Kodolányi, J., Pettke, T., Spandler, C., Kamber, B. S., and Gméling, K., 2012, Geochemistry of ocean floor and fore-arc serpentinites: Constraints on the ultramafic input to subduction zones: Journal of Petrology, v. 53, n. 2, p. 235–270, https://doi.org/10.1093/petrology/egr058

Kohl, L., Cumming, E., Cox, A., Rietze, A., Morrissey, L., Lang, S. Q., Richter, A., Suzuki, S., Nealson, K. H., and Morrill, P. L., 2016, Exploring the metabolic potential of microbial communities in ultra-basic, reducing springs at The Cedars, CA, USA: Experimental evidence of microbial methanogenesis and heterotrophic acetogenesis: Journal of Geophysical Research: Biogeosciences, v. 121, n. 4, p. 1203–1220, https://doi.org/10.1002/2015JG003233

Kumagai, H., Nakamura, K., Toki, T., Morishita, T., Okino, K., Ishibashi, J., Tsunogai, U., Kawagucci, S., Gamo, T., Shibuya, T., Sawaguchi, T., Neo, N., Joshima, M., Sato, T., and Takai, K., 2008, Geological background of the Kairei and Edmond hydrothermal fields along the Central Indian Ridge: Implications of their vent fluids' distinct chemistry: Geofluids, v. 8, n. 4, p. 239–251, https://doi.org/10.1111/j.1468-8123.2008.00223.x

Lane, N., and Martin, W. F., 2012, The origin of membrane bioenergetics: Cell, v. 151, n. 7, p. 1406–1416, https://doi.org/10.1016/j.cell.2012.11.050

Lang, S. Q., Butterfield, D. A., Schulte, M., Kelley, D. S., and Lilley, M. D., 2010, Elevated concentrations of formate, acetate and dissolved organic carbon found at the Lost City hydrothermal field: Geochimica et Cosmochimica Acta, v. 74, n. 3, p. 941–952, https://doi.org/10.1016/j.gca.2009.10.045

Marques, J. M., Carreira, P. M., Carvalho, M. R., Matias, M. J., Goff, F. E., Basto, M. J., Graça, R. C., Aires-Barros, L., and Rocha, L., 2008, Origins of high pH mineral waters from ultramafic rocks, Central Portugal: Applied Geochemistry, v. 23, n. 12, p. 3278–3289, https://doi.org/10.1016/j.apgeochem.2008.06.029

Marques, J. M., Etiope, G., Neves, M. O., Carreira, P. M., Rocha, C., Vance, S. D., Christensen, L., Miller, A. Z., and Suzuki, S., 2018, Linking serpentinization, hyperalkaline mineral waters and abiotic methane production in continental peridotites: An integrated hydrogeological-bio-geochemical model from the Cabeço de Vide CH_4-rich aquifer (Portugal): Applied Geochemistry, v. 96, p. 287–301, https://doi.org/10.1016/j.apgeochem.2018.07.011

Marshall, W. L., and Warakomski, J. M., 1980, Amorphous silica solubilities—II. Effect of aqueous salt solutions at 25 °C: Geochimica et Cosmochimica Acta, v. 44, n. 7, p. 915–924, https://doi.org/10.1016/0016-7037(80)90281-1

Martin, W., and Russell, M. J., 2007, On the origin of biochemistry at an alkaline hydrothermal vent: Philosophical Transactions of the Royal Society B: Biological Sciences, v. 362, p. 1887–1926, https://doi.org/10.1098/rstb.2006.1881

Martin, W., Baross, J., Kelley, D., and Russell, M. J., 2008, Hydrothermal vents and the origin of life: Nature Reviews Microbiology, v. 6, p. 805–814, https://doi.org/10.1038/nrmicro1991

Martin, W. F., Sousa, F. L., and Lane, N., 2014, Energy at life's origin: Science, v. 344, n. 6188, p. 1092–1093, https://doi.org/10.1126/science.1251653

Matter, J. M., Waber, H. N., Loew, S., and Matter, A., 2006, Recharge areas and geochemical evolution of groundwater in an alluvial aquifer system in the Sultanate of Oman: Hydrogeology Journal, v. 14, p. 203–224, https://doi.org/10.1007/s10040-004-0425-2

Mayhew, L. E., Ellison, E. T., Miller, H. M., Kelemen, P. B., and Templeton, A. S., 2018, Iron transformations during low temperature alteration of variably serpentinized rocks from the Samail ophiolite, Oman: Geochimica et Cosmochimica Acta, v. 222, p. 704–728, https://doi.org/10.1016/j.gca.2017.11.023

McCollom, T. M., 2007, Geochemical constraints on sources of metabolic energy for chemolithoautotrophy in ultramafic-hosted deep-sea hydrothermal systems: Astrobiology, v. 7, n. 6, p. 933–950, https://doi.org/10.1089/ast.2006.0119

——— 2016, Abiotic methane formation during experimental serpentinization of olivine: Proceedings of the National Academy of Sciences of the United States of America, v. 113, n. 49, p. 13965–13970, https://doi.org/10.1073/pnas.1611843113

McCollom, T. M., and Bach, W., 2009, Thermodynamic constraints on hydrogen generation during serpentinization of ultramafic rocks: Geochimica et Cosmochimica Acta, v. 73, n. 3, p. 856–875, https://doi.org/10.1016/j.gca.2008.10.032

McCollom, T. M., and Seewald, J. S., 2007, Abiotic synthesis of organic compounds in deep-sea hydrothermal environments: Chemical Reviews, v. 107, n. 2, p. 382–401, https://doi.org/10.1021/cr0503660

McCollom, T. M., and Shock, E. L., 1997, Geochemical constraints on chemolithoautotrophic metabolism by

microorganisms in seafloor hydrothermal systems: Geochimica et Cosmochimica Acta, v. 61, n. 20, p. 4375–4391, https://doi.org/10.1016/S0016-7037(97)00241-X
——— 1998, Fluid-rock interactions in the lower oceanic crust: Thermodynamic models of hydrothermal alteration: Journal of Geophysical Research: Solid Earth, v. 103, p. 547–575, https://doi.org/10.1029/97JB02603
McDermott, J. M., Seewald, J. S., German, C. R., and Sylva, S. P., 2015, Pathways for abiotic organic synthesis at submarine hydrothermal fields: Proceedings of the National Academy of Sciences of the United States of America, v. 112, n. 25, p. 7668–7672, https://doi.org/10.1073/pnas.1506295112
Ménez, B., Pasini, V., and Brunelli, D., 2012, Life in the hydrated suboceanic mantle: Nature Geoscience, v. 5, p. 133–137, https://doi.org/10.1038/ngeo1359
Ménez, B., Pasini, V., Guyot, F., Benzerara, K., Bernard, S., and Brunelli, D., 2018, Mineralizations and transition metal mobility driven by organic carbon during low-temperature serpentinization: Lithos, v. 323, p. 262–276, https://doi.org/10.1016/j.lithos.2018.07.022
Mervine, E. M., Humphris, S. E., Sims, K. W. W., Kelemen, P. B., and Jenkins, W. J., 2014, Carbonation rates of peridotite in the Samail Ophiolite, Sultanate of Oman, constrained through ^{14}C dating and stable isotopes: Geochimica et Cosmochimica Acta, v. 126, p. 371–397, https://doi.org/10.1016/j.gca.2013.11.007
Meyer-Dombard, D. R., Woycheese, K. M., Yargıçoğlu, E. N., Cardace, D., Shock, E. L., Güleçal-Pektas, Y., and Temel, M., 2015, High pH microbial ecosystems in a newly discovered, ephemeral, serpentinizing fluid seep at Yanartaş (Chimera), Turkey: Frontiers in Microbiology, v. 5, n. 723, https://doi.org/10.3389/fmicb.2014.00723
Meyer-Dombard, D. R., Casar, C. P., Simon, A. G., Cardace, D., Schrenk, M. O., and Arcilla, C. A., 2018, Biofilm formation and potential for iron cycling in serpentinization-influenced groundwater of the Zambales and Coast Range ophiolites: Extremophiles, v. 22, p. 407–431, https://doi.org/10.1007/s00792-018-1005-z
Meyer-Dombard, D. R., Osburn, M. R., Cardace, D., and Arcilla, C. A., 2019, The effect of a tropical climate on available nutrient resources to springs in ophiolite-hosted, deep biosphere ecosystems in the Philippines: Frontiers in Microbiology, v. 10, n. 761, https://doi.org/10.3389/fmicb.2019.00761
Miller, H. M., Matter, J. M., Kelemen, P., Ellison, E. T., Conrad, M. E., Fierer, N., Ruchala, T., Tominaga, M., and Templeton, A. S., 2016, Modern water/rock reactions in Oman hyperalkaline peridotite aquifers and implications for microbial habitability: Geochimica et Cosmochimica Acta, v. 179, p. 217–241, https://doi.org/10.1016/j.gca.2016.01.033
Monnin, C., Chavagnac, V., Boulart, C., Ménez, B., Gérard, M., Gérard, E., Pisapia, C., Quéméneur, M., Erauso, G., Postec, A., Guentas-Dombrowski, L., Payri, C., and Pelletier, B., 2014, Fluid chemistry of the low temperature hyperalkaline hydrothermal system of Prony Bay (New Caledonia): Biogeosciences, v. 11, n. 20, p. 5687–5706, https://doi.org/10.5194/bg-11-5687-2014
Morrill, P. L., Kuenen, J. G., Johnson, O. J., Suzuki, S., Rietze, A., Sessions, A. L., Fogel, M. L., and Nealson, K. H., 2013, Geochemistry and geobiology of a present-day serpentinization site in California: The Cedars: Geochimica et Cosmochimica Acta, v. 109, p. 222–240, https://doi.org/10.1016/j.gca.2013.01.043
Morrill, P. L., Brazelton, W. J., Kohl, L., Rietze, A., Miles, S. M., Kavanagh, H., Schrenk, M. O., Ziegler, S. E., and Lang, S. Q., 2014, Investigations of potential microbial methanogenic and carbon monoxide utilization pathways in ultra-basic reducing springs associated with present-day continental serpentinization: The Tablelands, NL, CAN: Frontiers in Microbiology, v. 5, n. 613, https://doi.org/10.3389/fmicb.2014.00613
Mottl, M. J., 2009, Highest pH: Geochemical News, v. 141, n. 9.
Mottl, M. J., Komor, S. C., Fryer, P., and Moyer, C. L., 2003, Deep-slab fluids fuel extremophilic *Archaea* on a Mariana forearc serpentinite mud volcano: Ocean Drilling Program Leg 195: Geochemistry, Geophysics, Geosystems, v. 4, n. 11, 9009, https://doi.org/10.1029/2003GC000588
Mottl, M. J., Wheat, C. G., Fryer, P., Gharib, J., and Martin, J. B., 2004, Chemistry of springs across the Mariana forearc shows progressive devolatilization of the subducting plate: Geochimica et Cosmochimica Acta, v. 68, n. 23, p. 4915–4933, https://doi.org/10.1016/j.gca.2004.05.037
Nakamura, K., and Takai, K., 2014, Theoretical constraints of physical and chemical properties of hydrothermal fluids on variations in chemolithotrophic microbial communities in seafloor hydrothermal systems: Progress in Earth and Planetary Science, v. 1, 5, https://doi.org/10.1186/2197-4284-1-5
Neal, C., and Shand, P., 2002, Spring and surface water quality of the Cyprus ophiolites: Hydrology and Earth System Sciences, v. 6, n. 5, p. 797–817, https://doi.org/10.5194/hess-6-797-2002
Neal, C., and Stanger, G., 1983, Hydrogen generation from mantle source rocks in Oman: Earth and Planetary Science Letters, v. 66, p. 315–320, https://doi.org/10.1016/0012-821X(83)90144-9
——— 1984, Calcium and magnesium hydroxide precipitation from alkaline groundwaters in Oman, and their significance to the process of serpentinization: Mineralogical Magazine, v. 48, n. 347, p. 237–241, https://doi.org/10.1180/minmag.1984.048.347.07
——— 1985, Past and present serpentinisation of ultramafic rocks; An example from the Semail Ophiolite Nappe of Northern Oman, *in* Drever, J. I., editor, The Chemistry of Weathering: Springer, NATO ASI Series, v. 149, p. 249–275, https://doi.org/10.1007/978-94-009-5333-8_15
Neubeck, A., Sun, L., Müller, B., Ivarsson, M., Hosgörmez, H., Özcan, D., Broman, C., and Schnürer, A., 2017, Microbial community structure in a serpentine-hosted abiotic gas seepage at the Chimaera ophiolite, Turkey: Applied and Environmental Microbiology, v. 83, n. 12, e03430-16, https://doi.org/10.1128/AEM.03430-16
Newton, R. C., and Manning, C. E., 2010, Role of saline fluids in deep-crustal and upper-mantle metasomatism: Insights from experimental studies: Geofluids, v. 10, n. 1–2, p. 58–72, https://doi.org/10.1111/j.1468-8123.2009.00275.x

Nyyssönen, M., Hultman, J., Ahonen, L., Kukkonen, I., Paulin, L., Laine, P., Itävaara, M., and Auvinen, P., 2014, Taxonomically and functionally diverse microbial communities in deep crystalline rocks of the Fennoscandian shield: The ISME Journal, v. 8, p. 126–138, https://doi.org/10.1038/ismej.2013.125

O'Hanley, D. S., and Dyar, M. D., 1993, The composition of lizardite 1T and the formation of magnetite in serpentinites: American Mineralogist, v. 78, n. 3–4, p. 391–404.

——— 1998, The composition of chrysotile and its relationship with lizardite: The Canadian Mineralogist, v. 36, n. 3, p. 727–739.

Oelkers, E. H., 2001, An experimental study of forsterite dissolution rates as a function of temperature and aqueous Mg and Si concentrations: Chemical Geology, v. 175, n. 3–4, p. 485–494, https://doi.org/10.1016/S0009-2541(00)00352-1

Ohlsson, J. I., Osvatic, J. T., Becraft, E. D., and Swingley, W. D., 2019, Microbial community in hyperalkaline steel slag-fill emulates serpentinizing springs: Diversity, v. 11, n. 7, 103, https://doi.org/10.3390/d11070103

Okland, I., Huang, S., Dahle, H., Thorseth, I. H., and Pedersen, R. B., 2012, Low temperature alteration of serpentinized ultramafic rock and implications for microbial life: Chemical Geology, v. 318–319, p. 75–87, https://doi.org/10.1016/j.chemgeo.2012.05.015

Olsson, J., Stipp, S. L. S., and Gislason, S. R., 2014, Element scavenging by recently formed travertine deposits in the alkaline springs from the Oman Semail Ophiolite: Mineralogical Magazine, v. 78, n. 6, p. 1479–1490, https://doi.org/10.1180/minmag.2014.078.6.15

Oufi, O., Cannat, M., and Horen, H., 2002, Magnetic properties of variably serpentinized abyssal peridotites: Journal of Geophysical Research: Solid Earth, v. 107, n. N5, EPM-3, https://doi.org/10.1029/2001JB000549

Palandri, J. L., and Reed, M. H., 2004, Geochemical models of metasomatism in ultramafic systems: Serpentinization, rodingitization, and sea floor carbonate chimney precipitation: Geochimica et Cosmochimica Acta, v. 68, n. 5, p. 1115–1133, https://doi.org/10.1016/j.gca.2003.08.006

Papastamataki, A., 1977, The alkalinity and the chemical composition of springs issuing from peridotites: Annales Géologiques Des Pays Helléniques, v. 28, p. 551–566.

Paukert, A. N., Matter, J. M., Kelemen, P. B., Shock, E. L., and Havig, J. R., 2012, Reaction path modeling of enhanced *in situ* CO_2 mineralization for carbon sequestration in the peridotite of the Samail Ophiolite, Sultanate of Oman: Chemical Geology, v. 330–331, p. 86–100, https://doi.org/10.1016/j.chemgeo.2012.08.013

Paukert Vankeuren, A. N., Matter, J. M., Stute, M., and Kelemen, P. B., 2019, Multitracer determination of apparent groundwater ages in peridotite aquifers within the Samail ophiolite, Sultanate of Oman: Earth and Planetary Science Letters, v. 516, p. 37–48, https://doi.org/10.1016/j.epsl.2019.03.007

Pawson, J. F., Oze, C., Etiope, G., and Horton, T. W., 2014, Discovery of new methane-bearing hyperalkaline springs in the serpentinized Dun Mountain Ophiolite, New Zealand: AGU Fall Meeting Abstracts, p. V53A-4824.

Pedersen, K., Nilsson, E., Arlinger, J., Hallbeck, L., and O'Neill, A., 2004, Distribution, diversity and activity of microorganisms in the hyper-alkaline spring waters of Maqarin in Jordan: Extremophiles, v. 8, p. 151–164, https://doi.org/10.1007/s00792-004-0374-7

Pfeifer, H.-R., 1977, A model for fluids in metamorphosed ultramafic rocks: observations at surface and subsurface conditions (high pH spring waters): Schweizerische Mineralogische und Petrographische Mitteilungen, v. 57, p. 361–396.

Plümper, O., Beinlich, A., Bach, W., Janots, E., and Austrheim, H., 2014, Garnets within geode-like serpentinite veins: Implications for element transport, hydrogen production and life-supporting environment formation: Geochimica et Cosmochimica Acta, v. 141, p. 454–471, https://doi.org/10.1016/j.gca.2014.07.002

Pokrovsky, O. S., and Schott, J., 2000, Kinetics and mechanism of forsterite dissolution at 25 °C and pH from 1 to 12: Geochimica et Cosmochimica Acta, v. 64, n. 19, p. 3313–3325, https://doi.org/10.1016/S0016-7037(00)00434-8

Postec, A., Quéméneur, M., Bes, M., Mei, N., Benaïssa, F., Payri, C., Monnin, C., Pelletier, B., Guentas, L., Ollivier, B., Gérard, E., Pisapia, C., Gérard, M., Ménez, B., and Erauso, G., 2015, Microbial diversity in a submarine carbonate edifice from the serpentinizing hydrothermal system of the Prony Bay (New Caledonia) over a 6-year period: Frontiers in Microbiology, v. 6, article n. 867, https://doi.org/10.3389/fmicb.2015.00857

Quéméneur, M., Bes, M., Postec, A., Mei, N., Hamelin, J., Monnin, C., Chavagnac, V., Payri, C., Pelletier, B., Guentas-Dombrowsky, L., Gérard, M., Pisapia, C., Gérard, E., Ménez, B., Ollivier, B., and Erauso, G., 2014, Spatial distribution of microbial communities in the shallow submarine alkaline hydrothermal field of the Prony Bay, New Caledonia: Environmental Microbiology Reports, v. 6, n. 6, p. 665–674, https://doi.org/10.1111/1758-2229.12184

Quéméneur, M., Palvadeau, A., Postec, A., Monnin, C., Chavagnac, V., Ollivier, B., and Erauso, G., 2015, Endolithic microbial communities in carbonate precipitates from serpentinite-hosted hyperalkaline springs of the Voltri Massif (Ligurian Alps, Northern Italy): Environmental Science and Pollution Research, v. 22, p. 13613–13624, https://doi.org/10.1007/s11356-015-4113-7

Reardon, E. J., 1990, An ion interaction model for the determination of chemical equilibria in cement/water systems: Cement and Concrete Research, v. 20, n. 2, p. 175–192, https://doi.org/10.1016/0008-8846(90)90070-E

Rempfert, K. R., Miller, H. M., Bompard, N., Nothaft, D., Matter, J. M., Kelemen, P., Fierer, N., and Templeton, A. S., 2017, Geological and geochemical controls on subsurface microbial life in the Samail Ophiolite, Oman: Frontiers in Microbiology, v. 8, n. 56, https://doi.org/10.3389/fmicb.2017.00056

Rizoulis, A., Milodowski, A. E., Morris, K., and Lloyd, J. R., 2016, Bacterial diversity in the hyperalkaline Allas

Springs (Cyprus), a natural analogue for cementitious radioactive waste repository: Geomicrobiology Journal, v. 33, n. 2, . 73–84, https://doi.org/10.1080/01490451.2014.961107
Roadcap, G. S., Kelly, W. R., and Bethke, C. M., 2005, Geochemistry of extremely alkaline (pH > 12) ground water in slag-fill aquifers: Groundwater, v. 43, n. 6, p. 806–816, https://doi.org/10.1111/j.1745-6584.2005.00060.x
Roadcap, G. S., Sanford, R. A., Jin, Q., Pardinas, J. R., and Bethke, C. M., 2006, Extremely alkaline (pH > 12) ground water hosts diverse microbial community: Groundwater, v. 44, n. 4, p. 511–517, https://doi.org/10.1111/j.1745-6584.2006.00199.x
Russell, M. J., Hall, A. J., and Martin, W., 2010, Serpentinization as a source of energy at the origin of life: Geobiology, v. 8, n. 5, p. 355–371, https://doi.org/10.1111/j.1472-4669.2010.00249.x
Sader, J. A., Leybourne, M. I., McClenaghan, M. B., and Hamilton, S. M., 2007, Low-temperature serpentinization processes and kimberlite groundwater signatures in the Kirkland Lake and Lake Timiskiming kimberlite fields, Ontario, Canada: Implications for diamond exploration: Geochemistry: Exploration, Environment, Analysis, v. 7, p. 3–21, https://doi.org/10.1144/1467-7873/06-900
Sánchez-Murillo, R., Gazel, E., Schwarzenbach, E. M., Crespo-Medina, M., Schrenk, M. O., Boll, J., and Gill, B. C., 2014, Geochemical evidence for active tropical serpentinization in the Santa Elena Ophiolite, Costa Rica: An analog of a humid early Earth?: Geochemistry, Geophysics, Geosystems, v. 15, n. 5, p. 1783–1800, https://doi.org/10.1002/2013GC005213
Sano, Y., Urabe, A., Wakita, H., and Wushiki, H., 1993, Origin of hydrogen-nitrogen gas seeps, Oman: Applied Geochemistry, v. 8, n. 3, p. 1–8, https://doi.org/10.1016/0883-2927(93)90053-J
Schmidt, K., Koschinsky, A., Garbe-Schönberg, D., de Carvalho, L. M., and Seifert, R., 2007, Geochemistry of hydrothermal fluids from the ultramafic-hosted Logatchev hydrothermal field, 15°N on the Mid-Atlantic Ridge: Temporal and spatial investigation: Chemical Geology, v. 242, n. 1–2, p. 1–21, https://doi.org/10.1016/j.chemgeo.2007.01.023
Schrenk, M. O., Kelley, D. S., Bolton, S. A., and Baross, J. A., 2004, Low archaeal diversity linked to subseafloor geochemical processes at the Lost City Hydrothermal Field, Mid-Atlantic Ridge: Environmental Microbiology, v. 6, n. 10, p. 1086–1095, https://doi.org/10.1111/j.1462-2920.2004.00650.x
Schrenk, M. O., Brazelton, W. J., and Lang, S. Q., 2013, Serpentinization, carbon, and deep life: Reviews in Mineralogy and Geochemistry, v. 75, p. 575–606, https://doi.org/10.2138/rmg.2013.75.18
Schulte, M., Blake, D., Hoehler, T., and McCollom, T., 2006, Serpentinization and Its implications for life on the early Earth and Mars: Astrobiology, v. 6, n. 2, p. 364–376, https://doi.org/10.1089/ast.2006.6.364
Schwarzenbach, E. M., Lang, S. Q., Früh-Green, G. L., Lilley, M. D., Bernasconi, S. M., and Méhay, S., 2013, Sources and cycling of carbon in continental, serpentinite-hosted alkaline springs in the Voltri Massif, Italy: Lithos, v. 177, p. 226–244, https://doi.org/10.1016/j.lithos.2013.07.009
Sciarra, A., Saroni, A., Etiope, G., Coltorti, M., Mazzarini, F., Lott, C., Grassa, F., and Italiano, F., 2019, Shallow submarine seep of abiotic methane from serpentinized peridotite off the Island of Elba, Italy: Applied Geochemistry, v. 100, p. 1–7, https://doi.org/10.1016/j.apgeochem.2018.10.025
Segadelli, S., Vescovi, P., Ogata, K., Chelli, A., Zanini, A., Boschetti, T., Petrella, E., Toscani, L., Gargini, A., and Celico, F., 2017, A conceptual hydrogeological model of ophiolitic aquifers (serpentinised peridotite): The test example of Mt. Prinzera (Northern Italy): Hydrological Processes, v. 31, n. 5, p. 1058–1073, https://doi.org/10.1002/hyp.11090
Seward, T. M., 1974, Determination of the first ionization constant of silicic acid from quartz solubility in borate buffer solutions to 350 °C: Geochimica et Cosmochimica Acta, v. 38, n. 11, p. 1651–1664, https://doi.org/10.1016/0016-7037(74)90183-5
Seyfried, W. E., Foustoukos, D. I., and Fu, Q., 2007, Redox evolution and mass transfer during serpentinization: An experimental and theoretical study at 200 °C, 500 bar with implications for ultramafic-hosted hydrothermal systems at Mid-Ocean Ridges: Geochimica et Cosmochimica Acta, v. 71, n. 15, p. 3872–3886, https://doi.org/10.1016/j.gca.2007.05.015
Seyfried Jr., W. E., Pester, N. J., Tutolo, B. M., and Ding, K., 2015, The Lost City hydrothermal system: Constraints imposed by vent fluid chemistry and reaction path models on subseafloor heat and mass transfer processes: Geochimica et Cosmochimica Acta, v. 163, p. 59–79, https://doi.org/10.1016/j.gca.2015.04.040
Sherwood Lollar, B., Voglesonger, K., Lin, L.-H., Lacrampe-Couloume, G., Telling, J., Abrajano, T. A., Onstott, T. C., and Pratt, L. M., 2007, Hydrogeologic controls on episodic H_2 release from precambrian fractured rocks—Energy for deep subsurface life on Earth and Mars: Astrobiology, v. 7, n. 6, p. 971–986, https://doi.org/10.1089/ast.2006.0096
Sherwood Lollar, B., Onstott, T. C., Lacrampe-Couloume, G., and Ballentine, C. J., 2014, The contribution of the Precambrian continental lithosphere to global H_2 production: Nature, v. 516, p. 379–382, https://doi.org/10.1038/nature14017
Shimbashi, M., Sato, T., Yamakawa, M., Fujii, N., and Otake, T., 2018, Formation of Fe- and Mg-rich smectite under hyperalkaline conditions at Narra in Palawan, the Philippines: Minerals, v. 8, n. 4, 155, https://doi.org/10.3390/min8040155
Shock, E. L., and Helgeson, H. C., 1988, Calculation of the thermodynamic and transport properties of aqueous species at high pressures and temperatures: Correlation algorithms for ionic species and equation of state predictions to 5 kb and 1000 °C: Geochimica et Cosmochimica Acta, v. 52, n. 8, p. 2009–2036, https://doi.org/10.1016/0016-7037(88)90181-0
Shock, E. L., Helgeson, H. C., and Sverjensky, D. A., 1989, Calculation of the thermodynamic and transport properties of aqueous species at high pressures and temperatures: Standard partial molal properties of inorganic neutral species: Geochimica et Cosmochimica Acta, v. 53, n. 9, p. 2157–2183, https://doi.org/10.1016/0016-7037(89)90341-4
Shock, E. L., Oelkers, E. H., Johnson, J. W., Sverjensky, D. A., and Helgeson, H. C., 1992, Calculation of the thermodynamic properties of aqueous species at high pressures and temperatures. Effective

electrostatic radii, dissociation constants and standard partial molal properties to 1000 °C and 5 kbar: Journal of the Chemical Society, Faraday Transactions, v. 88, p. 803–826, https://doi.org/10.1039/FT9928800803

Shock, E. L., Sassani, D. C., Willis, M., and Sverjensky, D. A., 1997, Inorganic species in geologic fluids: Correlations among standard molal thermodynamic properties of aqueous ions and hydroxide complexes: Geochimica et Cosmochimica Acta, v. 61, n. 5, p. 907–950, https://doi.org/10.1016/S0016-7037(96)00339-0

Shock, E. L., Holland, M., Meyer-Dombard, D., Amend, J. P., Osburn, G. R., and Fischer, T. P., 2010, Quantifying inorganic sources of geochemical energy in hydrothermal ecosystems, Yellowstone National Park, USA: Geochimica et Cosmochimica Acta, v. 74, n. 14, p. 4005–4043, https://doi.org/10.1016/j.gca.2009.08.036

Sleep, N. H., Meibom, A., Fridriksson, T., Coleman, R. G., and Bird, D. K., 2004, H_2-rich fluids from serpentinization: Geochemical and biotic implications: Proceedings of the National Academy of Sciences of the United States of America, v. 101, n. 35, p. 12818–12823, https://doi.org/10.1073/pnas.0405289101

Sleep, N. H., Bird, D. K., and Pope, E. C., 2011, Serpentinite and the dawn of life: Philosophical Transactions of the Royal Society B: Biological Sciences, v. 366, n. 1580, p. 2857–2869, https://doi.org/10.1098/rstb.2011.0129

Suda, K., Ueno, Y., Yoshizaki, M., Nakamura, H., Kurokawa, K., Nishiyama, E., Yoshino, K., Hongoh, Y., Kawachi, K., Omori, S., Yamada, K., Yoshida, N., and Maruyama, S., 2014, Origin of methane in serpentinite-hosted hydrothermal systems: The CH_4–H_2–H_2O hydrogen isotope systematics of the Hakuba Happo hot spring: Earth and Planetary Science Letters, v. 386, p. 112–125, https://doi.org/10.1016/j.epsl.2013.11.001

Suda, K., Gilbert, A., Yamada, K., Yoshida, N., and Ueno, Y., 2017, Compound– and position–specific carbon isotopic signatures of abiogenic hydrocarbons from on–land serpentinite–hosted Hakuba Happo hot spring in Japan: Geochimica et Cosmochimica Acta, v. 206, p. 201–215, https://doi.org/10.1016/j.gca.2017.03.008

Suzuki, S., Ishii, S., Wu, A., Cheung, A., Tenney, A., Wanger, G., Kuenen, J. G., and Nealson, K. H., 2013, Microbial diversity in The Cedars, an ultrabasic, ultrareducing, and low salinity serpentinizing ecosystem: Proceedings of the National Academy of Sciences of the United States of America, v. 110, n. 38, p. 15336–15341, https://doi.org/10.1073/pnas.1302426110

Suzuki, S., Kuenen, J. G., Schipper, K., van der Velde, S., Ishii, S., Wu, A., Sorokin, D. Y., Tenney, A., Meng, X., Morrill, P. L., Kamagata, Y., Muyzer, G., and Nealson, K. H., 2014, Physiological and genomic features of highly alkaliphilic hydrogen-utilizing *Betaproteobacteria* from a continental serpentinizing site: Nature Communications, v. 5, article n. 3900, https://doi.org/10.1038/ncomms4900

Suzuki, S., Ishii, S., Hoshino, T., Rietze, A., Tenney, A., Morrill, P. L., Inagaki, F., Kuenen, J. G., and Nealson, K. H., 2017, Unusual metabolic diversity of hyperalkaliphilic microbial communities associated with subterranean serpentinization at The Cedars: The ISME Journal, v. 11, p. 2584–2598, https://doi.org/10.1038/ismej.2017.111

Sverjensky, D. A., 1985, The distribution of divalent trace elements between sulfides, oxides, silicates and hydrothermal solutions: I. Thermodynamic basis: Geochimica et Cosmochimica Acta, v. 49, n. 3, p. 853–864, https://doi.org/10.1016/0016-7037(85)90177-2

Sverjensky, D. A., and Molling, P. A., 1992, A linear free energy relationship for crystalline solids and aqueous ions: Nature, v. 356, p. 231–234, https://doi.org/10.1038/356231a0

Sverjensky, D. A., Shock, E. L., and Helgeson, H. C., 1997, Prediction of the thermodynamic properties of aqueous metal complexes to 1000 °C and 5 kb: Geochimica et Cosmochimica Acta, v. 61, n. 7, p. 1359–1412, https://doi.org/10.1016/S0016-7037(97)00009-4

Szponar, N., Brazelton, W. J., Schrenk, M. O., Bower, D. M., Steele, A., and Morrill, P. L., 2013, Geochemistry of a continental site of serpentinization, the Tablelands Ophiolite, Gros Morne National Park: A Mars analogue: Icarus, v. 224, n. 2, p. 286–296, https://doi.org/10.1016/j.icarus.2012.07.004

Taran, Y. A., Fischer, T. P., Cienfuegos, E., and Morales, P., 2002, Geochemistry of hydrothermal fluids from an intraplate ocean island: Everman volcano, Socorro Island, Mexico: Chemical Geology, v. 188, n. 1–2, p. 51–63, https://doi.org/10.1016/S0009-2541(02)00061-X

Taran, Y. A., Varley, N. R., Inguaggiato, S., and Cienfuegos, E., 2010, Geochemistry of H_2- and CH_4-enriched hydrothermal fluids of Socorro Island, Revillagigedo Archipelago, Mexico. Evidence for serpentinization and abiogenic methane: Geofluids, v. 10, n. 4, p. 542–555, https://doi.org/10.1111/j.1468-8123.2010.00314.x

Taylor, R. M., Hansen, H. C. B., Stanger, G., and Koch, C. B., 1991, On the genesis and composition of natural pyroaurite: Clay Minerals, v. 26, n. 3, p. 297–309, https://doi.org/10.1180/claymin.1991.026.3.01

Thom, J. G. M., Dipple, G. M., Power, I. M., and Harrison, A. L., 2013, Chrysotile dissolution rates: Implications for carbon sequestration: Applied Geochemistry, v. 35, p. 244–254, https://doi.org/10.1016/j.apgeochem.2013.04.016

Tiago, I., and Veríssimo, A., 2013, Microbial and functional diversity of a subterrestrial high pH groundwater associated to serpentinization: Environmental Microbiology, v. 15, n. 6, p. 1687–1706, https://doi.org/10.1111/1462-2920.12034

Tiago, I., Chung, A. P., and Veríssimo, A., 2004, Bacterial diversity in a nonsaline alkaline environment: Heterotrophic aerobic populations: Applied and Environmental Microbiology, v. 70, n. 12, p. 7378–7387, https://doi.org/10.1128/AEM.70.12.7378-7387.2004

Tutolo, B. M., and Tosca, N. J., 2018, Experimental examination of the Mg-silicate-carbonate system at ambient temperature: Implications for alkaline chemical sedimentation and lacustrine carbonate formation: Geochimica et Cosmochimica Acta, v. 225, p. 80–101, https://doi.org/10.1016/j.gca.2018.01.019

Tutolo, B. M., Luhmann, A. J., Tosca, N. J., and Seyfried, W. E., 2018, Serpentinization as a reactive transport process: The brucite silicification reaction: Earth and Planetary Science Letters, v. 484, p. 385–395, https://doi.org/10.1016/j.epsl.2017.12.029

Tutolo, B. M., Evans, B. W., and Kuehner, S. M., 2019, Serpentine–hisingerite solid solution in altered ferroan peridotite and olivine gabbro: Minerals, v. 9, 47, https://doi.org/10.3390/min9010047

Twing, K. I., Brazelton, W. J., Kubo, M. D. Y., Hyer, A. J., Cardace, D., Hoehler, T. M., McCollom, T. M., and Schrenk, M. O., 2017, Serpentinization-influenced groundwater harbors extremely low diversity microbial communities adapted to high pH: Frontiers in Microbiology, v. 8, article n. 308, https://doi.org/10.3389/fmicb.2017.00308

Vacquand, C., Deville, E., Beaumont, V., Guyot, F., Sissmann, O., Pillot, D., Arcilla, C., and Prinzhofer, A., 2018, Reduced gas seepages in ophiolitic complexes: Evidences for multiple origins of the H_2-CH_4-N_2 gas mixtures: Geochimica et Cosmochimica Acta, v. 223, p. 437–461, https://doi.org/10.1016/j.gca.2017.12.018

Vance, S., Harnmeijer, J., Kimura, J., Hussmann, H., deMartin, B., and Brown, J. M., 2007, Hydrothermal systems in small ocean planets: Astrobiology, v. 7, n. 6, p. 987–1005, https://doi.org/10.1089/ast.2007.0075

Wagman, D. D., Evans, W. H., Parker, V. B., Schumm, R. H., Halow, I., Bailey, S. M., Churney, K. L., and Nuttall, R. L., 1982, The NBS tables of chemical thermodynamic properties: selected values for inorganic and C1 and C2 organic substances in SI units: New York, York, American Chemical Society, Journal of Physical and Chemical Reference Data Supplement, 392 p.

Warren, J. M., 2016, Global variations in abyssal peridotite compositions: Lithos, v. 248–251, p. 193–219, https://doi.org/10.1016/j.lithos.2015.12.023

Weast, R. C., and Lide, D. R., editors, 1989, CRC handbook of chemistry and physics: a ready-reference book of chemical and physical data: Boca Raton, Florida, CRC Press, 2528 p.

Wetzel, L. R., and Shock, E. L., 2000, Distinguishing ultramafic-from basalt-hosted submarine hydrothermal systems by comparing calculated vent fluid compositions: Journal of Geophysical Research: Solid Earth, v. 105, n. B4, p. 8319–8340, https://doi.org/10.1029/1999JB900382

Wheat, C. G., Fryer, P., Fisher, A. T., Hulme, S., Jannasch, H., Mottl, M. J., and Becker, K., 2008, Borehole observations of fluid flow from South Chamorro Seamount, an active serpentinite mud volcano in the Mariana forearc: Earth and Planetary Science Letters, v. 267, n. 3–4, p. 401–409, https://doi.org/10.1016/j.epsl.2007.11.057

Whitney, D. L., and Evans, B. W., 2010, Abbreviations for names of rock-forming minerals: American Mineralogist, v. 95, n. 1, p. 185–187, https://doi.org/10.2138/am.2010.3371

Wolery, T., and Jarek, R., 2003, EQ3/6, version 8.0, software user's manual: US Department of Energy, Office of Civilian Radioactive Waste Management, Office of Repository Development 10813-UM-8.0-00, 376 p.

Wolery, T. J., and Jove-Colon, C. F., 2004, Qualification of thermodynamic data for geochemical modeling of mineral-water interactions in dilute systems: US Department of Energy, Office of Civilian Radioactive Waste Management, Office of Repository Development ANL-WIS-GS-000003, 212 p.

Woycheese, K. M., Meyer-Dombard, D. R., Cardace, D., Argayosa, A. M., and Arcilla, C. A., 2015, Out of the dark: Transitional subsurface-to-surface microbial diversity in a terrestrial serpentinizing seep (Manleluag, Pangasinan, the Philippines): Frontiers in Microbiology, v. 6, article n. 44, https://doi.org/10.3389/fmicb.2015.00044

Zarubin, D., and Nemkina, N., 1990, The solubility of amorphous silica in alkaline aqueous solutions at constant ionic strength: Zhurnal Neorganicheskoi Khimii, v. 35, p. 31–38.

Zgonnik, V., Beaumont, V., Larin, N., Pillot, D., and Deville, E., 2019, Diffused flow of molecular hydrogen through the Western Hajar mountains, Northern Oman: Arabian Journal of Geosciences, v. 12, article n. 71, https://doi.org/10.1007/s12517-019-4242-2